The Pennsylvania State University

The Graduate School

College of Engineering

EFFECTS OF EXTERNAL STIMULI ON MICROSTRUCTURE-PROPERTY RELATIONSHIP AT THE NANOSCALE

A Dissertation in

Mechanical Engineering

by

Baoming Wang

© 2017 Baoming Wang

Submitted in Partial Fulfillment
of the Requirements
for the Degree of

Doctor of Philosophy

August 2017

The dissertation of Baoming Wang was reviewed and approved* by the following:

Aman Haque
Professor of Mechanical Engineering
Dissertation Advisor
Chair of Committee

Donghai Wang
Associate Professor of Mechanical Engineering

Reuben Kraft
Assistant Professor of Mechanical Engineering

Douglas E. Wolfe
Professor of Materials Science and Engineering

Karen A. Thole
Professor of Mechanical Engineering
Head of the Department of Mechanical and Nuclear Engineering

*Signatures are on file in the Graduate School

ABSTRACT

Due to their small physical and microstructural size, nanoscale materials show significantly different behavior compared to the bulk. Size effects studies on materials behavior, particularly at the nanoscale, has been a vigorously active area of research. The state of art is to characterize materials properties at individual domains, such as mechanical, electrical and thermal. Fundamental aspects of microstructure-properties relationship in these individual domains are relatively well understood. Nevertheless, experiments relating external stimuli, such as stress, temperature, electrical current, light, ion irradiation to structure and properties at the nanoscale remain challenging at this length-scale. From a fundamental perspective, small size should make materials more sensitive to stimuli compared to bulk. If this hypothesis is validated, one can envision facile tuning of microstructure to actively control materials properties. Such tunability would enhance performance in broader areas of electronics, energy conversion and sensors. This motivates us to experimentally investigate the stimuli-microstructure-property relationship at the nanoscale.

The technical contribution of this research is a unique nanofabricated experimental setup that integrates nanoscale specimens with tools for interrogating mechanical (stress-strain, fracture, and fatigue), thermal and electrical (conductivity) properties as function of external stimuli such as strain, temperature, electrical field and radiation. It addresses the shortcomings of the state of the art characterization techniques, which are yet to perform such simultaneous and multi-domain measurements. Our technique has virtually no restriction on specimen material type and thickness, which makes the setup versatile. It is demonstrated with 100 nm thick nickel, aluminum, zirconium; 25 nm thick molybdenum di-sulphide (MoS_2), 10 nm hexagonal boron nitride (h-BN) specimens and 100nm carbon nanofiber, all in freestanding thin film form. The technique is compatible with transmission electron microscopy (TEM). In-situ TEM captures microstructural features, (defects,

phases, precipitates and interfaces), diffraction patterns and chemical microanalysis in real time. ‘Seeing the microstructure while measuring properties’ is our unique capability. It helps identifying fundamental mechanisms behind thermo-electro-mechanical coupling and degradation, so that these mechanisms can be used to (i) explain the results obtained for mesoscale specimens of the same materials and experimental conditions and (ii) develop computational models to explain and predict properties at both nano and meso scales. The uniqueness of this contribution is therefore simultaneously quantitative and qualitative probing of length-scale dependent external stimuli effects on microstructures and physical properties of nanoscale materials.

The scientific contribution of this research is the experimental validation of the fundamental hypothesis that, if the nanoscale size can cause significant deviation in a certain domain, e.g., mechanical, it can also make that domain more sensitive to external stimuli when compared to bulk. We have showed that mechanical properties of freestanding nanocrystalline thin films have higher sensitivity to elevated temperatures compared to bulk. The Young’s modulus of nanocrystalline aluminum thin film is measured about 50% of the room temperature value at 65% of the melting temperature. The higher volume fraction of grain boundaries can be ascribed to this observation since the inherent disorder on the grain boundary atoms means they are more sensitive to the temperature. At the bulk scale, thermal conductivity of metals is not sensitive to mechanical strain. However, this may not be true for grain sizes below the electron mean free paths, for which mechanical deformation mechanism and volume fraction of grain boundaries are drastically different from the bulk. Our experimental results show strong mechanical strain-thermal conductivity coupling, thermal conductivity of Zr film with average grain size of 10nm dropped from 20 W/m-K to 13 W/m-K with a strain level of only 1.24 %.

In this dissertation, we present a series of studies tied by the common thread of synergy of two or more stimuli. The first example is on pure metals, which need very high temperature (>

$0.5T_m$, where T_m is melting point) or stress ($>\sigma_y$, where σ_y is the yield stress) to change microstructure. In contrast, we present experimental evidence of about 100 times grain growth in nanocrystalline nickel at only $0.2T_m$ (T_m is the melting temperature) when accompanied with only 0.2 σ_y (σ_y is the yield stress) stress. This finding contradicts with the classical understanding that grain growth is a plastic deformation ($>\sigma_y$) mechanism. Interestingly, stressing the films by high stress (around σ_y) or temperature ($0.5T_m$) separately produce only insignificant grain growth. These results suggest that when synergistic, external stimuli can exert unprecedented influence over microstructure-properties in nanoscale materials. In a corollary study, we modeled nanocrystalline metals as a standard linear elastic solid and our experimental results on 100 nm thick (average grain size 10 nm) freestanding nickel specimens at temperatures from 300 to 425 °K support this hypothesis reasonably well. The viscosity of solid nickel ranged from $3.3\text{x}10^{13}$ Pa.s to $1.5\text{x}10^{13}$ Pa.s at these temperatures, which are about two orders of magnitude smaller than that expected for metals and are also less sensitive to temperature compared to bulk.

The second case study involved a novel concept of electro-graphitization that induces synergistic thermo-electro-mechanical fields to graphitize carbon nanofibers at around 800 ºC temperature and below 10^6 A/cm^2 current density. In comparison, conventional graphitization of carbon nanofiber requires very high temperatures (> 2800 °C). A more convincing study on the pronounced role of stimuli on microstructure-properties is the transformation of amorphous materials to nano or microcrystalline form. This is because typically the energy barrier for this kind of transformation is very high, requiring extreme conditions to initiate such transformation. To pursue this, we studied 25 nm thick MoS_2 and 10 nm h-BN films. Our in-situ TEM heating of these specimens indicated that such phase transformation can be induced to temperatures as low as 600 °C.

In the third study, we observed anomalous response of GaN microstructure to the externally applied electrical field at nanoscale. 90° domain switching in 100nm thick GaN film was observed at a 10^7 V/m electrical field, applied perpendicular to the polarization direction. No such switching was observed for thicker films. This anomalous behavior is explained by the nanoscale size effects on the piezoelectric coefficients of GaN, which can be 2-3 times larger than the bulk value.

We also explored the sensitivity of nanoscale materials to photons and ions. With light radiation on monolayer MoS_2 films, we observed very strong light-matter interaction (photo voltaic effects) without any apparent rectifying junctions. For bi-layers, no such effect was present, suggesting strong size effect in light-matter interaction. The photo-voltaic effect was observed to highly direction dependent in the film plane, which suggests that the oblique deposition configuration plays a key role in developing the rectifying potential gradient. We have studied ion irradiation effects in Zr thin films, showing significant grain growth (>300%), texture evolution, and displacement damage defects. Stress-strain profiles were mostly linear elastic below 20 nm grain size, but above this limit the samples demonstrated yielding and strain hardening. Experimental results support the hypothesis that grain boundaries in nanocrystalline metals act as very effective defect sinks.

Since microstructures-properties in nanoscale are sensitive to external stimuli, structural stability or degradation of nanoscale materials due to over stimuli will be an important topic to study. To pursue this, we studied the degradation mechanism of graphene and WSe_2/graphene heterostructure as a function of temperature and electrical current density. Our experimental results show that high temperature and current density can induce migration of foreign contaminants due to phenomena similar to thermo and electromigration and alloying with foreign elements leads to catastrophic degradation in crystallinity.

This dissertation presents experimental evidence of external stimuli effects on the microstructures-properties relationship at nanoscale. The technological aspect of this research impacts nanotechnology applications, like microelectronics, optoelectronics, energy conversion and sensors. However, it is also very fundamental in nature, and the new phenomena that are explored will enrich knowledge of material behavior and lay foundation for the future work on multi-physics of material at nanoscale.

TABLE OF CONTENTS

List of Figures x

List of Tables xvi

Acknowledgements xvii

Chapter 1 Introduction 1

- 1.1. Length-scale Effects on Materials Behavior 1
- 1.2. External Stimuli Effects at Bulk and Smaller Length Scales 4
- 1.3. Objectives and Impacts of this Research 5

Chapter 2 Mechanical (Stress/ Strain) Effects 9

- 2.1 Mechanical Behavior of Nanocrystalline Zirconium Thin Films 10
  - 2.1.1 Objective and Motivation 10
  - 2.1.2 Materials and Methods 11
  - 2.1.3 Experimental Results and Discussion 13
  - 2.1.4 Conclusion 17
- 2.2 Low Temperature Viscoelasticity in Nanocrystalline Nickel Films 17
  - 2.2.1 Introduction 17
  - 2.2.2 Experimental Details 18
  - 2.2.3 Results and Discussion 20
  - 2.2.4 Conclusion 23
- 2.3 Thermo-Mechanical Coupling in Zirconium Thin Films 24
  - 2.3.1 Literature Review and Objective 25
  - 2.3.2 Experimental Setup 27
  - 2.3.3 Experimental Results and Analysis 34
  - 2.3.4 Conclusion 36

Chapter 3 Thermal Effects 38

- 3.1 Mechanical Behavior of Aluminum Thin Film at Elevated Temperature 39
  - 3.1.1 Experimental Design and Setup 39
  - 3.1.2 Experimental Results and Discussion 42
  - 3.1.3 Conclusion 44
- 3.2 Domain Engineering of Physical Vapor Deposited Two-Dimensional Materials 45
  - 3.2.1 Introduction 45
  - 3.2.2 Sample Preparation and Experimental Setup 49
  - 3.2.3 Results and Discussion 51
  - 3.2.4 Conclusion 54

Chapter 4 Synergistic Effects of Stress and Temperature 55

- 4.1 Introduction 56
- 4.2 Experimental Setup 57

4.3 Results and Discussion....59
4.4 Conclusion....62

Chapter 5 Electrical (Current Density or Field) Effects....64

5.1 Electro-graphitization and Exfoliation of Graphene on Carbon Nanofibers....65
5.1.1 Literature Review....65
5.1.2 Experimental Setup....68
5.1.3 Experimental Results and Discussion....70
5.1.4 Conclusion....81
5.2 Domain Switching in GaN Thin Films....82
5.2.1 Introduction....82
5.2.2 Materials and Methods....85
5.2.3 Results and Discussion....87
5.2.4 Conclusion....91

Chapter 6 Degradation....92

6.1 High Temperature and Current Density Induced Degradation of Multi-layer Graphene....93
6.1.1 Background and Motivation....93
6.1.2 Experimental Setup....94
6.1.3 Results and Discussion....97
6.1.4 Conclusion....101
6.2 In-situ Degradation Studies of Two-dimensional WSe_2-Graphene Heterostructures....102
6.2.1 Introduction....102
6.2.2 Experimental Setup....105
6.2.3 Results and Discussion....107
6.2.4 Conclusion....113

Chapter 7 Sensitivity to Photons and Ions....115

7.1 Photo-Sensitivity of Large Area Physical Vapor Deposited Mono and Bilayer MoS_2....116
7.1.1 Introduction....116
7.1.2 Materials and Methods....117
7.1.3 Results and Discussion....119
7.1.4 Conclusion....124
7.2 Self-Ion Irradiation Effects on Mechanical Properties of Nanocrystalline Zr Films....124
7.2.1 Introduction....125
7.2.2 Experimental Setup....126
7.2.3 Results and Discussion....128
7.2.4 Conclusion....134

References....135

LIST OF FIGURES

Figure 1.1. Break down of scaling mechanics in the mechanical domain at grain sizes below 25 nm. 2

Figure 1.2. Variation of electrical resistivity with width of nanowire in (a) Gold [4] and (b) Copper [5]. 3

Figure 1.3. Variation of thermal conductivity of Silicon with temperature in (a) thin films [10] and (b) nanowires [11]....... 3

Figure 1.4. (a) MEMS device on fingertip (b) MEMS device accommodated in TEM holder for in-situ TEM testing (c) SEM image of the MEMS device. 6

Figure 2.1. Experimental setup, (a, b, c) front, side and rear ends of the in-situ electrical biasing TEM specimen holder respectively (d) zoomed view of the MEMS thin film tensile testing chip showing specimen, actuators and sensors (e, f) schematic representation and force equilibrium diagram of the test chip respectively [50] (g) infrared image of the test chip after actuation....... 12

Figure 2.2. (a) Bright-field TEM image of the as-deposited specimen and (b) selected area electron diffraction pattern....... 13

Figure 2.3. (a) Representative stress-strain diagram for nanocrystaline zirconium specimens measured in situ inside a TEM (b) nanoscale voids appears at the grain boundaries at the onset of fracture. 14

Figure 2.4. Grain growth as function of polarity and magnitude of dc electrical current passed through the freestanding specimen. 15

Figure 2.5. (a) Bright-field TEM image of specimen after 5 mins of current flow at $0.5x10^6 A/cm^2$ density (b) TEM selected area electron diffraction (c) Stress-strain curve....... 16

Figure 2.6. (a) Scanning electron micrograph of the MEMS device integrating a freestanding thin film specimen with microheaters, force sensors and electro-thermal actuators (not shown), (b, c, d) schematic rendering of the force sensor and specimen before, during and after a step loading....... 19

Figure 2.7. Time vs. displacement plot of the point marked B on the specimen at (a) 275 K and (b) 425 K temperatures....... 21

Figure 2.8. Quasi-static uniaxial tensile stress-strain diagram for the freestanding nickel specimens....... 21

Figure 2.9. (a) Variation of the unrelaxed modulus and the viscous damping coefficient with temperature, (b) calculation of the activation energy for the viscous damping element....... 23

Figure 2.10. Experimental setup, (a) SEM image of the MEMS thin film tensile testing chip showing specimen, actuators and sensors (b, c) schematic diagram showing displacement based force and strain measurement (d) SEM image of the heaters and the freestanding specimen. schematic representation and force equilibrium diagram of the test chip respectively. 28

Figure 2.11. Fabrication details of MEMS thermo-mechanical testing device........................30

Figure 2.12. (a) Bright-field TEM image of the as-deposited specimen, the inset shows selected area electron diffraction pattern and (b) Stress-strain diagram of as deposited specimen..31

Figure 2.13. (a) Infrared thermal image of the device when one-side heater is activated; (b) Mathematical model of proposed study; (c) Estimation of heat transfer coefficient h_c by curve fitting with model; (d) Representative matching of experimental data with model prediction. 33

Figure 2.14. Experimental results for as-deposited specimens with 10 nm grain size (a) Comparison of experimental temperature profile with model prediction at various strains; (b) Plot of measured thermal conductivity as a function of externally applied mechanical strain...35

Figure 2.15. TEM bright field image of (a) as-deposited specimen and (b) specimen after grain growth with an average grain size of 250 nm; (c) Plot of thermal conductivity as function of grain size..36

Figure 3.1. (a) Finite element simulation of the MEMS device, (b) the experimental setup showing an electrical biasing holder and the MEMS chip (c) micro-heaters at specimen ends to generate temperature gradient if desired (d) micro-heaters at specimen sides to generate uniform temperature field, (e) schematic view of specimen elongation and force measurement..41

Figure 3.2. Temperature calibration with infrared microscopy of the (a) end heated and (b) side heated samples, (c) comparison with finite element simulation (d, e) demonstration of aluminum melting (around 925 K)..42

Figure 3.3. (a) Uniaxial tensile stress-strain response of 100 nm thick freestanding aluminum at room temperature, (b) TEM image of the specimen at room temperature and (c) stress-strain response at homologous temperature of 0.65, (d) TEM image of the high temperature specimen at 85 MPa stress and 0.18% strain, (e) TEM image of the high temperature specimen at 3.5 MPa stress and 4.4% strain. 44

Figure 3.4. Experimental details (a) PVD of specimen layers on oxide coated silicon wafer and a protective titanium over-layer (b) reactive ion etching of all the layers and additional isotropic etching of silicon after photolithographic patterning preparation (c) nano-manipulation of the a cleaved specimen on to a MEMS device and (d) securing it with carbon deposition (e) vapor phase hydro-fluoric acid etch to remove the protective titanium and oxide layers, (f) infrared image of the MEMS heaters and

(g) experimental validation of a finite element model for heater temperature estimation in TEM. 50

Figure 3.5. Experimental results on MoS_2 (a) bright field TEM, (b) electron diffraction and (c) Raman spectroscopy of the as-deposited specimen while supported on the substrate measured with 10 mW excitation laser power. After in-situ TEM annealing at 600 °C, (d) bright field TEM and (e) electron diffraction shows significant grain/domain growth, (f) comparison of the as-deposited and annealed Raman spectra with that for a single crystal MoS_2. The power was reduced to 1 mW to avoid damage to the free-standing specimens, thus the intensity of the as-deposited film is significantly reduced. 52

Figure 3.6. Experimental results for amorphous boron nitride (a) bright field TEM, (b) electron diffraction of the as-deposited specimen. After in-situ TEM annealing at 600 °C, (d) bright field TEM and (e) electron diffraction shows significant grain/domain growth with hexagonal crystal structure. 53

Figure 4.1. (a) Scanning electron micrograph showing various components of a MEMS device for quantitative in-situ TEM testing of thin films (false colored), (b, c) Bright-field and selected area electron diffraction pattern of the as-deposited nano-crystalline Ni specimen (d, e) room temperature grain growth in a span of 30 to 60 days. Scale bar represents 500 nm. 58

Figure 4.2. TEM images of the specimens at (a) room temperature (b) 0.2 T_m with no applied stress, (c) no applied stress and (b) 1.7 GPa stress at room temperature. Scale bar is 500 nm. 60

Figure 4.3. TEM and selected area diffraction images of a specimen loaded at (a) $0.2T_m$, $0.2\sigma_Y$ and (b) $0.2T_m$, $0.5\sigma_Y$. 61

Figure 5.1. Proposed electrical current induced graphitization and subsequent surface exfoliation to create high conductivity graphitic nanofibers with high surface area graphene. 68

Figure 5.2. Experimental setup (a) nanofabricated chip with microelectrodes mounted on TEM specimen holder, SEM image of (b) single carbon nanofiber and (c) nanofiber-junction-nanofiber specimen, suspended on a micro fabricated through-the-wafer hole (d) zoomed TEM image of the carbon nanofiber. 69

Figure 5.3. (a) Electrical resistance of single carbon nanofiber as function of electrical current. Bright field TEM images are labeled with values of applied current density. (b) Raman spectra of as-received and electro-graphitized carbon nanofiber specimen. 71

Figure 5.4. (a) Melting of silver on carbon nanofiber, which subsequently (b) coalesce and (c) evaporate inside the TEM chamber. (d-f) failure of the semiconducting nanofiber. 73

Figure 5.5. TEM images of the (a) as-received specimen and (b) after electro-graphitization and subsequent graphene exfoliation (c) zoomed view of location B and (d) location A showing exfoliated graphene on the carbon nanofiber surfaces..................................75

Figure 5.6. Electron energy loss spectra (EELS) obtained from (a) nanofiber shell and (b) exfoliated flakes at the surface...76

Figure 5.7. (a) Proposed electro-static charge based exfoliation mechanism for surface layers (b-d) TEM image showing evolution of the exfoliated structure, (e) gray scale mapping of the distance between two layers is 0.34 nm, indicating graphene and not nanotube formation (f) high magnification images of the graphene flakes. 78

Figure 5.8. (a, b) Very small contact area and (c, d) poorly conducting amorphous skin result in large contact resistance in a carbon nanofiber network (e) electrical resistance of a fiber-contact-fiber configuration as function of electro-graphitization, (f) evolution of graphene flakes resulting in diminishing contact resistance, (g) high magnification TEM image of the graphene-graphene contact between two nanofibers. 79

Figure 5.9. (a-c) TEM sample preparation process using FIB. A 100 nm thin coupon is milled and then rotated before (d) mounting on two electrodes on (e) micro device that fits a (f) TEM specimen holder with electrical biasing capability. (g) Raman spectra of the GaN specimen showing excellent crystallinity...87

Figure 5.10. (a-c) Bright field TEM image at various levels of electrical biasing. (d) Selected area diffraction pattern before biasing and (e) at 20 V. Low magnification images of the specimen (f) and (g) after domain switching and catastrophic failure. The poling and electrical field directions are highlighted using arrows. 88

Figure 5.11. (a) Domain switching in 100 nm thick film occurs at 20 V (b) about 55 V is needed to store the same internal energy in a 2 micron thick film, which is long preceded by electrical breakdown, a reason domain switching in GaN is typically not observed at the bulk scale. 91

Figure 6.1. (a) Optical image of a micro-electro-mechanical device with specimens schematically located at X and Y positions, (b) schematic diagram of the freestanding specimen (c, d) scanning electron image of the specimens at X and Y locations. 96

Figure 6.2. (a) TEM electron diffraction and (b) Raman spectra of the freestanding multi-layer graphene specimen before the passage of heat and/or current. 97

Figure 6.3. (a-c) Migration of silicon atoms on multi-layer graphene in form of waves at about 930 °C. The arrows indicate the silicon atom wave fronts. (d) microstructural change related to silicon carbide formation (e) continued migration of silicon atoms (f) SEM image of a specimen showing no melting of the silicon clamping ends (g) energy dispersive spectroscopy showing silicon over the freestanding region................99

Figure 6.4. (a) TEM image of the nanocrystalline silicon carbide and corresponding diffraction pattern after indexing (b) Raman spectra of specimen corresponding to

Figure 6.3f confirming decomposition of the carbon atoms followed by excessive migration of silicon. 100

Figure 6.5. (a) Heating multi-layer graphene specimen in absence of electrical current induces thermal motion of polymeric residue, which (b) pyrolizes at elevated temperatures. No migration of silicon is seen. 101

Figure 6.6. (a) Experimental setup consisting of a micro-electro-mechanical devices mounted on an electrical biasing TEM holder (b) Zoomed view of the device showing heater and actuator areas (c) Zoomed view of a heater (d) Zoomed view of a freestanding WSe_2-graphene heterostructure on the heater area (e) Zoomed view of a freestanding specimen in the actuator area (f) Triangle shaped domains of highly crystalline WSe_2 on graphene. 106

Figure 6.7. In-situ TEM observation of the microstructure and corresponding electron diffraction patterns at various temperatures. 108

Figure 6.8. Energy dispersive spectroscopy of the thermally degraded WSe_2-graphene heterostructure showing (a) surface diffusion of silicon and (b) carbon (c) Raman spectra suggesting various alloys of tungsten, silicon and carbon. 110

Figure 6.9. In-situ TEM observation of the microstructure and corresponding electron diffraction patterns at various temperatures and current densities. 111

Figure 6.10. Energy dispersive spectroscopy of the electro-thermally degraded WSe_2-graphene heterostructure showing (a) surface diffusion of silicon and (b) carbon (c) Raman spectra suggesting alloying of silicon carbide and tungsten disilicide. 112

Figure 6.11. TEM diffraction pattern shown in Figures 6.7 and 6.9 indexed against (a) silicon and (b) silicon carbide. 113

Figure 7.1. (a) Schematic of the pulsed dc magnetron sputtering configuration (b) Cross-sectional TEM (dashed lines are added for highlighting the MoS_2 layers, (c) X-ray photoelectron spectroscopy data revealing the structure (d) 1cm x 1cm MoS_2 specimen packaged for van der Pauw measurements showing the large active area. 119

Figure 7.2. I-V characteristics under dark and 1.2 milli-Watts illumination for (a) mono-layer and (b) bi-layer MoS_2 devices. The corresponding values, when measured with electrodes at perpendicular ($\perp$) direction in (c) monolayer and (d) bilayer devices exhibit remarkable anisotropy in photo-sensitivity. Predominant nature of ohmic contact is seen for all the devices. 120

Figure 7.3. (a) Micro-machined electromechanical device for mechanical testing of thin films (b) zoomed-in view of the specimen gauge section before ion irradiation (c) the same location after ion irradiation and subsequent substrate etching (d) schematic showing displacement and force measurement. 127

Figure 7.4. SRIM simulation of (a) collision events and (b) ion ranges in 100 nm thick zirconium thin films on silicon substrate irradiated with 800 keV Zr^+ ions. The plots are super-imposed on an SEM image of the specimen before the silicon layer is etched away. 129

Figure 7.5. (a-e) TEM images of the specimens after various levels of irradiation damage, (f) increase in measured grain size from the 10 nm as-deposited value as function of irradiation damage. 130

Figure 7.6. Select area electron diffraction patterns of the specimens at various irradiation dosage 131

Figure 7.7. Effect of self-ion irradiation driven microstructural changes on the mechanical properties of nanocrystalline zirconium thin films. 132

Figure 7.8. Effect of self-ion-irradiation on (a) Young’s modulus (inset shows the grain size as function of damage that correlates grain size with Young’s modulus) and (b) strain hardening of nanocrystalline (as-deposited grain size ~10 nm) zirconium thin films. 133

LIST OF TABLES

Table 7.1. Dark dc resistivity of the mono and bi-layer MoS_2 specimens. 119

ACKNOWLEDGEMENTS

I thank my graduate advisor, Dr. Aman Haque for the opportunity to work with him and learn nanofabrication, microscopy and most importantly how to formulate and solve fundamental problems using these tools. He always has been patient, resourceful, encouraging and instructive with positive criticism on my shortcomings. I also thank the members of the doctoral committee for consent to be a part of it and being ready to help me. Special thanks to my colleagues Tarek, Raghu, Zahabul and Tun for sharing their invaluable experience with me and providing moral support. I would like to thank staff at the Penn State MRI Guy, Shane, Mike, Kathy, Andy, Bangzhi, Bill, Tim, Max, Josh, Trevor, Ke, Jennifer, Haiying and Intae at the ADL, SUNY Binghamton for helping me with difficulties regarding the nanofabrication process and microscopy techniques. I am also very grateful to my friends for their tremendous support and encouragement throughout this work. My sincerest thanks to my wife-Mengyuan, who always stands by me with her full support. Last but not the least, utmost thanks goes to my parents, grandparents and to my brother and sister for being constant source of encouragement and having belief in me.

Chapter 1

Introduction

1.1. Length-scale Effects on Materials Behavior

It is well established in the literature that materials properties depend on the microstructural dimensions and features (grain size, dislocation density) [1]. A well-studied example is the Hall-Petch effect, where materials strength (σ_y) is related to grain size (d) as,

$$\sigma_y = \sigma_0 + kd^{-\frac{1}{2}} \quad (1)$$

Where σ_0 is the stress needed to move individual dislocations and k is a material dependent constant. Such phenomenological relationships are known to breakdown at or below a length-scale, where the materials physical dimensions are comparable to microstructural sizes [2]. Such breakdown is ascribed to completely different deformation mechanisms at the nanoscale. Extreme dimensional confinements, predominance of interfacial phenomena and unique atomic configuration lead to unusual materials properties. The Hall-Petch relationship, for example, breaks down below 25 nm grain size. This is also the length-scale of interest in this dissertation. Criteria like deformation mechanism, energy distribution in the surface shell, high surface area to volume ratio are some of the underlying physics that explain the unusual behavior. Further motivation for this research comes from the observation that the explosive growth of the micro-electronics industry (and subsequently, nanotechnology) has ushered materials with even smaller length-scales, highlighting the importance of such size effects of performance and reliability of modern devices.

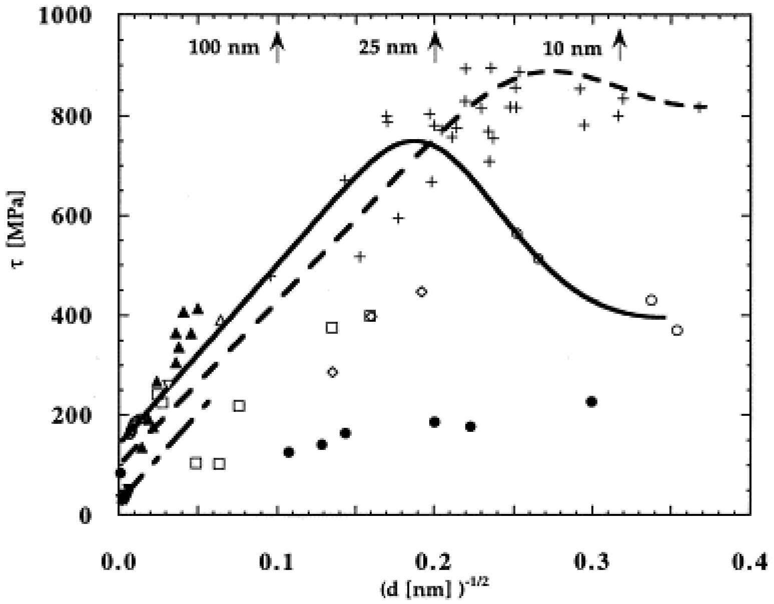

Figure 1.1. Break down of scaling mechanics in the mechanical domain at grain sizes below 25 nm.

The conceptual foundation of this dissertation is based on the observation that breakdown of classical mechanics and physics also influences other (electrical, thermal, magnetic etc.) domains. Electrical properties of thin films and materials at small scale are observed to deviate from the bulk value, albeit at a different scaling of length (when electron mean free path is comparable to grain size or film thickness/width). Enhanced electron scattering at grain-boundary and surface are known to increase the electrical resistivity, is modeled by Mayadas and Shatzkes [3]. Size-dependent resistivity was observed and was found to increase with decreasing diameter of gold [4] and copper [5, 6] nanowires. As one goes towards smaller wire dimensions, the mean grain size reduces that increases the number of grain boundaries resulting in higher electrical resistivity. Figure 1.2 shows the variation of the electrical resistivity with width for gold and copper nanowires from the works reported in the literature. With the number of interconnects increasing consistently, this is already a major problem in state of the art transistors [7-9] .

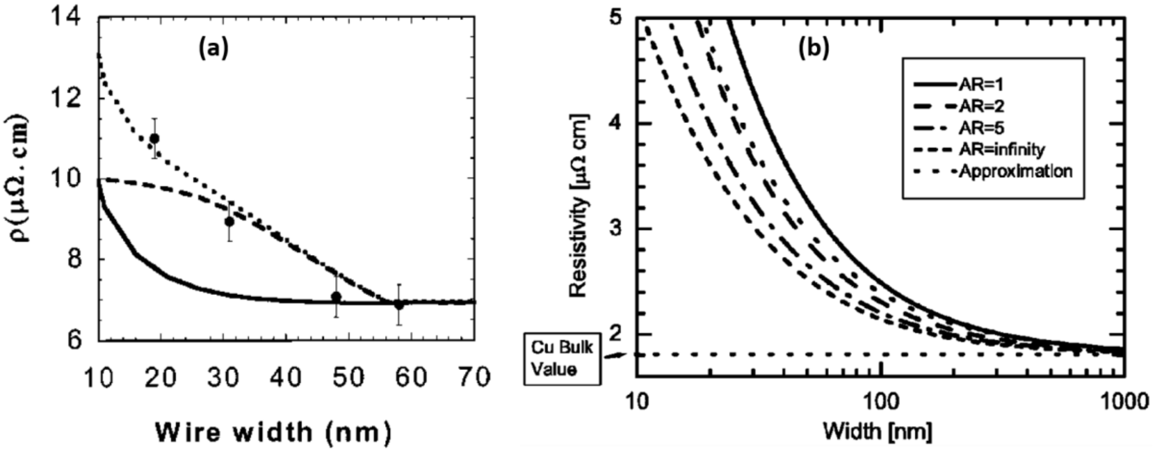

Figure 1.2. Variation of electrical resistivity with width of nanowire in (a) Gold [4] and (b) Copper [5].

While the electron transport in thin films and one-dimensional nanostructures is studied very extensively, thermal (phonon) transport has come under investigation recently. When solids shrink to nanometer range, the thermal transport phenomenon by phonons is altered due to effects like phonon boundary scattering, modifications in the phonon dispersion relation and quantization of phonons. Thermal conductivity at small size scales is mostly observed to be lesser than the bulk value of crystalline solids due to enhanced boundary scattering of phonons.

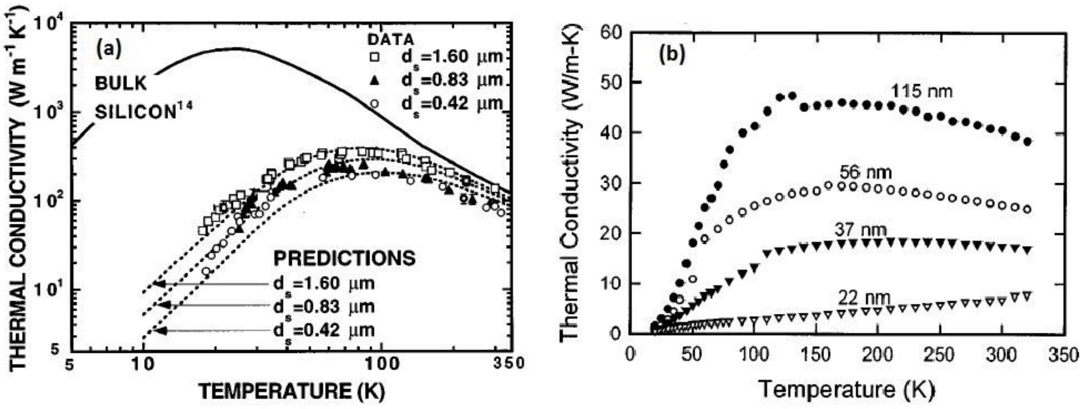

Figure 1.3. Variation of thermal conductivity of Silicon with temperature in (a) thin films [10] and (b) nanowires [11]

Figure 1.3 shows the trend of thermal conductivity of silicon with temperature in silicon thin films [10] and nanowires [11]. It is evident that from the figure that it is much lesser than the bulk value due to enhanced phonon scattering at grain boundaries and imperfections. For nanowires, the variation with temperature is found to be more significant at larger diameters. At smaller diameters, the thermal conductivity behavior deviates from the Debye T^3 law which might be due to changes in the phonon dispersion relation. Computational studies based on Boltzmann transport equation (BTE) and Molecular Dynamics (MD) simulation [12, 13] are also used extensively to predict the thermal transport behavior in nano scale materials.

1.2. External Stimuli Effects at Bulk and Smaller Length Scales

The overarching philosophy of this dissertation is that if extreme length-scale effects can breakdown materials behavior in all physical domains, the same phenomenon can make the materials more susceptible to external stimuli compared to bulk. It is well-known that bulk materials, with exception of semiconductors or very special crystallographic structures, are not very responsive to light, heat, electrical current etc.

For example, the elastic constant of bulk Cu, Ag and Au exhibit very weak temperature dependence up to 800 °K [14]. The young's modulus of micro-sized Ni, single-crystal silicon (SCS) and silicon carbide films (SiC) showed very little or no change from room temperature to 500°C [15, 16]. In the computational investigation, Li et al [17] reported that the thermal conductivity of bulk silicon and diamond changes appreciably at as high as 2% strain. Kuczynski et al [18] measured the strain sensitivity coefficients of electrical resistivity for metals and all were great than unit which indicated non-sensitivity of electrical resistivity to elastic strain. The phase change of Si from amorphous to crystalline through solid phase crystallization (SPC) method happened at around 600 °C [19-21]. Meng et al [22] also reported crystalline to amorphous transformation in Zr-Cu-Al alloys induced by high pressure torsion.

In this dissertation, we hypothesize that the unusual behavior of nanoscale materials in various domains can be interpreted as pronounced effects of the stimuli (such as stress, temperature, and current) respective to these domains. For example, the extreme dimensional constraints on the generation, storage and motion of defects (vacancies, dislocations) as well as the abundance of surface and interfaces breakdown the scaling law of mechanical domain. However, these dimensional constraints also mean enhanced electron and phonon scattering. Law et al [23] reported that characteristic length of various physical phenomenon for solids at room temperature like electron mean free path, phonon free mean path, the Fermi wavelength, the Debye length etc. all fall in the range of 1-50 nm. When the length scales of the sample specimen approach or lie in this range, there is an enhanced coupling between two or more physical domains. Such coupling is expected to manifest in pronounced effects of the external stimuli that are typically absent at the bulk. Existing works in the literature show the effect of mechanical strain, may be substrate induced or externally applied, on properties like thermal conductivity and electrical resistivity [24-27]. It is essential to understand this correlation for a reliable design of nano systems with their applicability increasing consistently.

1.3. Objectives and Impacts of this Research

The objective of this research is to experimentally validate the hypothesis that nanoscale materials are more sensitive to external stimuli compared to bulk. To achieve this, we have developed a versatile test bed that can measure multi-domain properties under controlled exposure to stress, temperature, current etc, as shown in Figure 1.4. This is a micro-electro-mechanical-system based experimental setup with sensors, heaters and actuators integrated with the nanoscale free standing thin film specimens as shown in Figure 1.4c. This device uses the thermal actuation technique where electrical current is passed through highly doped single crystal silicon actuator beams by using electrodes C-C’ in Figure 1.4c. These beams expand slightly in the direction of motion due to Joule heating [28], which applies mechanical load in the specimen. Biasing electrodes A-A’ or B-B’ or both in Figure 1.4c can generate different temperature fields in the specimen and current density can be applied to the specimen by biasing electrodes A-B’ in Figure 1.4c. The setup is compatible with electron, infrared, and Raman microscopes to access the various stimuli and domains, especially transmission electron microscope. Real time microstructures, phase transformation, interfaces, defects with different stimuli can be visualized and recorded while material properties (thermal, electrical, optical, and mechanical) are measured.

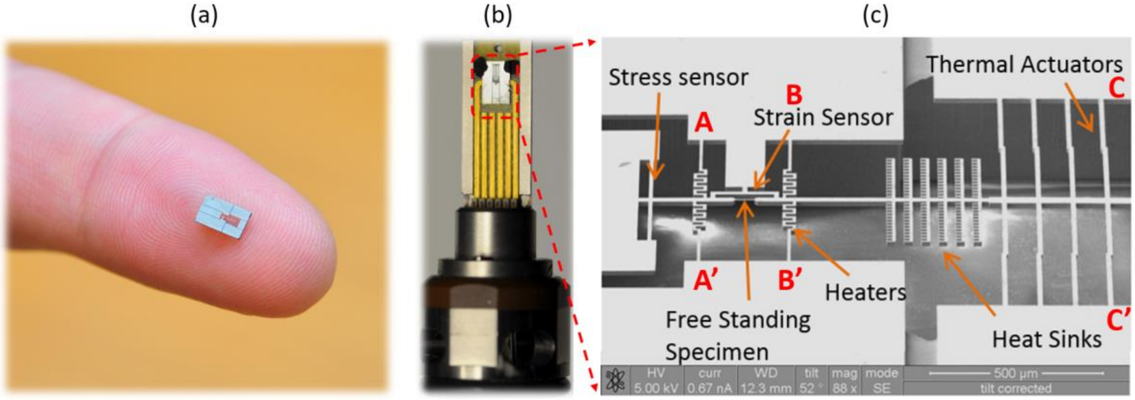
(a)
(b)
(c)
Stress sensor
B
Strain Sensor
Thermal Actuators
C
A
A’
B’
Heaters
Free Standing Specimen
Heat Sinks
C’
HV 5.00 kV
curr 0.67 nA
WD 12.3 mm
tilt 52 °
mag 88 x
mode SE
500 μm
tilt corrected

Figure 1.4. (a) MEMS device on fingertip (b) MEMS device accommodated in TEM holder for in-situ TEM testing (c) SEM image of the MEMS device.

In this dissertation, we have investigated the effects of various external stimuli on the microstructures and properties of different nanoscale materials.

Chapter 2 of this dissertation presents the work on microstructural observation and deformation behavior of nanoscale materials and their properties under mechanical loading. The experimental results in section one suggest the inverse Hall-Petch behavior in nanocrystalline zirconium and great sensitivity of mechanical properties to grain size. In section two, we observed the relaxation behavior of 100nm thick Ni thin films with average grain size of 10nm under mechanical stress. The results show that the viscosity of solid nickel is about two orders of magnitude smaller than that expected for metals and are also less sensitive to temperature compared to bulk. In section three, we studied the thermal conductivity of Zr thin films as a function of mechanical strain and found very strong mechanical strain-thermal conductivity coupling in nanocrystalline Zr thin film.

In chapter 3, temperature or heating is studied as an external stimulus to influence the microstructures and properties of materials. Section one shows greater sensitivity of the mechanical behavior of nanocrystalline aluminum thin films to elevated temperatures compared to its bulk. The experimental results of section two on 25 nm thick MoS_2 and 10 nm h-BN films implies that the phase transformation from amorphous to nanocrystalline or microcrystalline at nanoscale can happen at a much lower temperature than that at bulk scale.

Chapter 4 and Chapter 5 highlights the major contribution of this dissertation: synergy of external mechanical, thermal and electrical field to actively tune the microstructures and thus properties. Chapter 4 shows unusually large grain growth of nickel thin films under low temperature and low stress synergy. Section one of chapter 5 shows remarkable microstructure change and properties improvement of carbon nanofibers with electrical current that induces synergistic thermo-electro-mechanical fields to graphitize carbon nanofibers at much lower temperature than conventional approach. Section two of chapter 5 shows that at nanoscale, electrical filed can cause 90° domain switching in GaN thin film, which is not observed in the bulk scale.

Chapter 6 presents the work on the microstructure stability and degradation of nanoscale materials as a function of external temperature and electrical current. Experimental results show that high temperature can cause dramatic degradation of multilayer graphene or WSe_2/graphene heterostructure specimens. But with the assistance of current, the degradation starts at much lower temperature and the process is greatly accelerated.

Finally, Chapter 7 shows the effect of external radiation. Section one studies the photovoltaic effect of MoS_2 sample and we observed very strong light-matter interaction without any apparent rectifying junctions in monolayer MoS_2 while no such effect was present in the bilayer sample, suggesting strong size effect in light-matter interaction. In next section, the mechanical behavior of nanocrystalline Zr thin films is explored as a function of ion irradiation doses. We observed increased grain size, grain boundary mobility and defects density in the microstructures. Our measurements shows that the Young’s modulus is very sensitive to irradiation below about 15 nm grain size and that strength and ductility are influenced by irradiation in a different manner than the bulk.

The impact of this research can be profound for the design and development of next generation electronics, energy conversion and sensors where ever continuing miniaturization has pushed the materials dimensions even to single digit nanometer scale. We cannot extrapolate bulk behavior at this extreme length-scale and also, classical physics do not predict the hypothesized stimuli effects. However, multi-domain coupling and stimuli effects can be vital for performance and reliability of these devices. For example, strained silicon is used to enhance the electron mobility in MOSFETs [29-31]. Strain/stress effects on optical properties can be also be used for reducing the threshold carrier density and thus increasing the gain of laser diodes [25, 32, 33]. Recently, there are also great interests in using strains to tune the quality factor of nanowire resonators [34]. Strain/stress effects can also be used to enhance the performance of thermoelectric materials [35, 36], which is indeed a combination of strain/stress effects on electrical and thermal transport properties. There are also undesired effects of such stimuli-sensitivity in modern transistors, where miniaturization results in very high power dissipation densities [37] with complex interplay of temperature, stress and current.

Chapter 2

Mechanical (Stress/ Strain) Effects

Contents of this chapter are based on the following journal articles:

- **Baoming Wang**, Vikas Tomar, Aman Haque, "In-situ TEM mechanical testing of nanocrystalline zirconium thin films", *Materials Letters*, Volume 152, Pages 105-108, 2015

  Author of this dissertation designed the experiment, performed the thin film and device preparation, experimentation, data analysis and manuscript writing. Aman Haque took part in experiment design, data analysis and manuscript writing. Vikas Tomar helped in the manuscript preparation.

- **Baoming Wang** and Aman Haque, "Low Temperature Viscoelasticity in Nanocrystalline Nickel Films", *Materials Letters*, Vol. 188, pp. 59-61, 2014

  Author of this dissertation designed the experiment, performed the sample and device preparation, experimentation, data analysis and manuscript writing. Aman Haque took part in experiment design, data analysis and manuscript writing.

- **Baoming Wang**, Raghu Pulavarthy, Aman Haque, "Grain size induced thermo-mechanical coupling in Zirconium thin films", *Journal of Thermal Analysis and Calorimetry*, Volume 123, Issue 2, pp 1197–1204, 2016

  Author of this dissertation designed the experiment, performed the sample and device preparation, experimentation, data analysis and manuscript writing. Raghu Pulavarthy assisted in experimentation, data analysis and corresponding manuscript writing. Aman Haque took part in experiment design, data analysis and manuscript writing.

2.1 Mechanical Behavior of Nanocrystalline Zirconium Thin Films

In this section, mechanical behavior of nanocrystalline zirconium thin films was investigated in-situ inside a transmission electron microscope (TEM). The yield stress measured for specimens with <10 nm grain size was around 450-500 MPa compared to the bulk value of 250-300 MPa. Similar grain size effects are seen on fracture stress and strain of about 0.9 GPa and 1.5-2% respectively. Using in-situ TEM, we demonstrate control of grain size in the specimens using the electro-migration stress and temperature. The experimental results suggest that the critical grain size for inverse Hall-Petch type relationship in nanocrystalline hexagonal close packed metals could be around 15 nm.

2.1.1 Objective and Motivation

Zirconium is a strong and ductile metal with hexagonal close packed (HCP) crystal structure at room temperature. Its strength, resistance to corrosion and irradiation, high melting point and biocompatibility are attractive features for important applications in nuclear, aviation and surgical implant industries. Even though nanocrystalline materials exhibit higher yield strength and resistance to fatigue [38, 39], more comprehensive studies in the relevant literature considered ultra-fine (around 100 nm) grain sizes [40, 41]. These studies addressed the challenges in the nanocrystalline materials preparation through severe plastic deformation, surface mechanical attrition treatment or cryo-rolling [42, 43]. Such multi-modal grain distribution results in a unique combination of high strength and large ductility, e.g. a high ultimate tensile strength of ~658 MPa and large uniform elongation of ~8.5% [44]. Micro-scale pillars have also been fabricated using focused ion beam machining [45, 46], which are then tested under compression to study role of grain size and pillar diameter.

In this study we take a different approach, where sputtered thin films are patterned and integrated with micro-electro-mechanical system (MEMS) sensors and actuators, thereby limiting the test chip size to 3mm x 5mm. The electron transparent specimens are released from the silicon substrate, which allows us to perform mechanical tests inside a transmission electron microscope (TEM). In-situ TEM tests can reveal microstructural features, (defects, phases, precipitates and interfaces), diffraction patterns and chemical microanalysis in real time [47]. Integration of MEMS sensors allow mechanical stress and strain to be measured [48, 49]. The unique simultaneously quantitative mechanical properties and qualitative defect and microstructural visualization will lead to accurate and quick (direct observation based) modeling of nanocrystalline zirconium deformation.

2.1.2 Materials and Methods

Figure 2.1 shows our experimental setup, where the chip is mounted on a TEM specimen holder (Figure 2.1a). The holder itself is shown in Figure 2.1b, with electrical biasing (Figure 2.1c) for electro-thermal actuation of the test chip inside the TEM. A SEM image of the test chip is shown in Figure 2.1d, where details of the specimen, force and displacement sensors and actuators are provided. It also shows the electrical contact pads A-A’ and B-B’ for specimen heating and C-C’ for mechanical actuation. Figure 2.1e shows a schematic diagram of the device design, where the specimen is integrated with a flexure beam force sensor and a set thermal actuator beams. The 20 micron deep and 10 microns wide thermal actuator beams expand due to Joule heating [28], which loads both the specimen and the force sensing beam. The force on the specimen can be obtained from the force equilibrium diagram shown in Figure 2.1f. If the stiffness values of the force sensor and the specimen are k_{fs} and k_{sp} respectively, then the elongation and force in the specimen are given by,

$$\delta_{specimen} = \delta_1 - \delta_2\,;\ F_{specimen} = k_{fs}\delta_2 = \left(\frac{24\kappa}{L_{fs}{}^{3}}\right)\delta_2 \tag{1}$$

where δ_1 and δ_2, are displacements in the thermal actuator and force sensing beams respectively and κ is the in-plane flexural rigidity of the force sensing beam. These displacement values can be read directly from the TEM images. The actuators operate below 100 °C for which infrared microscopy (Figure 2.1g) suggests no temperature influence on the specimen.

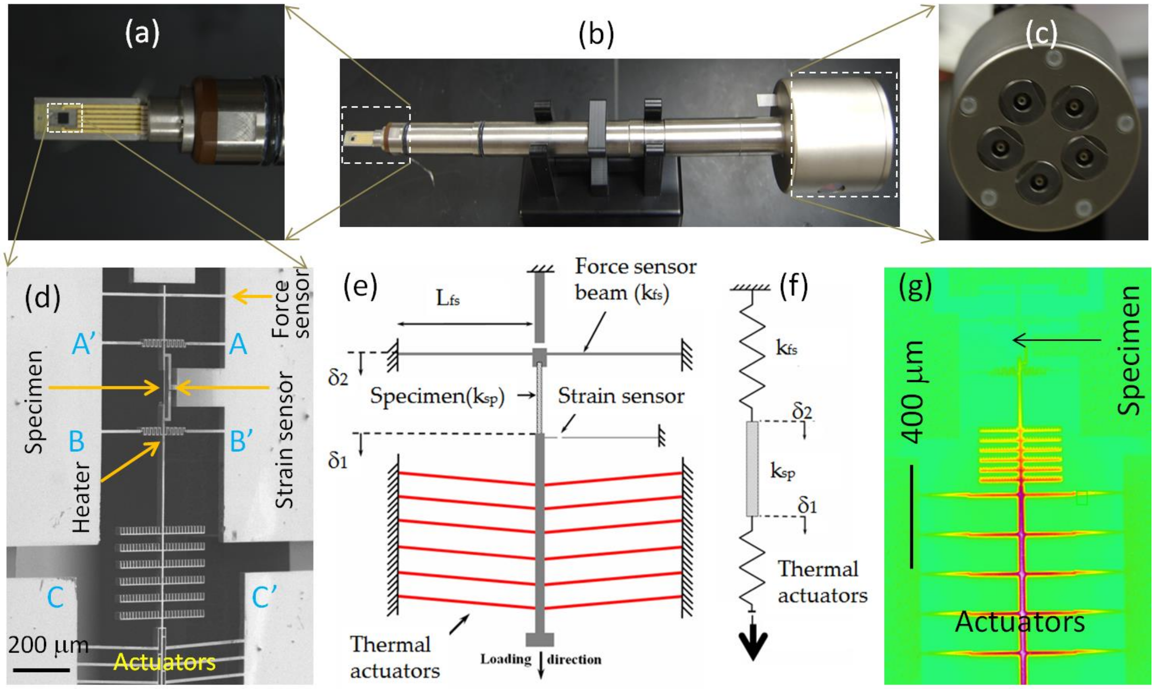
(a)
(b)
(c)
(d)
Force sensor
A'
A
Specimen
B
B'
Strain sensor
Heater
C
C'
200 µm
Actuators
(e)
L_{fs}
Force sensor beam (k_{fs})
δ2
Specimen(k_{sp})
Strain sensor
δ1
Thermal actuators
Loading direction
(f)
k_{fs}
δ2
k_{sp}
δ1
Thermal actuators
(g)
400 µm
Specimen
Actuators

Figure 2.1. Experimental setup, (a, b, c) front, side and rear ends of the in-situ electrical biasing TEM specimen holder respectively (d) zoomed view of the MEMS thin film tensile testing chip showing specimen, actuators and sensors (e, f) schematic representation and force equilibrium diagram of the test chip respectively [50] (g) infrared image of the test chip after actuation [51].

It is important to note that the specimens are co-fabricated with the MEMS devices, so that specimen alignment and gripping issues are automatically achieved during nanofabrication. In this study, we fabricated 100 nm thick, 99.97% pure zirconium films as 100 microns long and 5 microns wide specimens. Figure 2.2 shows the TEM bright field image and selected area diffraction pattern. The average grain size of the 100 nm thick films is <10 nm.

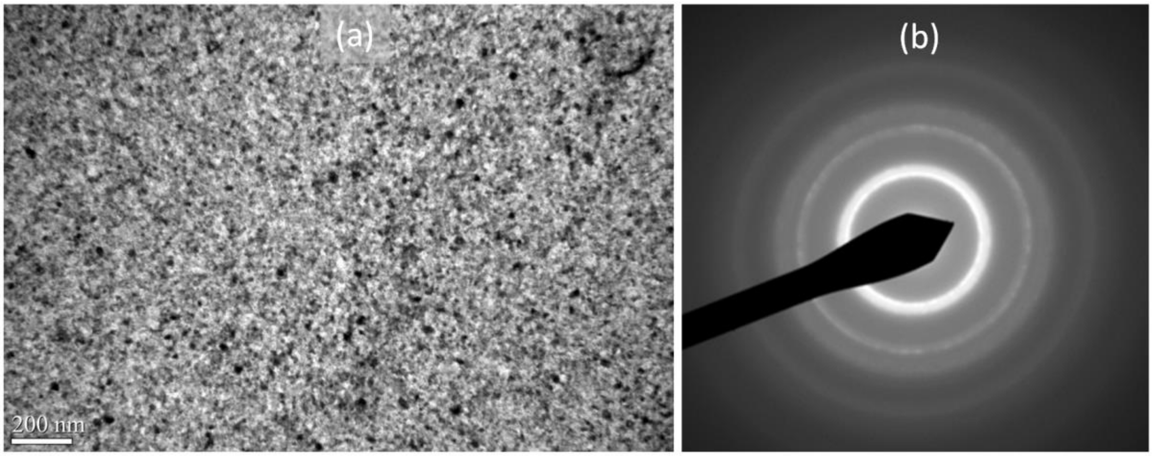

Figure 2.2. (a) Bright-field TEM image of the as-deposited specimen and (b) selected area electron diffraction pattern [51].

2.1.3 Experimental Results and Discussion

In-situ TEM tests were performed on a set of ten as-deposited zirconium specimens, which was followed by calibration of the force sensor beam to ensure experimental accuracy. Figure 2.3a shows a typical stress-strain diagram, where yield stress is around 500 MPa and fracture stress and strain are about 900 MPa and 1.5% respectively. In comparison, the yield stress and fracture strain of bulk poly-crystalline zirconium is about 250 MPa and 40% respectively. The inset in Figure 2.3a is a zoomed view of the linear elastic part of the overall stress-strain diagram. The Young’s modulus value was measured to be about 87.6 MPa, which validates the satisfactory calibration of the procedure since the accepted value in the literature is about 90 GPa. The experimental results for the <10 nm grain size specimens show remarkable size effect when compared to the literature [40], especially in terms of plastic strain. For about 300 nm grain size [40], the observed plastic strain of 15% overshadows our observation of only 1.5% strain for >10 nm grain size. Such size effect could also emanate from the specimen (bulk nanocrystal vs thin film nanocrystal), since thin films have orders of magnitude higher surface area compared to the bulk. As a result, thin film nanocrystals may show strain hardening (as suggested by out in-situ TEM experiments) but the dislocations may escape through the surface, leaving atomic scale defects in the surface to trigger fracture at very low strain. The very small value of the plastic strain in this study can also be explained by the appearance of relative large voids as shown in Figure 2.3b. It is well known that mechanical deformation is localized at the grain boundaries in nanocrystalline metals. In addition the strain incompatibility among neighboring grains of different crystallographic orientations may pronounce the grain boundary stress, creating voids at the grain boundaries.

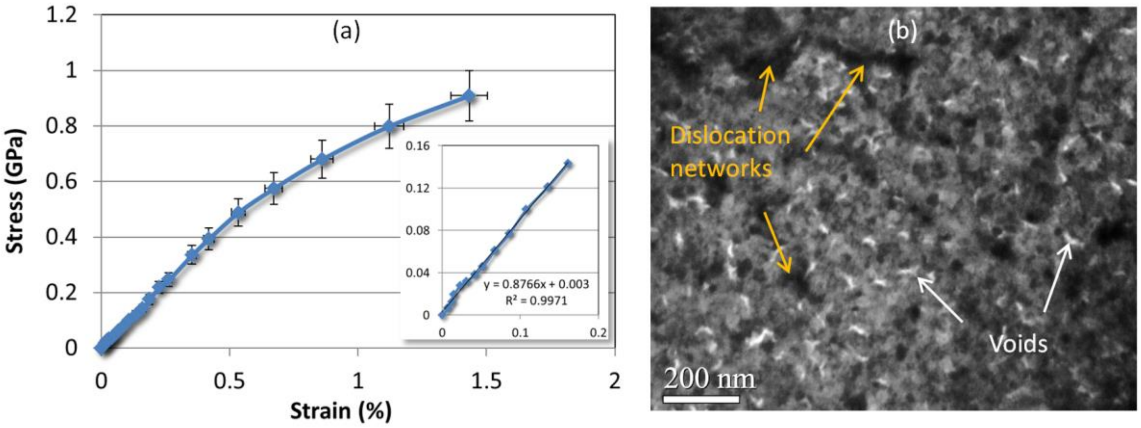

Figure 2.3. (a) Representative stress-strain diagram for nanocrystaline zirconium specimens measured in situ inside a TEM (b) nanoscale voids appears at the grain boundaries at the onset of fracture [51].

To study the effects of external stimuli (thermal, electrical, mechanical) on grain growth kinetics, we passed electrical current through the specimen using contact pads A-B in Figure 2.1d. The dc current creates mechanical stress (compressive stresses near anode and tensile stresses near cathode) and temperature fields in the specimen, which trigger the grain boundary diffusion processes. This is similar to electro-migration, except we applied one order of magnitude lower current density to avoid any damage. The results are shown in Figure 2.4 for various current levels and polarity. The highest temperature in the specimen is about 350°C, which is only 20% of the melting temperature, which suggests that synergy of multiple stimuli has stronger effects than a single stimuli.

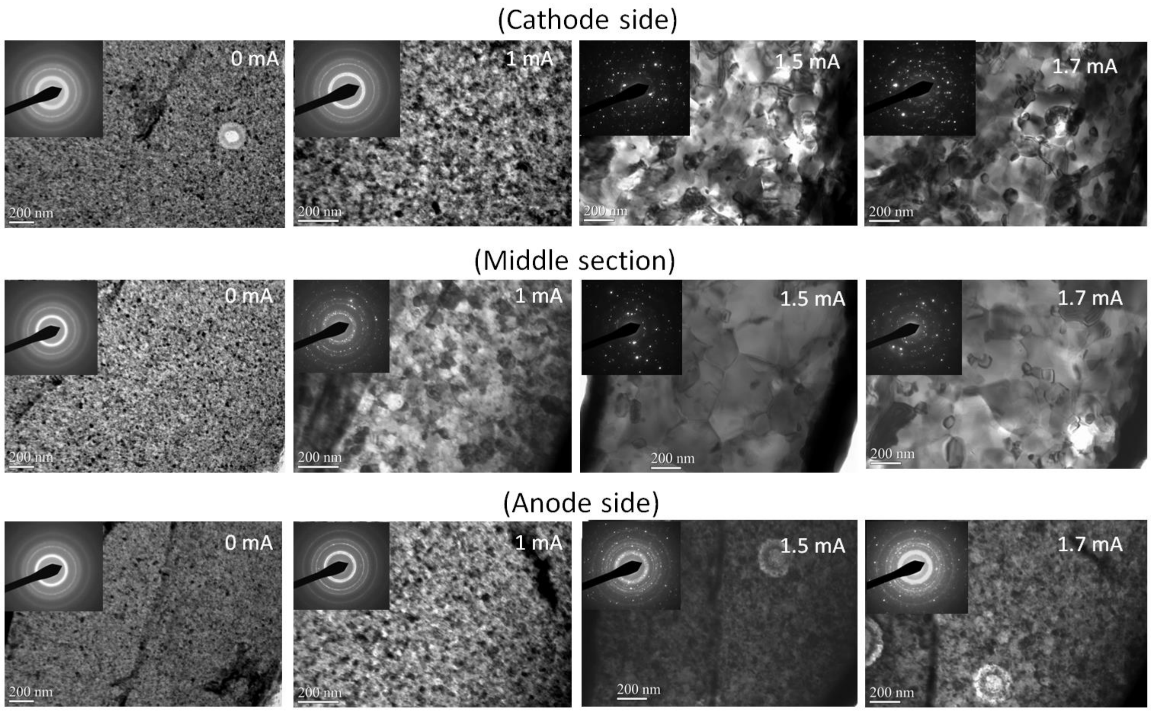

Figure 2.4. Grain growth as function of polarity and magnitude of dc electrical current passed through the freestanding specimen [51].

The literature suggests decrease of strength below a critical average grain size, known as the inverse Hall-Petch relationship. This size is around 15 nm for most FCC metals [52]. Since no study exists for nanocrystalline zirconium, we attempted to grow the grain size to about 25 nm by passing a current at density of $0.5 \times 10^6 A/cm^2$ through the specimen for about 5 min. The microstructure and selected area diffraction pattern after grain growth are shown in Figure 2.5(a) and 2.5(b). Figure 2.5(c) shows a typical stress-strain diagram for average grain size of 25 nm. The yield stress is around 800 MPa, which is higher than the bulk (250 MPa) or 5-10 nm grain size (500 MPa). This suggests inverse Hall-Petch relationship, however extensive experimentation is needed to substantiate this phenomenon. Unfortunately, the proposed electro-migration stress technique is difficult for more than 500% growth and largest grain size studies was about 50 nm. Interestingly, the measured yield stress was in the same range as the 25 nm grain sized specimens considering experimental error of about 7%. Therefore the suggested observation of inverse Hall-Petch behavior needs to be confirmed after s that other factors, such as strain rate, temperature and grain size distribution may play role in the mechanical properties for this grain size range [52].

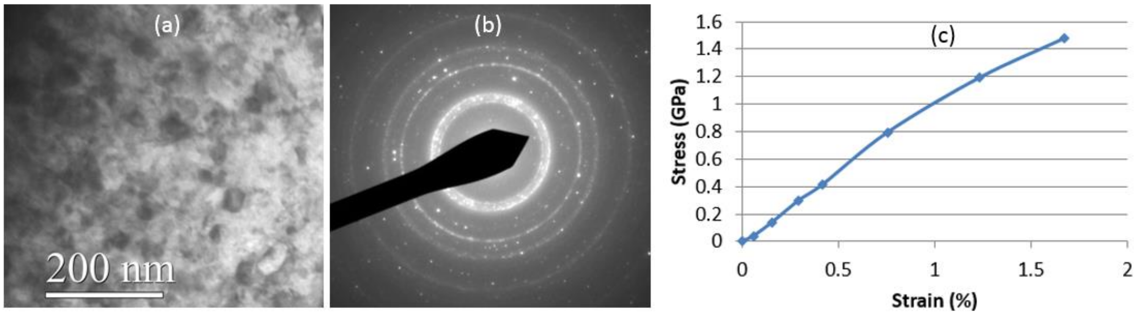

Figure 2.5. (a) Bright-field TEM image of specimen after 5 mins of current flow at $0.5 \times 10^6 A/cm^2$ density (b) TEM selected area electron diffraction (c) Stress-strain curve [51].

2.1.4 Conclusion

We presented in-situ TEM mechanical test results for nanocrystalline zirconium thin films. The measured Young's modulus of as-deposited specimen with an average grain size 5-10nm is 85-90 GPa which falls very close to the bulk value. In-situ TEM tests showed yielding around 400-500 MPa and fracture strain around 1.5-2% strain. In comparison, ultra-fine grained zirconium in the literature shows yield strength of 500 MPa and 15% fracture strain. The measured yield stress of zirconium thin films with an average grain size 25 nm is about 60% higher than that of as deposited specimen with an average gain size of 5-10 nm, which suggests inverse Hall-Petch behavior in nanocrystalline zirconium.

2.2 Low Temperature Viscoelasticity in Nanocrystalline Nickel Films

Metals typically do not exhibit viscoelastic deformation. However, grain size effects can render grain boundaries in nanocrystalline metals viscous. Modeling the nanocrystallites as linear elastic elements embedded in a viscous network of grain boundaries, the overall response of nanocrystalline metals can be viscoelastic even at lower temperatures. To investigate this hypothesis, we measured viscoelastic response of 100 nanometers thick freestanding nickel films at temperatures up to 425 K. Experimental results show about two orders of magnitude lower viscosity compared to the bulk, suggesting that diffusion enhanced mobility of grain boundary atoms may be responsible for such pronounced viscoelasticity.

2.2.1 Introduction

Thin films are prevalently used in micro-electronic and micro-electromechanical (MEMS) systems [53]. Reliability of these devices, particularly those involving dynamic loading such as resonators, is influenced by time dependent behavior of the thin films [54]. Typically, metals do not show viscoelasticity; they are viscoplastic only at higher temperatures [55]. Nevertheless, thin films exhibit significant deviation from bulk behavior, attributed to their smaller grain size (on the order of the film thickness), larger surface area over volume ratio and most importantly, different defect structures [56]. The literature contains evidence of lower relaxation times for metal thin films even at ambient temperature [57-59], which suggests that viscosity of these solids decrease with grain size. However, these studies involve plastic deformation and whether size effect can induce viscoelasticity in metals is yet to be established, which motivates the present study. We propose a hypothesis that size effect enhanced atomic mobility of the surface and grain boundary atoms may lead deformation that is time sensitive yet reversible. Accordingly, we envision a model where the glassy crystal interiors are embedded in viscous grain boundary matrix that become more rubbery and damped due to increased temperature sensitivity. In this paper, we present preliminary evidence of viscoelastic deformation of nanocrystalline nickel films at room and elevated (up to 425 K) temperatures to support this hypothesis.

2.2.2 Experimental Details

Figure 2.6a shows the experimental setup, where a micro-electro-mechanical system (MEMS) device integrates a freestanding thin film specimen, an electro-thermal actuator and a microheater to apply uniaxial tensile stress and temperature on the specimen respectively. The 100 nm thick, 99.99% pure Ni films were first evaporated on a silicon-on-insulator wafer and then co-fabricated with the MEMS device. The as-deposited grain size was about 10 nm. Details of the MEMs fabrication processing are given in [60]. The electro-thermal actuator and heater were calibrated for various values of input current using an infrared microscope with 0.1^{o}K resolution.

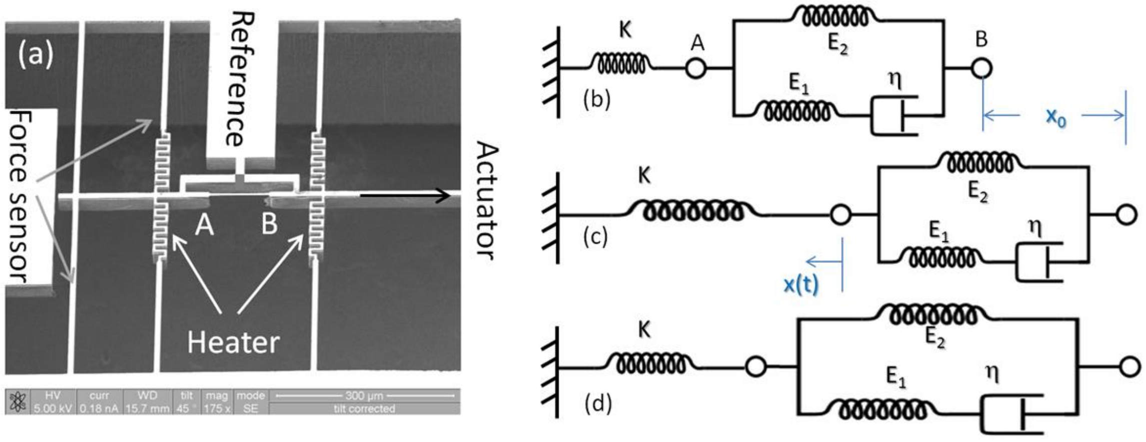

Figure 2.6. (a) Scanning electron micrograph of the MEMS device integrating a freestanding thin film specimen with microheaters, force sensors and electro-thermal actuators (not shown), (b, c, d) schematic rendering of the force sensor and specimen before, during and after a step loading [61].

Figure 2.6b schematically shows the force sensor beams (with total stiffness, K) and the specimen gauge section (marked as A-B in Figure 2.6a) in form of a standard linear solid [62]. The characteristic equation for a three parameter standard anelastic (Zener) solid is given as,

$$\frac{\eta}{E_1}(E_1+E_2)\dot{\varepsilon}+E_2\varepsilon=\frac{\eta}{E_1}\dot{\sigma}+\sigma \tag{1}$$

Here, E_1 and E_2 are the *glassy* and *rubbery* moduli and η is the viscoelastic damping coefficient of the material. As shown in Figure 2.6c, a step displacement of x_0 is applied at time t = 0 by supplying a step voltage on the actuator, which is kept constant for rest of the experiment. The displacement of the actuator end of the specimen (point B) is accommodated instantaneously by the force sensor beam, giving rise to initial stress σ_0 = K x_0/A, where K is the stiffness of the force sensing beam and A is the cross-sectional area of the specimen. This step displacement is also accommodated by the E_1 and E_2 components of the Zener solid, giving rise to instantaneous strain in the specimen, $\varepsilon_0 = \sigma_0/(E_1+E_2)$. For time t >0, the specimen relaxes and so does the force sensor beam (Figure 2.6d), thereby decreasing the effective stress level. The displacements are measured from digital video recording from the microscope with a digital image correlation (DIC) technique.

To model this simultaneous creep-stress relaxation phenomenon, we note that the stress and strain on the specimen at any time are given by,

$$\sigma(t) = \sigma_0 - K\frac{x(t)}{A};\;\; \varepsilon(t) = \varepsilon_0 + \frac{x(t)}{L} \tag{2}$$

Where x(t) is measured as the displacement of the force sensing beam as shown in Figure 2.6c and L is the length of the specimen. Rearranging using the expressions for stress and strain given by equation 1, for t >0,

$$\left[\frac{\eta}{E_1}\frac{E_1+E_2}{L} + \frac{\eta}{E_1}\frac{K}{A}\right]\dot{x} + \left[\frac{E_2}{L} + \frac{K}{A}\right]x = \sigma_0 \tag{3}$$

The solution to this ordinary differential equation is

$$x = \frac{b}{a} + \left(\frac{b}{a} - x_0\right)e^{-at}, \text{ where } a = \left[\frac{\left[\frac{E_2}{L}+\frac{K}{A}\right]}{\frac{\eta}{E_1}\left[\frac{E_1+E_2}{L}+\frac{K}{A}\right]}\right] \text{ and } b = \left[\frac{\sigma_0 - \varepsilon_0 E_2}{\frac{\eta}{E_1}\left[\frac{E_1+E_2}{L}+\frac{K}{A}\right]}\right] \tag{4}$$

The unknown parameters E_1, E_2 and η can be obtained by curve fitting the force sensor beam displacement data, x(t) with the model (equation 4) using a generalized reduced gradient algorithm.

2.2.3 Results and Discussion

Figure 2.7 shows the experimental results on freestanding 100 nm thick nickel films at temperatures ranging from 300 to 425 K, where the displacement of the left side (point A in Figure 2.6a) is plotted against time. Also plotted is the model (equation 4) prediction for the best fitted parameter (E_1, E_2 and η) values. The stiffness of the force sensing beams, K, was about 100 N/m, while specimen gauge length, L, was 50 microns for both cases.

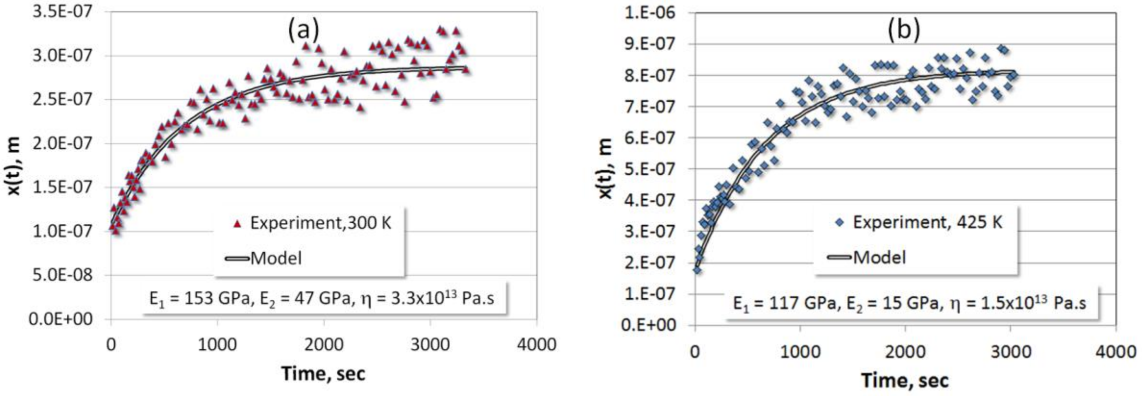

Figure 2.7. Time vs. displacement plot of the point marked B on the specimen at (a) 275 K and (b) 425 K temperatures [61].

An important consideration in these measurements is the reversibility of the deformation, so that the choice of the viscoelastic model is justified. We therefore performed uniaxial tensile testing on these freestanding thin films. Figure 2.8 shows the results of a quasi-static (about 5 minutes time interval between each measurement) room temperature experiment. The loading segment was approximately linear till 1.5% strain. In comparison, the strain (ε_0) levels in the time dependent tests (Figures 2.7a and 2.7b) after instantaneous loading are 0.21% and 0.35% respectively. These values are therefore in the elastic regime. The specimens were initially slightly buckled condition, which were straightened to the zero stress and strain reference point before the experiments.

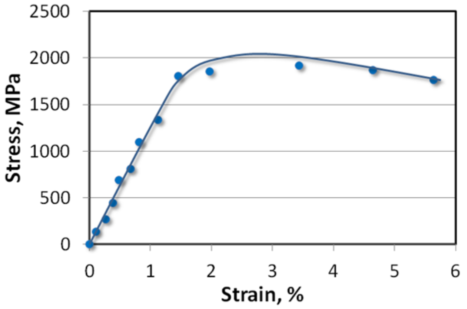

Figure 2.8. Quasi-static uniaxial tensile stress-strain diagram for the freestanding nickel specimens.

Figure 2.9a summarizes the obtained results for temperature range 300 to 425 K. For these temperatures, the glassy modulus (E_1) was measured to be 153 GPa and 117 GPa while the rubbery modulus (E_2) followed similar trend with 49 GPa and 15 GPa respectively. Finally, the damping coefficient η was measured to be 3.3×10^{13} Pa.s and 1.5×10^{13} Pa.s at these temperatures. In absence of nickel data, these values compare about two orders of magnitude smaller than viscosity of aluminum (2.2×10^{15} Pa.s) [63]. Since the damping is predominantly contributed by the grain boundaries, we hypothesize that its viscosity is lowered by enhanced atomic mobility arising from size effects on diffusive displacement. At the same time, the steady state behavior is not plastic because the crystalline components of the specimens are predominantly elastically loaded. Figure 2.9b shows the plot of $\log(\eta)$ against 1/RT, where R is the universal gas constant. The slope of this curve is 3.13 KJ/mole, which is the creep activation energy for the viscous damping coefficient. This value is approximately two orders of magnitude smaller than the bulk (276 KJ/mole) and nanocrystalline (115 KJ/mole) nickel [64]. The present study is unique because of the freestanding nature of the specimen, which means that the surface diffusivity could play a prominent role. Surface diffusivity in nickel is 3 orders of magnitude higher than the grain boundary diffusion [58]. For copper, it is 3 and 16 orders of magnitude higher than grain boundaries and the lattice respectively [65]. Our recent study on grain growth at low temperature and stress supports this explanation, where we observed unusually large grain growth in nickel thin films as a deformation mechanism.

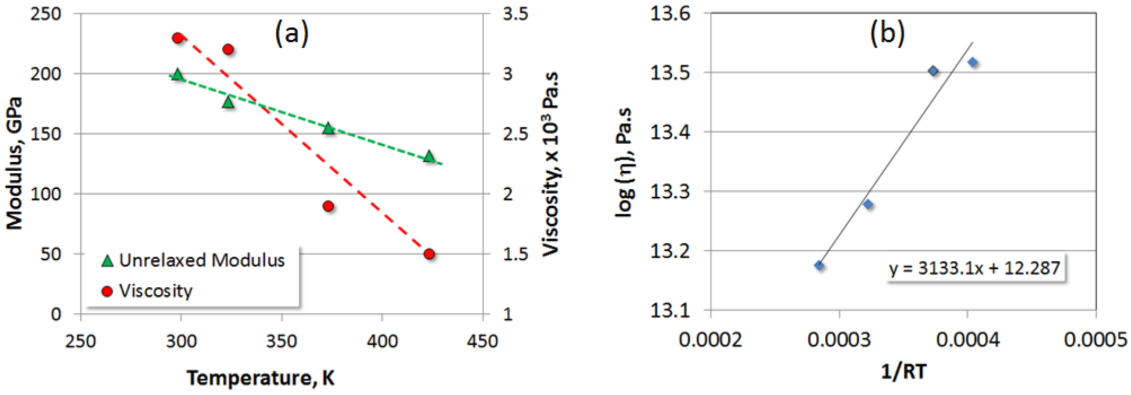

Figure 2.9. (a) Variation of the unrelaxed modulus and the viscous damping coefficient with temperature, (b) calculation of the activation energy for the viscous damping element [61].

More intriguing aspect of the experimental results is the weaker influence of temperature on viscosity. The rate of decrease of the viscous damping coefficient is remarkably lower than the bulk. No such data is available for nickel, but for aluminum the viscosity decreases 10^7 times from room temperature to 425 K. These trends of weaker temperature dependence (than bulk) is, however, cross-validates our hypothesis on the role of surface diffusivity in the paragraph above. Surface diffusivity may have higher magnitudes compared to the grain boundaries or the lattice, but it also shows the weakest temperature dependence compared to the grain boundary and the lattice.

2.2.4 Conclusion

We modeled nanocrystalline metals as a standard linear elastic solid, where the crystallite parts are embedded in a viscous grain boundary network. We hypothesize that the grain boundaries exhibit enhanced atomic mobility due to size and temperature effects on diffusion, yet the global behavior of the specimen remains linear elastic because of the predominance of the linear elastic crystallites. Experimental results on 100 nm thick (average grain size 10 nm) freestanding nickel specimens at temperatures from 300 to 425 K support this hypothesis reasonably well. The viscosity of solid nickel ranged from 3.3×10^{13} Pa.s to 1.5×10^{13} Pa.s at these temperatures, which are about two orders of magnitude smaller than that expected for metals and are also less sensitive to temperature compared to bulk. We propose that for freestanding thin films, surface diffusion dominates other pathways (grain boundary and lattice), which can explain the lower viscosity and weaker sensitivity to temperature.

2.3 Thermo-Mechanical Coupling in Zirconium Thin Films

At the bulk scale, thermal conductivity of metals is not coupled with mechanical strain. However, this may not be the same for grain sizes below the electron mean free paths, for which mechanical deformation mechanism and volume fraction of grain boundaries are drastically different from the bulk. To investigate this hypothesis of grain size induced thermo-mechanical coupling, we developed an experimental setup to measure the thermal conductivity of 100 nm thick freestanding nanocrystalline zirconium (Zr) films as a function of externally applied mechanical strain. Experimental results show strong mechanical strain-thermal conductivity coupling, thermal conductivity of Zr film dropped from 20 W/m-K to 13 W/m-K with an increasing strain from 0 % to 1.24 %. Thermal conductivity of Zr film was also measured as a function of average grain size ranging from as-deposited 10 nm to as-grown 250 nm. The results clearly show that for grain sizes above 10 nm, mechanical strain has no influence over thermal conductivity, which supports the proposed hypothesis.

2.3.1 Literature Review and Objective

Thermal transport in thin film components of microscale devices and systems, opto – electronics and energy conversion devices is receiving more attention because of the continuing trend in miniaturization [66-68]. Dissipative power density of these devices scales as L^{-1}, where L is the length scale [69], which renders heat transfer in thin films critical for device performance and reliability. These devices experience varying levels of mechanical strain during their fabrication processes involving high temperatures or during device operation. Most studies typically focus on the temperature dependence of thermal or mechanical properties [15, 16, 70, 71] and the literature lacks systematic investigation on the mechanical strain – thermal conductivity coupling. The few investigations involving mechanical deformation [72, 73] involved only intrinsic or residual strains. Also, no appreciable thermal-mechanical coupling was observed in these studies because of the large grain size. For large grains, dislocations dominate the deformation and it is well known that they scatter electrons or phonons only weakly. The advances in materials processing and computational materials science has highlighted the needs for coupling effects at the smaller length-scales, where mechanical strain could possibly be coupled with thermal conductivity as a size effect [74, 75]. Lee et al. [26] also reported strong strain influence on thermal conductivity of nanocrystalline aluminum with an average grain size of 50 nm. However, their specimens were attached to the substrate, which makes it very difficult to isolate the role of mechanical strain from the substrate accurately. A more recent study on ferroelastic $Pb(Zr_{0.3}Ti_{0.7})O_3$ films with nanoscale domain structure showed up to 11 % change in thermal conductivity due to the electrical field assisted domain re-structuring [76]. Such active and reversible tuning of thermal conductivity shows that phonon-based transport can also be tuned by mechanical strain.

It is commonly accepted that mechanical deformation can influence thermal transport, because it affects the scattering mechanisms of thermal energy carriers (electrons and phonons).

For example, electrons transfer heat in metals and are scattered by dislocations and grain boundaries. But at the bulk and micro scales where dislocation is the dominant mechanism, the thermal-mechanical coupling in metals is very weak, if any. This is because appreciable scattering of electrons by dislocations only happens at temperatures less than 100 K [77, 78]. However, thermal transport in materials is known to be size dependent at the nanoscale [79-82]. Specially, metal thin films show stronger size effect when the film thickness or grain size is smaller than or comparable to electron mean free path [83-85].

Thermal transport in pure metals contains both components of electrons and phonons. According to conventional physics, free electrons contribute to heat conduction in pure metals more than the lattice vibrations (phonons) [86]. While tacitly assumed, the question is open whether the same is true at the nanoscale. It has been reported both experimentally and theoretically that the phonon specific heat in low-dimensional system would be enhanced to a large extent [87, 88]. Heino & Ristolainen [89] computed the thermal conductivities by phonons in several metals and found they are very small compared to the experimental values due to the role of electrons. Chantrenne et al. [90] investigated the electron and phonon contributions on the thermal conductivity of aluminum films with a thickness range from 2 to 20 nm and found that it remarkably dropped below the bulk value. Feng et al. [91] studied the in-plane thermal conductivity of nanoscale copper films and concluded that even though the lattice contribution in metallic films is enhanced compared to that in bulk metal, but it is still relatively small compared to that of electrons.

The present work is motivated by the fact that the conventional physical laws break down at or below a critical length scale [1], where size effects are not only shown in individual domains, but also in the coupling of these domains. As the grain size is reduced below ~50 nm, electrons and phonons are primarily scattered by free surfaces and grain boundaries [92] instead of dislocation-based deformation mechanism which mainly takes place at the grain interior. It has been reported that ultra-fine grains are often dislocation-starved both experimentally [93, 94] and theoretically

[95, 96]. At the nanoscale, the very high volume fraction of grain boundaries (two-dimensional microstructures) plays a critical role [97]. As previously mentioned, the thermal conduction in nanoscale metallic films is still dominated by the role of electrons. The change of thermal conductivity because of mechanical strain must be attributed to the change of electron scattering due to mechanical deformation. The literature suggests that most of the externally applied deformation gets accommodated in grain boundaries at nanoscale [98-100] as opposing to grain interiors at bulk scale, thus increasing the intensity of deformation and related carrier scattering. We hypothesize that this localization of mechanical strain results in increased defects at grain boundaries, which causes the change in thermal transport.

2.3.2 Experimental Setup

To investigate the effect of deformation on thermal conductivity, an experimental setup that can apply uniaxial strain on a freestanding thin film while thermal properties are being measured is required. We achieve this by designing and fabricating a micro-electro-mechanical (MEMS) tensile testing device which can be accommodated in a custom-made transmission electron microscope (TEM) holder allowing in-situ investigation. Figure 2.10a shows a SEM image of the fabricated device integrating freestanding specimen, stress and strain sensors and electro-thermal actuators. The MEMS has three pairs of electrical contact pads, A-A’ and B-B’ for heating either end of the specimen without passing current through the specimen, C-C’ for thermal actuation, A-B’ or A’-B for passing current through specimen. The freestanding specimen is shown in Figure 2.10b at an angle of 52 degree of tilt. We chose V-shaped electro-thermal actuators for uniaxial displacement loading upon actuation.

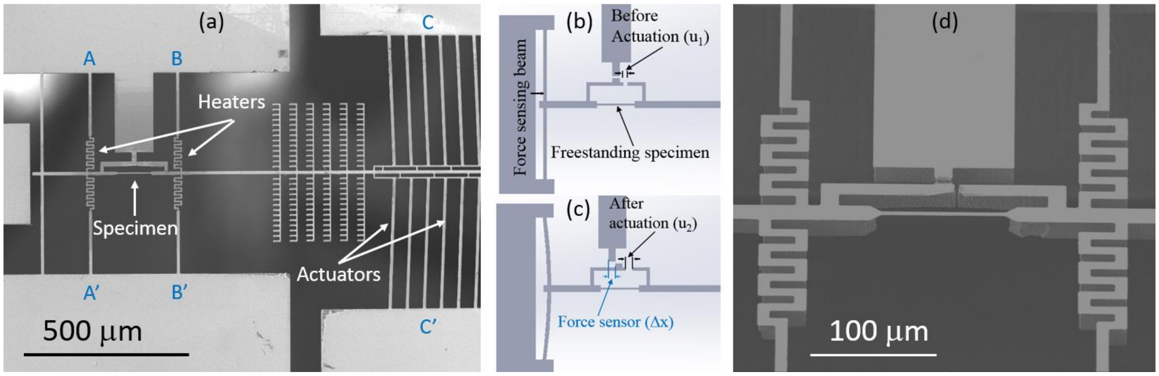

Figure 2.10. Experimental setup, (a) SEM image of the MEMS thin film tensile testing chip showing specimen, actuators and sensors (b, c) schematic diagram showing displacement based force and strain measurement (d) SEM image of the heaters and the freestanding specimen. schematic representation and force equilibrium diagram of the test chip respectively [101].

Figure 2.10c shows a schematic diagram of the device design, where the specimen is co-fabricated with a force sensor beam and a set of thermal actuator beams. These beams are micro machined from heavily doped silicon-on-insulator (SOI) wafers. By passing current through C-C’, the thermal actuator beams will expand due to Joule heating to apply load on both the specimen and the force sensing beam. The force on the specimen can be calculated from the force equilibrium diagram shown in Figure 2.10d. If the stiffness values of the force sensor and the specimen are k_{fs} and k_{sp} respectively, then the elongation and force in the specimen are given by [101, 102],

$$\delta_{specimen} = u_2 - u_1 \text{ ; } F_{specimen} = k_{fs}\Delta x = (\frac{192k}{L_{fs}^3})\Delta x \qquad (1)$$

where δ_1 and δ_2, are displacements in the thermal actuator and force sensing beams respectively and κ is the in-plane flexural rigidity of the force sensing beam. These displacement values can be obtained directly from the TEM images. The maximum achievable stress and strain values depend on the stiffness of the force sensor and the specimen dimension; both of which can be controlled accurately during the fabrication process. The maximum displacement of the thermal actuator is limited to 5 microns in order to achieve high precision displacements. For a 50 micron long specimen, this results in maximum of 10 % strain.

The chip shown in Figure 2.10a is fabricated using conventional nanofabrication techniques involving photolithography, reactive ion etching and evaporation of the metal film. 100 nm thick, 99.97 % pure Zr thin film is first deposited on silicon on insulation (SOI) substrate using e-beam evaporator and then the device design shown in Figure 2.10a is patterned on the wafer using standard photo-lithography. Micro-heaters, force sensors and actuators are fabricated by using deep reactive ion etching (DRIE) to etch through the patterned device layer while specimen is protected by photoresist pattern. After the backside patterning, the SOI wafer is mounted on a carrier wafer using photoresist. Another DRIE is used to etch through the backside handle layer and make the whole front side device layer free-standing. After the backside etching done, the SiO_2 layer just beneath the device layer is removed by a reactive ion etching process using CF_4 chemistry. Then the SOI wafer is separated from the carrier wafer using Nano PG Remover. Finally, substrate under the specimen is isotropically etched to make the thin film freestanding while a physical shadow mask is used to protect the other parts. Figure 2.11 shows the fabrication details. Such co-fabrication ensures perfect specimen alignment and gripping [93]. After fabrication, the device is wire bonded to make the proper electrical connection and mounted on either the gold coated ceramic pads for in-situ infrared microscope measurement or on a TEM specimen holder with electrical biasing capability for in-situ TEM investigation.

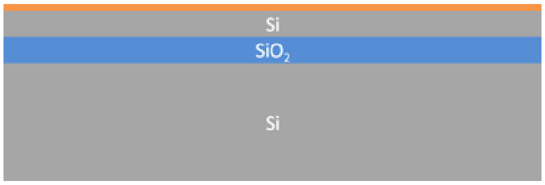

a. Zirconium is evaporated on the top of SOI wafer.

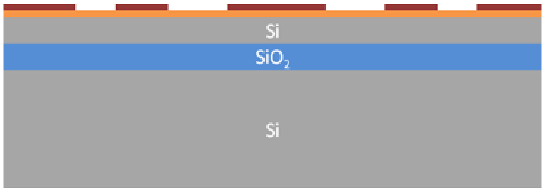

b. Device layer is patterned using lithography.

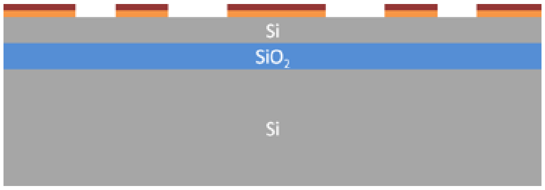

c. Zirconium is etched away on the top.

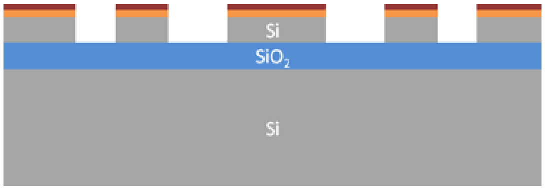

d. Front-side DRIE through the device layer is done.

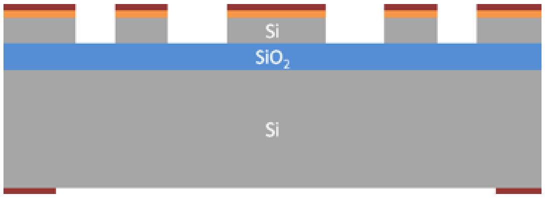

e. Backside opening is patterned using lithography.

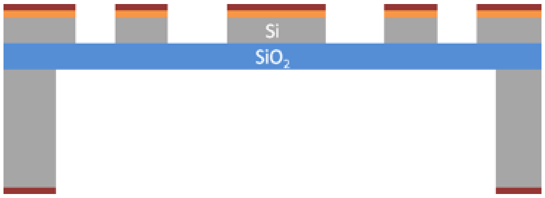

f. Backside DRIE through the handle layer is done.

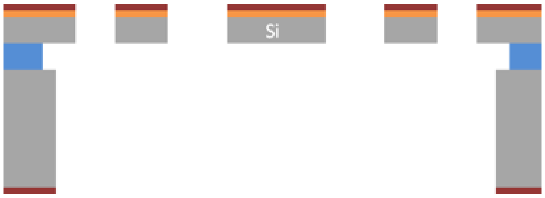

g. Oxide layer is etched using CF4.

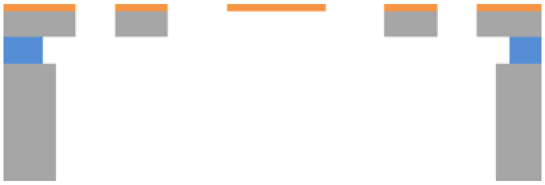

h. Silicon underneath Zirconium thin film is etched and photo-resist is removed.

Figure 2.11. Fabrication details of MEMS thermo-mechanical testing device.

Figure 2.12a shows the TEM bright field image and selected area diffraction pattern of the as-deposited specimen. The average grain size of the 100 nm thick films is around 10 nm. Nanocrystalline structure is also evident from the selected area diffraction pattern, which shows diffused rings representing grains with various crystallographic orientations. Grain size and thickness are two parameters that make thin film mechanical properties different from the bulk. For example, the yield stress and fracture strain of bulk poly-crystalline Zr are about 400 MPa and 24 % respectively [42]. For 100 nm grain size and 80 microns foil thickness, these values change to 850 MPa and 2.7 5% respectively. To accurately characterize our 100 nm thick and 10 nm grain size specimens, we performed uniaxial tensile tests using the procedure described above. The stress-strain diagram, shown in Figure 2.12b, is remarkable linear. This suggests that dislocation based plasticity is absent due to the extreme microstructural (grain size) and dimensional (film thickness) constraints. As a result, the fracture stress is very high (about 1.2 GPa) at the expense of fracture strain (1.5 %).

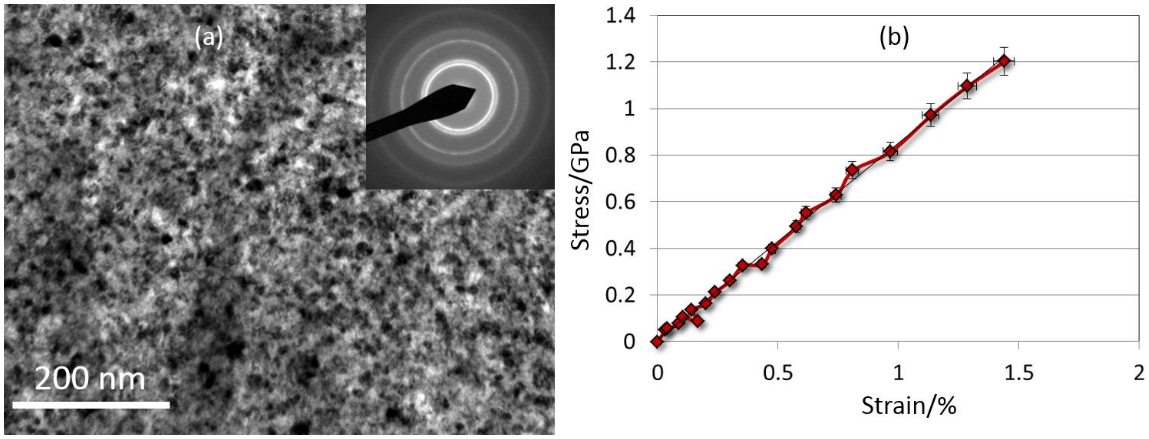

Figure 2.12. (a) Bright-field TEM image of the as-deposited specimen, the inset shows selected area electron diffraction pattern and (b) Stress-strain diagram of as deposited specimen.

Thermal conductivity measurements were conducted under an infrared (IR) microscope. Figure 2.13a shows a typical thermal mapping from the IR microscope when the electric contact pads B-B' in Figure 2.10a are powered up. The freestanding specimen is modeled as a simple extended fin as shown in Figure 2.13b. Energy balance is applied on a control volume of the specimen with a length of Δx.

$$kA\frac{dT}{dx}\bigg|_{x} - kA\frac{dT}{dx}\bigg|_{x+\Delta x} = hP\Delta x(T - T_{\infty}) \tag{2}$$

where k is thermal conductivity of specimen, A and P are cross-sectional area and perimeter, h is the overall heat transfer coefficient (summation of convection h_c and radiation h_r) and T_{∞} is the ambient temperature. For small temperature difference, h can be expressed as [103]:

$$h = \varepsilon\sigma 4T_{amb}^{3} + h_c \tag{3}$$

where ε is the emissivity (0.48 [104] for Zr)and σ is the Stefan-Boltzmann constant (5.67×10^{-8} W m^{-2} K^{-4}). The general solution of Equation 1 is:

$$\theta = C_1 e^{mx} + C_2 e^{-mx} \tag{4}$$

where θ = (T-T$_\infty$) and $m = \sqrt{hP/kA}$.

C$_1$ and C$_2$ can be obtained by applying boundaries, T=T$_b$ at x=0 and T=T$_L$ at x=L. Then the solution can be given by:

$$\frac{T-T_\infty}{T_b-T_\infty} = \frac{[T_L-T_\infty/T_b-T_\infty]\sinh mL + \sinh m(L-x)}{\sinh mL} \tag{5}$$

The calculated temperature profile T can be plotted as a function of *k* using Equation 5. If heat transfer coefficient h$_c$ is measured accurately, by matching the modeled temperature profile T with experimental data from IR microscope, thermal conductivity *k* can be measured. Figure 2.13c shows such curve fitting of the model to match it with experimental data with *k* as the only fitting parameter. The heat transfer coefficient h$_c$ can be acquired by applying energy conservation principle near the heated specimen surface [105],

$$-k_{air}A\frac{\partial}{\partial y}(T - T_{s)}\Big|_{y=0} = h_c A(T_s - T_\infty) \tag{6}$$

where, y is the perpendicular direction to the specimen length (y = 0 denotes specimen surface) and T$_s$ is the specimen temperature. The solution is given by,

$$T = T_\infty + (T_s - T_\infty) * e^{-sy} \tag{7}$$

where $s = \frac{h_c}{k_{air}}$. Rearrange equation 7,

$$ln\frac{(T-T_\infty)}{(T_s-T_\infty)} = -sy \tag{8}$$

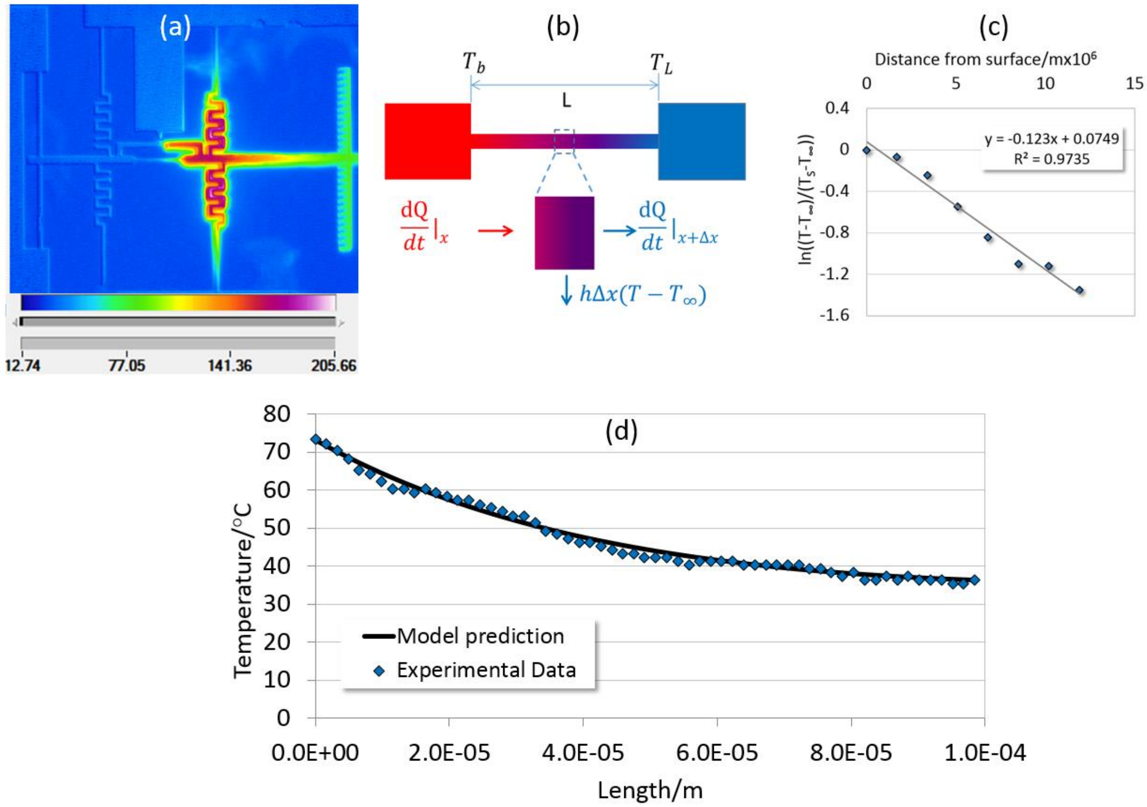

Figure 2.13. (a) Infrared thermal image of the device when one-side heater is activated; (b) Mathematical model of proposed study; (c) Estimation of heat transfer coefficient h_c by curve fitting with model; (d) Representative matching of experimental data with model prediction [106].

Here, the term *s* can be determined from the logarithm plot of the temperature difference ratio against distance y from the specimen surface with temperature T_s as shown in Figure 2.13d. This method has been validated using materials with known thermal conductivity [105]. With this experimental setup, the electro-thermal actuators are activated with different biases to apply different mechanical strains on the sample. The temperature profile is mapped using an Infrascope II thermal microscope (Quantum Focus Instruments Corporation), whose liquid nitrogen-cooled Indium-Antimonide infrared detector measures temperature with 0.1 degree K resolution. In this study, a 15x objective was used, which provides pixel to pixel resolution of about 2 microns. At each strain, the temperature profile is recorded for the calculation of thermal conductivity. The strains are measured later using optical microscope and digital image correlation technique.

2.3.3 Experimental Results and Analysis

Figure 2.14a shows comparison of the experimental temperature profile with model predictions at three different strains. Since the model is based on constant (not temperature dependent) thermal conductivity, the observed fit between the model and experiments reflects the negligible role of temperature dependent thermal conductivity at the relevant temperature range. The estimated thermal conductivity is also listed. In order to eliminate the effects of temperature on thermal conductivity, the hot end temperature of the specimen is kept almost constant during all the measurements. The thermal conductivity measured at zero strain is measured to be 20 W/m-K. Due to the lack of data on the thermal conductivity of nanocrystalline Zr, we compared the measured result with the value of bulk Zr which is around 22.6 W/m-K [107, 108]. This validates our experimental procedure since the literature suggests that thermal conductivity will decrease when the grain size becomes smaller. Figure 2.14b summarizes the obtained results with a strain range from zero to 1.244 %, where the thermal conductivity clearly decreases as we increase the strain. This behavior can be ascribed to the nanocrystalline microstructure of these thin films. When the geometric dimension of specimen or the grain sizes go down to nanoscale, it becomes increasingly difficult for the grain interiors to accommodate the external deformations. For example, in aluminum, dislocations may cease to exist in grains as large as 60 nm [93, 94]. Therefore, mechanical deformation mechanisms for grain sizes smaller than about 50 nm are basically different from the bulk ones which is not only due to absence of dislocations but also very high volume fraction of the grain boundaries [1]. Absent of dislocations in the grain interior, the grain boundaries primarily accommodate the applied strain [85]. To accomplish this, the grain boundaries must slide, rotate or emit dislocations that also move along the grain boundaries as strain is applied [92]. The scattering of electrons by grain boundaries will be enhanced by these grain motions [26]. Therefore, we hypothesize that the motion of grain boundaries resulted from strain localization is the primary mechanism behind thermal-strain coupling.

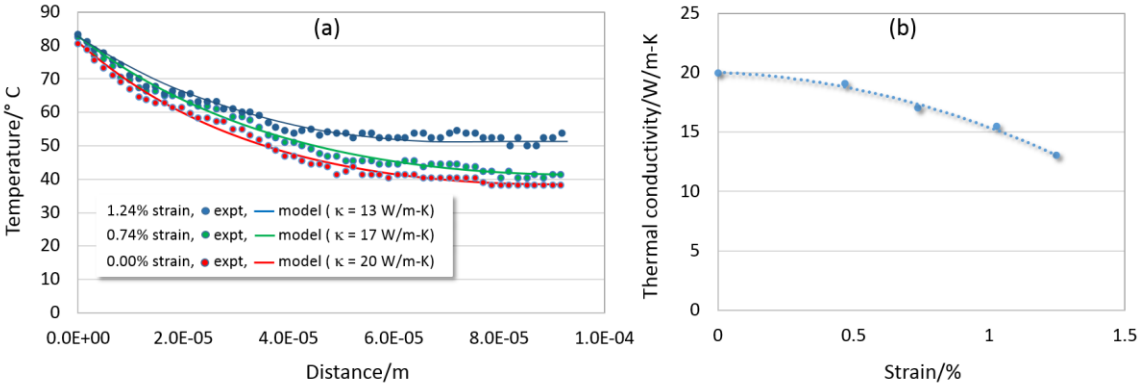

Figure 2.14. Experimental results for as-deposited specimens with 10 nm grain size (a) Comparison of experimental temperature profile with model prediction at various strains; (b) Plot of measured thermal conductivity as a function of externally applied mechanical strain [106].

To further verify our original hypothesis that mechanical deformation is coupled only in the grain size range that is comparable to (or smaller than) the electron mean free path, we repeated the experiments shown in Figure 2.14 as a function of grain size. The electron mean free path in Zr at room temperature is about 10 nm [109], which is just about the grain size of our specimens. For the as-deposited specimens, we observed remarkable thermal-mechanical coupling (Figure 2.14b). For larger grain sizes, we expect the thermal conductivity to remain constant irrespective of grain size or mechanical strain. To perform this investigation, we electrically annealed the freestanding specimens in-situ inside a transmission electron microscope (TEM) by passing current through the specimen. Figure 2.15a and 2.15b show two specimen with average grain size of 10 nm and 250 nm, respectively. Figure 2.15c shows the measured thermal conductivity (consistent value of 20

W/m-K) as function of grain size that was increased by electrical annealing. We then performed mechanical straining for these grain sizes (50, 120 and 250 nm). We did not observe any mechanical strain dependence of thermal conductivity in these specimens, which supports our hypothesis that the thermo-mechanical coupling is absent for grain sizes more than the electron mean free path.

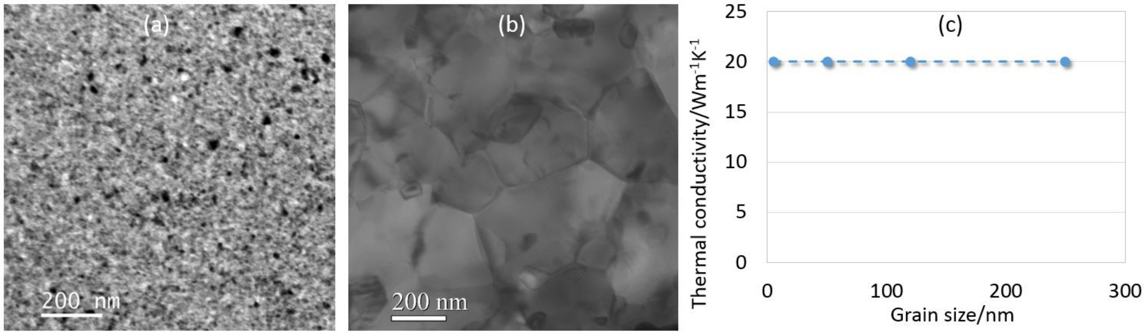

Figure 2.15. TEM bright field image of (a) as-deposited specimen and (b) specimen after grain growth with an average grain size of 250 nm; (c) Plot of thermal conductivity as function of grain size [106].

2.3.4 Conclusion

In this study, we measured thermal conductivity of 100 nm thick Zr films as a function of externally applied mechanical strain. The average grain size of the specimen is about 10 nm. The results show a decrease trend of thermal conductivity with increasing strain. We propose that the increasing scattering of thermal conduction electrons is due to the deformation localization at the grain boundaries which enhances the motion of grain boundaries (or results in increased defect concentration), thus pronouncing scattering of electrons. This hypothesis is further verified by the measurement of thermal conductivity as a function of grain size, which shows a constant value of 20W/m-K at average grain size ranging from 10 nm to 250 nm. The experimental results indicate the validity of our hypothesis that mechanical strain-thermal conductivity coupling is primarily size induced and is absent when the characteristic length-scale (thickness or grain size) is greater than the electron mean free path.

Chapter 3

Thermal Effects

Contents of this chapter are based on the following journal articles:

- **Baoming Wang** & Aman Haque, "In Situ Microstructural Control and Mechanical Testing Inside the Transmission Electron Microscope at Elevated Temperatures", *JOM*, Volume 67, Issue 8 , pp 1713-1720, 2015

  Author of this dissertation designed the experiment, performed the thin film and device preparation, experimentation, data analysis and manuscript writing. Aman Haque took part in experiment design, data analysis and manuscript writing.

- Tarek Alam, **Baoming Wang**, Raghu Pulavarthy, M. A Haque, Christopher Muratore, Nicholas Glavin, Ajit K Roy, Andrey A Voevodin, "Domain engineering of physical vapor deposited two-dimensional materials", *Applied Physics Letters*, 105, 213110, 2014

  Experiment design: M T Alam, Baoming Wang, Raghu Pulavarthy and Aman Haque

  Thin film preparation: Chris Muratore, N. Glavin, A. Roy and A Voevodin

  Device fabrication and sample integration: M T Alam, Baoming Wang and Raghu Pulavarthy

  Experiment and measurement: M T Alam and Baoming Wang

  Data Analysis and Manuscript preparation: M T Alam, Baoming Wang, Raghu Pulavarthy, Chris Muratore and Aman Haque

3.1 Mechanical Behavior of Aluminum Thin Film at Elevated Temperature

This study is motivated by the observation that there are other impactful areas open for contribution, such as in-situ TEM tests at elevated temperatures. Mechanical properties of thin films are known to exhibit strong size dependence at the nanoscale, where the dominant mechanism for deformation switches from dislocations to diffusion based processes. Since diffusion is directly related to external temperature and internal defect structures (voids, grain boundaries), nanoscale materials are known to exhibit pronounced temperature effect [110, 111]. Commercially available high temperature holders can help visualize the effect of temperature on the grain boundary kinetics [112, 113] but without measuring the mechanical properties. Conversely, quantitative testings setups are not TEM compatible [114, 115]. To date, we are unaware of any quantitative in-situ TEM testing on nanoscale thin films at elevated temperatures. A TEM-compatible high temperature setup would therefore augment the current capabilities in the areas of thermo-mechanical fracture, fatigue and creep.

3.1.1 Experimental Design and Setup

To measure the mechanical properties at elevated temperatures, we integrated the specimens with microscale heaters to apply specific temperature boundary conditions. Force is applied to the specimen with thermal actuators. The actuator design is optimized to achieve the desired loading at maximum actuator temperatures below 100 ºC. In addition, arrays of heat sinks are available to prevent heat flow from the actuator to the specimen. This is validated with infrared microscope. The freestanding specimen is essentially suspended from nanofabricated silicon structures (force sensing beams, heaters) whose stiffness are calibrated after the experiment is over. There are two reference gaps in the silicon structure that supports the two ends of the specimen.

Upon actuation of the device, one of these directly reads the elongation in the specimen while the other reads the displacement of the force sensing structures. Inside the TEM, these gap lengths are monitored through very high resolution, so that for the eleongation and force on the specimen can be monitored. Such manual data recording can be avoided by fabricating capacitive displacement sensors. The specimens in this study were co-fabricated with the actuators, sensor, heaters and electrodes, which ensures lithographically accurate specimen aligning and automatic specimen gripping. The nanofabrication processing sequence is similar to that described previously [60]. All the specimens in this study were 5 microns wide and 100 microns long, defined by a photo-lithographic mask after they were deposited on the a silicon-on-insulator substrate. The specimen thickness was nominally 100 nm with surface roughness of about 0.4nm (closely following the silicon substrate roughness) and a variation less than 5%. This thickness makes them electron transparent, which is necessary for the insitu TEM experiments. The gauge length parts were made freestanding by etching away the silicon substrate using SF_6 gas.

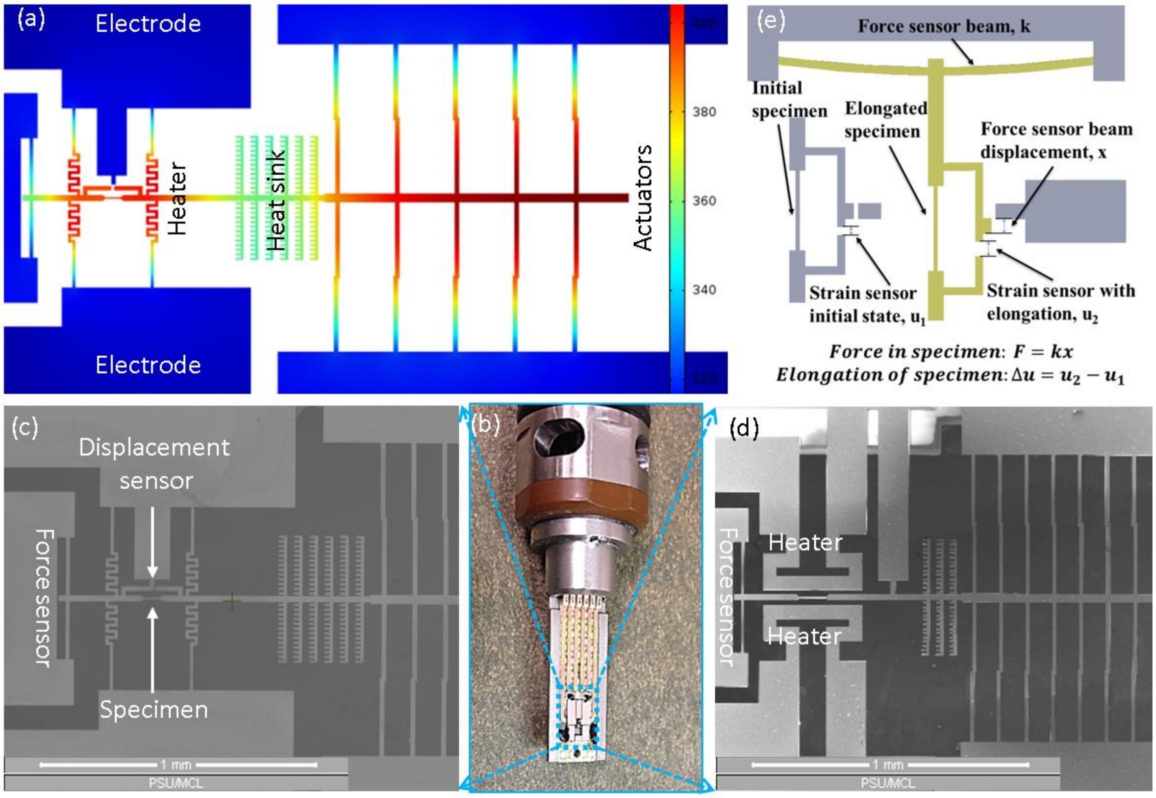
(a)
Electrode
Heater
Heat sink
Actuators
Electrode
400
380
360
340
320
(e)
Force sensor beam, k
Initial specimen
Elongated specimen
Force sensor beam displacement, x
Strain sensor initial state, u_1
Strain sensor with elongation, u_2
Force in specimen: $F = kx$
Elongation of specimen: $\Delta u = u_2 - u_1$
(c)
Displacement sensor
Force sensor
Specimen
1 mm
PSU/MCL
(b)
(d)
Heater
Force sensor
Heater
1 mm
PSU/MCL

Figure 3.1. (a) Finite element simulation of the MEMS device, (b) the experimental setup showing an electrical biasing holder and the MEMS chip (c) micro-heaters at specimen ends to generate temperature gradient if desired (d) micro-heaters at specimen sides to generate uniform temperature field, (e) schematic view of specimen elongation and force measurement [116].

Figure 3.1a shows the finite element simulation of the micro-electro-mechanical system (MEMS) chip, showing both the actuator and heater turned on. Figure 3.1b shows the experimental setup consisting of the chip on a commercially available electrical biasing holder. Figures 3.1c and 3.1d show two variants of the heater design to achieve both gradient (useful for simultaneous measurement of thermal conductivity) and uniform temperature field in the specimen. For electrical interrogation, such as four point probing, the silicon structures for heating can also be used as electrodes since the typical current and voltage are order of magnitude lower than heating. The specimen elongation and force measurement scheme is also pictorially described in Figure 3.1e. The mechanical calibration (such as stiffness of the force sensing beams) is performed with widely accepted force and displacement measurement tools such as the nanoindenter. The temperature calibration is perfomed with infrared microscope. Figure 3.2 shows the infrared images of the heaters and the calibration of a finite element model to determine the temperature as a function of supplied current. The maximum temperature we have achieved is over 950 K, which is very close to the melting point of aluminum. This is also shown in Figure 3.2.

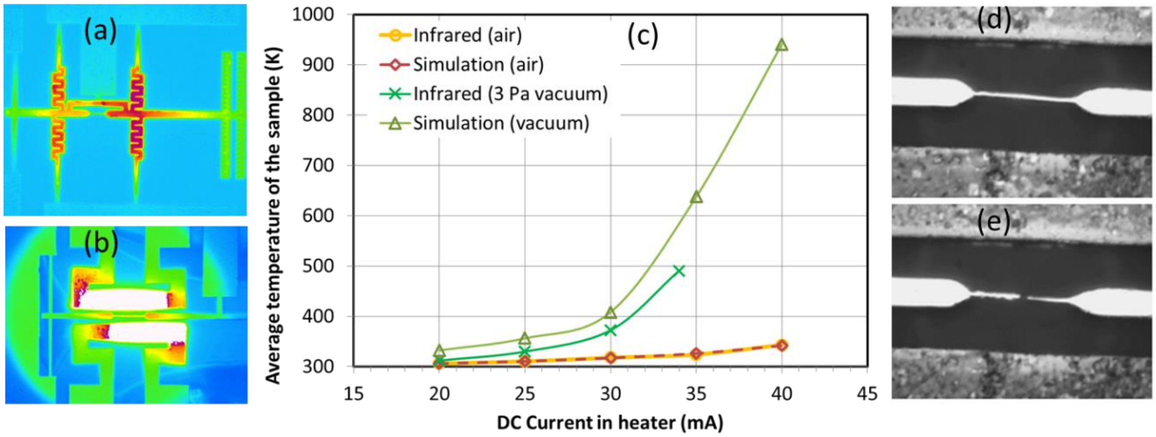

Figure 3.2. Temperature calibration with infrared microscopy of the (a) end heated and (b) side heated samples, (c) comparison with finite element simulation (d, e) demonstration of aluminum melting (around 925 K).

3.1.2 Experimental Results and Discussion

The objective of this study is to demonstrate the MEMS approach to extend current in-situ TEM mechanical testing to that at elevated temperatures. In this study, we performed uniaxial tensile testing on 100 nm thick freestanding aluminum specimens around 600 K, which is homologous temperature of 0.65 (melting temperatures of aluminum is 930 K). For comparison, we also present room temperature stress-strain diagram in Figure 3.3a. Because of the very small grain size (about 30 nm, Figure 3.3b) is not able to accommodate dislocation density similar to the bulk scale, the room temperature behavior is almost linear elastic, with yielding around 600 MPa. For the same reason, the fracture strain of 1.43% is also very small. Figure 3.3c shows the uniaxial stress-strain diagram a specimen taken from the same batch of prepared specimens. The Young's modulus is measured about 50% of the room temperature value. The higher volume fraction of grain boundaries can be ascribed to this observation since the inherent disorder on the grain boundary atoms means they are more sensitive to the temperature. Freestanding nanocrystalline thin films show higher sensitivity to elevated temperatures compared to bulk [111]. Figure 3.3d shows the TEM image of the specimen at homologous temperature of 0.65, 85 MPa stress and 0.18% strain (marked with a diamond in Figure 3.3c). Very little grain growth is seen, most likely because no time was allowed for the grain boundary kinetics. The maximum stress sustained by the sample (123 MPa) is also very small compared to 836 MPa for the room temperature, primarily because of the excessive diffusion at the high temperature due to scaling effects in nanocrystalline materials. Beyond the elastic limit, we observe dramatic softening, primarily because of the avalanche of diffusion dominated deformation at the grain boundaries at higher stress and temperature. This is because diffusion is an Arrhenius process with exponential, cubic and linear dependence on temperature, grain size and applied stress respectively. In general, diffusional creep tends to occur at a significant rate when the homologous temperature is 0.4 or higher. Figure 3.3e shows the specimen microstructure at homologous temperature of 0.65, 3.5 MPa stress and 4.4% strain (marked with an asterisk Figure 3.3c) to develop insight on the avalanche softening. Here, the grains do not grow in size; rather, the grain boundaries (shown by the white line like contrasts) became extremely mobile and appear to be unzipped compared to the solid-solid interface appearance (Figure 3.3b) at ambient conditions. The specimen also becomes structurally unstable as some part of it goes out of focus.

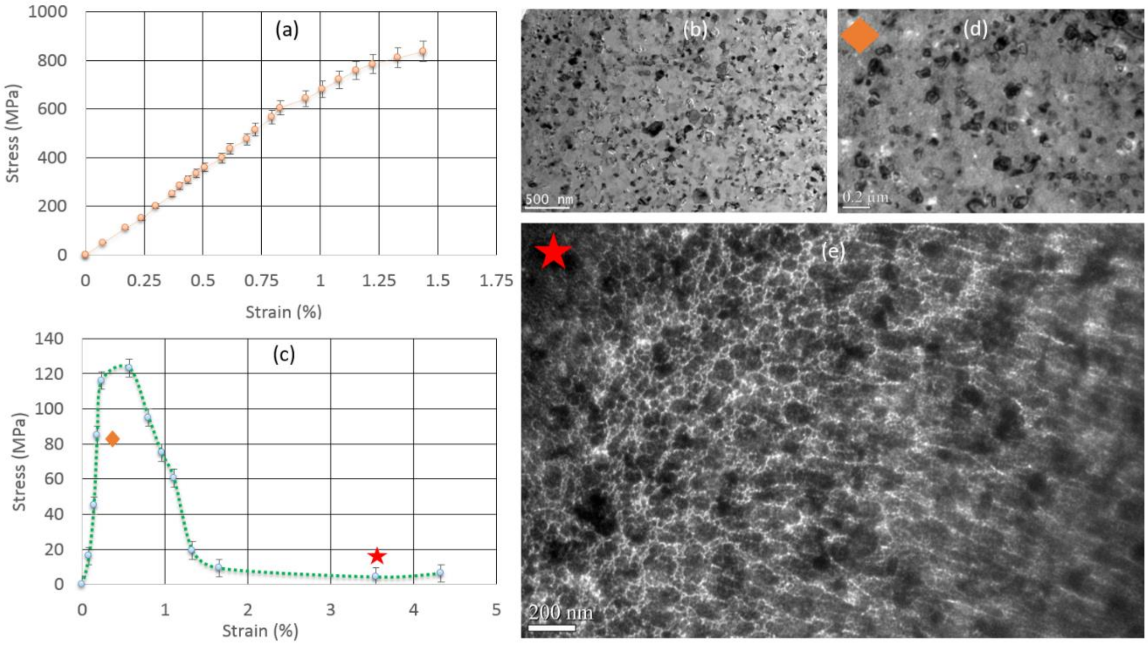

Figure 3.3. (a) Uniaxial tensile stress-strain response of 100 nm thick freestanding aluminum at room temperature, (b) TEM image of the specimen at room temperature and (c) stress-strain response at homologous temperature of 0.65, (d) TEM image of the high temperature specimen at 85 MPa stress and 0.18% strain, (e) TEM image of the high temperature specimen at 3.5 MPa stress and 4.4% strain [116].

3.1.3 Conclusion

TEM has been a workhorse for the materials and life sciences community. Through advances such as aberration correction, nano-beam diffraction and improved energy loss of filtering techniques, it has improved in resolution and analytical capabilities. However, the unique chamber design makes it less friendly to in-situ quantitative measurements. While heating and electrical biasing capabilities have been around a long time, these tools have been used mainly for microstructural or post mortem investigation. Inspired by the prospect of seeing while measuring, significant efforts have been exerted in the literature towards mechanical measurements. The increasing number of studies on in-situ TEM mechanical measurements reflects this. However, most of these measurements are performed under ambient conditions and as-received microstructure. In this study, we address this opportunity by developing MEMS-based multi-functional chips that can measure properties at elevated temperatures.

3.2 Domain Engineering of Physical Vapor Deposited Two-Dimensional Materials

Physical vapor deposited two-dimensional (2D) materials span larger areas compared to exfoliated flakes, but suffer from very small grain or domain sizes. In this letter, we fabricate freestanding molybdenum disulfide (MoS_2) and amorphous boron nitride (BN) specimens to expose both surfaces. We performed *in situ* heating in a transmission electron microscope (TEM) to observe the domain restructuring in real time. The freestanding MoS_2 specimens showed up to 100x increase in domain size, while the amorphous BN transformed in to polycrystalline hexagonal BN (h-BN) at temperatures around 600 °C much lower than the 850-1000 °C range cited in the literature.

3.2.1 Introduction

The rise of graphene [117] has galvanized the research on low dimensional materials that, to date, has extended to semiconducting transition metal di-chalcogenides (MoS_2 or WS_2), and insulating h-BN. This special class of materials consist of atomic layers with strong in-plane covalent bonding that are stacked together, with each layer bound by weak van der Waals bonding. The technological know-how from graphene has translated to other materials in 2D form and their intriguing layer/thickness dependence of thermo-physical properties as well as novel phenomena such as spin, valley or strain-tronics have led to the current resurgence of interest. For example the indirect bandgap of bulk MoS_2 (1.29 eV) shifts to direct type for a monolayer at 1.8eV [118]. This gives rise to unprecedented interaction with light [119] that can be exploited in opto-electronic devices. Monolayers of MoS_2 in transistors show on/off ratios many orders of magnitude larger than the best graphene transistors at room temperature, with comparable mobility [120] and are aggressively pursued for electronic and optoelectronic devices [121, 122]. A perfect foil for the semi-metal graphene is h-BN, also known as the *white graphene*, where atomically thick layers comprised of equal parts boron and nitrogen atoms form a 2D honeycomb structure iso-structural to graphite yet exhibiting very wide band gap of 5.9 eV nearing an insulator and a very high in-plane thermal conductivity [123] around 390 $Wm^{-1}K^{-1}$. Their low energy atomically smooth surfaces are free of dangling bonds as well as surface optical phonon modes, reducing phonon scattering from the dielectric. While these individual 2D materials are potentially interesting on their own, the exciting prospect of their stacking into heterostructures (or van der Waals' solids [124]) that currently propels 2D materials research. These are complex 'on-demand designer materials' with controlled stacks of individual molecular or atomic layers building novel 3D materials with interesting structural, electronic, optical, mechanical and other properties [125-127].

The most influential microstructural parameter for 2D materials physics is the grain or domain boundaries, which reflect degree of laterally coherent atomic ordering within the material. Mechanical exfoliation of bulk crystals allows maintenance of a high degree of atomic-scale order in the transition from bulk to 2D when compared to vapor phase synthesis, but only over areas below 100 μm^2. As a result, exfoliated crystals make excellent specimens for fundamental research but are impractical for scaling up technological applications. Therefore, alternate techniques for large area growth using processes amenable to microelectronics, such as chemical or physical vapor deposition, have seen a major thrust in the literature. In this time, none of the large area synthesis processes has been able to produce exfoliation-grade results, primarily due to the domain boundaries. Chemical vapor deposition (CVD) of MoS_2, for example, results in triangular domains with size scale of few tens of microns. The growth of these domains is sensitive to the precursor gas concentration and chamber pressure, while the nucleation rate dependence on extrinsic process parameters is yet to be understood and controlled. High surface energy features [128], such as scratches, edges, as well as special precursor treatment [129] have been used to increase the nucleation site density. As a result, even though the individual triangles are highly crystalline, they physically overlap upon extended growth and form domain boundaries [130]. The presence of these overlaps critically influences the overall microstructure, which is obvious from the remarkable difference seen in the Raman spectra as a function of the number of monolayers [131]. The physical overlap of these crystallites increases nonlinearly with the number of layers; therefore, even though the individual domains can be large, the effective domain sizes are much smaller. Physical vapor deposition (PVD) does not suffer from the isolated nucleation sites as CVD for continuous coverage, but in this case the crystallites are smaller. Hence the domain sizes are even smaller although the films demonstrate continuous coverage. Other large area synthesis processes, such as solution based dip-coating and thermolysis [132] are also limited by such domain boundaries.

We first highlight that atomic ordering of CVD, PVD or solution based process is typically localized in individual domains or crystallites. Over larger areas, these isolated regions of highly-ordered atoms are interrupted by domain boundaries, which generally degrades the properties of 2D materials [128, 129, 133, 134]. Low temperature (200-300 °C) annealing is routinely done in the literature to eliminate surface contaminations or to improve the electrode contacts, for bulk and thin film materials but there is very little evidence of increased domain size of 2D materials, via post-process annealing. However, it was shown recently that a combination of localized and global heating results in in-situ annealing of high angle grain boundaries in chemical vapor deposited graphene [135]. While high temperature annealing is expected to induce such recrystallization of the grain boundaries, the required temperatures are too high for MoS_2 [132] and BN [136]. MoS_2 for example has been extensively used as high temperature (>700 ^{o}C) solid lubricant (in vacuum), while h-BN, which is less sensitive to the composition of the ambient environment, does not show substantial phase transformation (amorphous to crystalline) or grain size increase unless the temperature and pressure are very high (>1000 °C and 7.7 GPa) [137, 138]. Evidence in the literature for microstructural changes in h-BN thin films involve special catalysts [139] or lattice matched substrates [140], such as ruthenium, with temperature exceeding 850 °C in either cases. In air, annealing of MoS_2 results in layer thinning [141], but most often complete oxidation at temperatures as low as 330 ^{o}C [142] Sulfur desorption is sometimes observed at high temperatures under high vacuum [143]. Grain sizes of MoS_2 films do not increase beyond 10 nm [144] even after annealing at 750 °C based on x-ray diffraction peaks peak sharpening methods of the structure analysis. However, we also note that 2D materials are expected to be extremely sensitive to external stimuli, particularly because of the predominance of surface atoms which are also expected to have a higher mobility In this study, we expose both surfaces of the specimens by releasing them from the substrate. Our hypothesis is that doubling the number of highly mobile surface atoms (not to mention high energy features such as surface steps and ledges) will reduce the activation energy of atomic migration for domain reconstructions driven by a reduction of domain boundary energy. To test this hypothesis, we selected thicker (40 layer) MoS_2 and (10 layer) amorphous BN specimens. Thicker specimens are more robust for the pick-and-place technique for transferring films to devices used here, and also facilitate characterization for definitive evidence of structural effects. Moreover, it is anticipated that the recrystallization temperature increases with the specimen length-scale and hence thicker specimens pose a rigorous test of the proposed hypothesis. In this study, we adopt an *in-situ* TEM approach that is known to be effective in detecting precise changes in crystallinity through both imaging and electron diffraction modes [145].

3.2.2 Sample Preparation and Experimental Setup

To examine the effects of heating of freestanding films, nanocrystalline MoS_2 (domain size around 5 nm) and amorphous BN films were integrated into a micro-electro-mechanical system (MEMS) fitted with micro-heaters for *in situ* heating inside TEM. PVD techniques were used for growth of both materials on silicon substrates coated with 200 nm thick spin on glass. Briefly, the sputtering process involves generation of a magnetically confined, cold, low pressure argon plasma adjacent to a pure MoS_2 disk. The disk also serves as the plasma cathode, driving positively charged argon ions into the disk, and liberating atoms from its surface. Those atoms condense on the substrate surface, where their kinetic energy and the substrate temperature dictate the resulting film microstructure. Asymmetric, bipolar voltage pulses were applied to the sputtering magnetron to control microstructure for surface plane (002) orientation [146]. BN films were deposited by pulsed laser deposition, where a focused laser beam pulse causes both ionized and neutral components from a BN target to accelerate to the desired substrate surface as a plasma plume in a nitrogen gas background. The deposition characteristics are controlled by laser wavelength, power, pulse rate, pulse duration, target-to-substrate working distance and relative orientation, background gas type and pressure, and substrate temperature. Previously, we have deposited few-layer MoS_2 and BN (mono to few-layers) on oxidized silicon substrates at temperatures as low as 350 °C and have performed complete characterization of the specimens [147, 148]. A 10 nm titanium layer was deposited in the same PVD growth chamber to protect the BN and MoS_2 specimen layers without breaking the vacuum. This is shown in Figure 3.4a, with inset elaborating the protective sandwich structure. In the next step, photolithography and reactive ion etching were used to pattern 10 micron wide and 100 micron long rectangular specimens that are released from the substrate. This step is shown in Figure 3.4b. These sandwich (oxide-specimen-titanium) structures were then mechanically cleaved at the supporting ends and then manipulated on the MEMS device. Figure

3.4c shows this step with the cleaved specimen and the nanomanipulator needle in a focused ion beam (FIB) chamber.

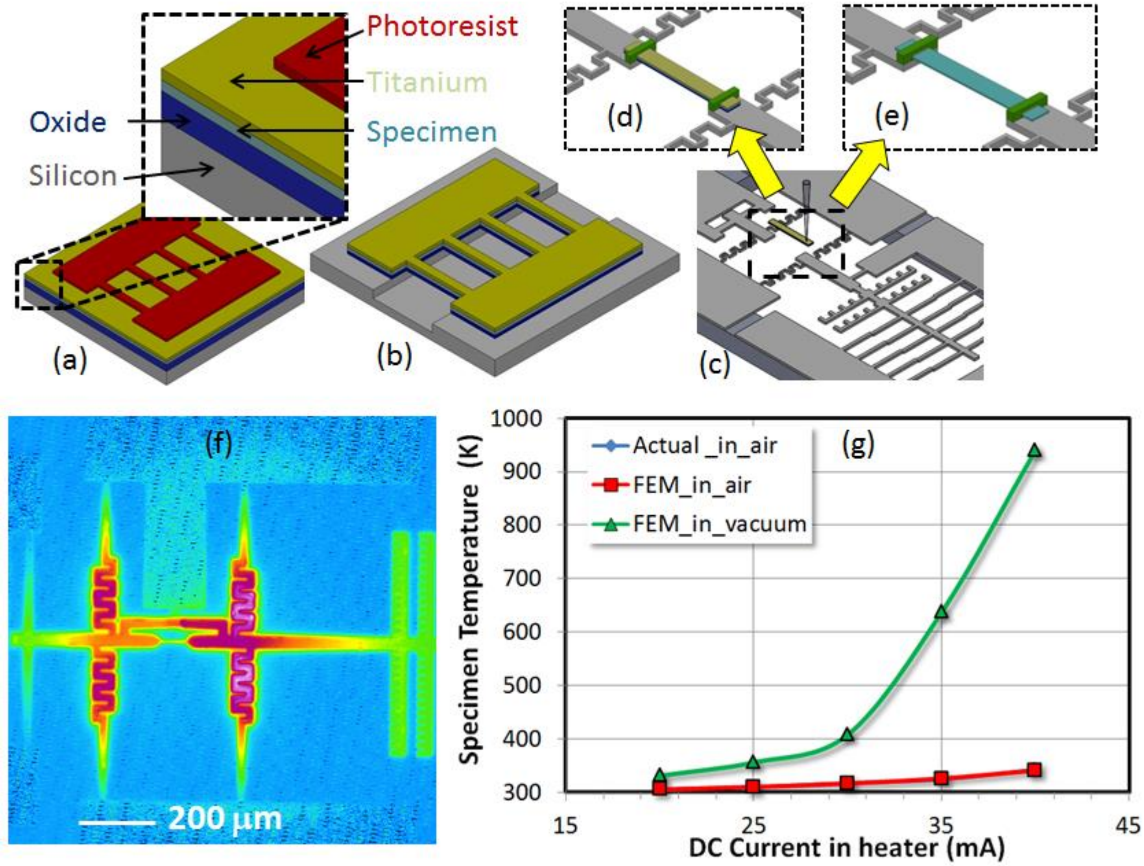
Photoresist
Titanium
Oxide
Specimen
Silicon
(a)
(b)
(c)
(d)
(e)
(f)
200 μm
(g)
Actual _in_air
FEM_in_air
FEM_in_vacuum
Specimen Temperature (K)
1000
900
800
700
600
500
400
300
15
25
35
45
DC Current in heater (mA)

Figure 3.4. Experimental details (a) PVD of specimen layers on oxide coated silicon wafer and a protective titanium over-layer (b) reactive ion etching of all the layers and additional isotropic etching of silicon after photolithographic patterning preparation (c) nano-manipulation of the a cleaved specimen on to a MEMS device and (d) securing it with carbon deposition (e) vapor phase hydro-fluoric acid etch to remove the protective titanium and oxide layers, (f) infrared image of the MEMS heaters and (g) experimental validation of a finite element model for heater temperature estimation in TEM [149].

Once the specimen is aligned with the MEMS device, it was secured with carbon deposition at the ends using a focused ion beam. The effective gage length of the specimen was about 10 microns. The MEMS device was then exposed to hydrofluoric acid vapor to remove the protective layers of spin on glass (SiO_2) and titanium without damaging the specimens. These two steps are shown in Figures 3.4d and 3.4e respectively. Energy filtered chemical element mapping confirmed removal of all traces of the Ti layer. No carbon was present either, suggesting that the specimen transfer technique is much cleaner than the conventional practice involving poly(methyl methacrylate) [150]. Figure 3.4f shows an infrared image of the heaters integrated with the test chip. A finite element model was developed to calculate the temperature profile for heating at ambient conditions. The excellent agreement between the measurement and calculation is obvious from the overlap of these two lines. Next, the convective mode heat transfer was turned off in the model to estimate the temperature profile inside the TEM chamber.

3.2.3 Results and Discussion

Figure 3.5 shows the experimental results on the MoS_2 specimen. In as-deposited form, the microstructure was turbo-stratic as evident from the diffused rings in the electron diffraction pattern. High resolution TEM indicated average domain size around 3-5 nm. The Raman spectra clearly showed the signature peaks for stoichiometric $MoS_{2,}$ but with reduced intensity indicative of phonon scattering over 5-10 nm domains. After annealing for 30 minutes at 600 °C minutes, significant domain restructuring was observed as the average domain size increased to approximately 100 nm. Figure 3.5d shows a high resolution TEM image where the lattice spacing of 0.61 nm clearly indicates crystalline phases of MoS_2, and the electron diffraction pattern shows spotty rings indicating grain growth. The effect of such low temperature and short time annealing is evident in Figure 3.5f, where the Raman spectra of the annealed sample is compared with the as-deposited as well as a bulk single crystal of MoS_2. The comparison with the bulk crystal is very promising and currently electrical measurements on the domain engineered specimens are underway.

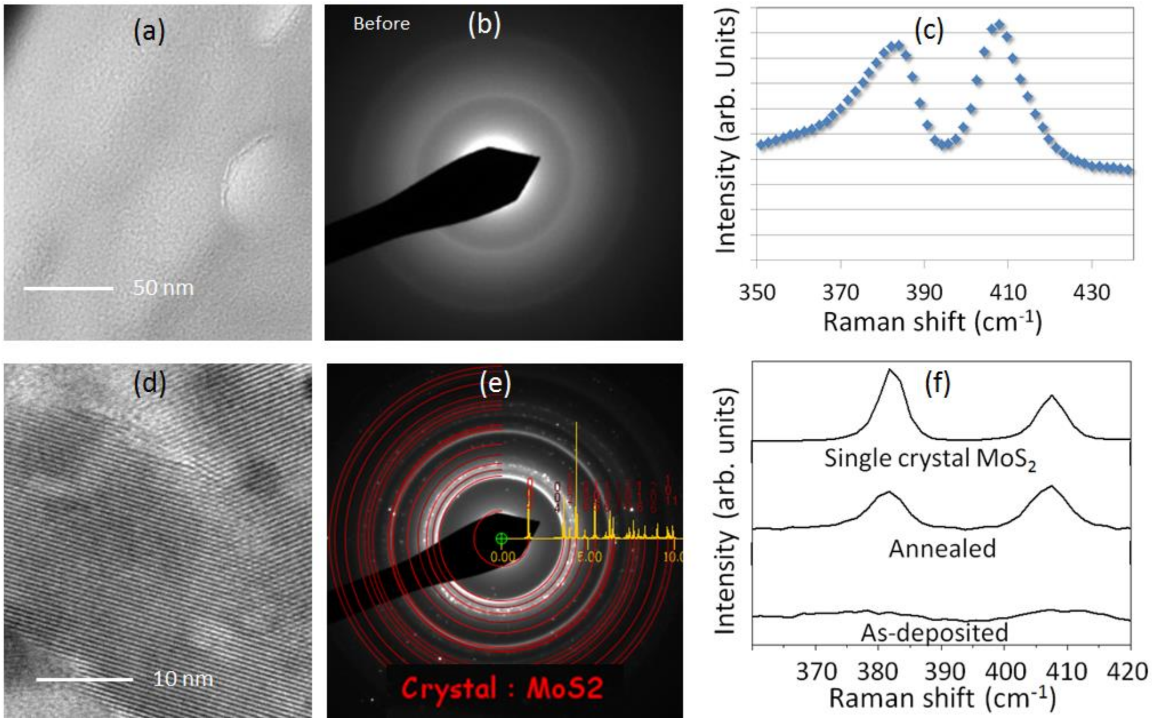

Figure 3.5. Experimental results on MoS_2 (a) bright field TEM, (b) electron diffraction and (c) Raman spectroscopy of the as-deposited specimen while supported on the substrate measured with 10 mW excitation laser power. After in-situ TEM annealing at 600 °C, (d) bright field TEM and (e) electron diffraction shows significant grain/domain growth, (f) comparison of the as-deposited and annealed Raman spectra with that for a single crystal MoS_2. The power was reduced to 1 mW to avoid damage to the free-standing specimens, thus the intensity of the as-deposited film is significantly reduced [149].

While turbo-stratic to nanocrystalline phase transformation at relatively lower temperature in MoS_2 is remarkable, it is not energetically forbidden as seen in literature for carbonaceous materials albeit at higher temperatures [151]. A rather challenging and long lasting problem lies in amorphous specimens that typically require impractical magnitudes of temperature and pressure [152]. Figure 3.6 shows the experimental results with *in-situ* TEM annealing of the amorphous BN films at 600 °C for 30 minutes. The as-deposited amorphous boron nitride transformed into crystallites with average domain size of 100 nm. Indexing of the resulting electron diffraction pattern reveals a match with that for hexagonal structure of boron nitride as shown in Figure 3.6d. The transformed structure was stable after the temperature was lowered to ambient.

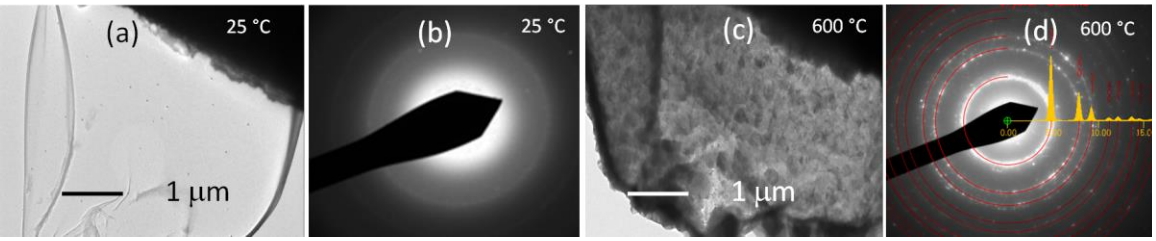

Figure 3.6. Experimental results for amorphous boron nitride (a) bright field TEM, (b) electron diffraction of the as-deposited specimen. After in-situ TEM annealing at 600 °C, (d) bright field TEM and (e) electron diffraction shows significant grain/domain growth with hexagonal crystal structure [149].

To explain the observed phenomenon of grain growth in MoS_2 and the amorphous to nano-crystalline phase transformation in BN at only 600 °C, we note the dominant role of surface diffusion. In general, surface is the fastest pathway for atomic migration, which can be orders of magnitude higher than bulk and grain boundary diffusion [153]. Since the specimens in this study were freestanding, both surfaces provide a reduced activation energy for diffusion compared to specimens on substrates where the grain boundaries are essentially pinned or constrained by the substrate and even extremely high temperature is not effective in their migration towards grain growth. An extension of the present study under progress is quantification of the activation energy for grain or domain boundaries by measuring the grain sizes as function of temperature and time, carrying out the experiments for various thicknesses. The implications of our finding are two-fold: i) provides an avenue for a large area synthesis of 2D materials by PVD methods with post-annealing and; ii) experimental guidance to the concept of domain size engineering while using free surfaces to significantly reduce temperature requirements for structure restructuring activation.

3.2.4 Conclusion

Successful implementation of domain engineering may allow us to grow these materials on any desired substrates and yet maintain acceptable crystallinity through post processing, relaxing the substrate constraint. However, domain size and grain-boundary defect engineering is mostly theoretical concept because studies on grain boundaries in 2D materials is still at its infancy [134]. By maximizing domain size and minimizing boundary defect concentrations, it may be possible to achieve pristine-like performance in large area 2D materials, which is a dominant technological barrier for integration of this class of materials in diverse applications.

Chapter 4

Synergistic Effects of Stress and Temperature

Contents of this chapter are based on the following journal articles:

- **Baoming Wang**, Tarek Alam and Aman Haque., "Grain Growth in Nano-crystalline Nickel Films at Low Temperature and Stress", Scripta Materialia, Volume 71, pp. 1-4, 2014.

  Author of this dissertation designed the experiment, performed the thin film and device preparation, experimentation, data analysis and manuscript writing. Tarek Alam assisted in experiment and data analysis and corresponding manuscript writing. Aman Haque took part in experiment design, data analysis and manuscript writing.

Influence of temperature and stress on grain growth was investigated in nano-crystalline nickel thin films *in-situ* inside a transmission electron microscope. Independently, temperature and stress did not show any appreciable effect. However, concurrent loading at only 20% of melting temperature and 20% of yield stress resulted in significant grain boundary mobility and grain growth. We propose that grain growth in nano-crystals is a stress-heterogeneity relieving mechanism that may not necessarily be associated with plasticity as proposed in the literature.

4.1 Introduction

Grain size is undoubtedly the most influential microstructural parameter governing polycrystalline materials properties. Mechanical properties have been studied for grain sizes from a few nanometers to hundreds of microns [154, 155]. By directly controlling defect density and grain boundary volume fraction, grain size is known to govern both elastic [93, 156] and plastic [157-159] behavior. It is generally accepted that as grain size becomes smaller, materials exhibit higher yield strength and lower ductility, primarily because of the confining of dislocations [1]. The trend reverses below a critical size due to large fraction of grain boundaries at the nanoscale [160]. Grain size effects go beyond mechanical behavior, since defects and grain boundaries are also responsible for scattering electrons and phonons. At the nanoscale, grain size can significantly impact electrical and thermal conductivity [161] primarily because grain boundary scattering is stronger than that by dislocations and vacancies [162]. The literature contains similar evidence for optical, magnetic etc. properties [163]. Such multi-disciplinary impact of grain size has been instrumental in vigorous research in various disciplines.

In this study, we focus on grain size growth in thin metal films, which are prevalently used in a wide variety of devices such as microelectronics, sensors, energy conversion [164], to name a few. Classical ways of increasing grain size are thermal annealing, precipitate/impurities and irradiation [165]. For nano-crystalline materials, thermal annealing works primarily through surface diffusion, a reason why grain growth stagnates at temperatures far below the melting point (0.2-0.3 T_m) [166, 167]. Here, the excess free volume associated with the grain boundaries are transformed in to vacancies as the grains grow. The atomic rearrangement in the grain boundaries decreases the grain-boundary mobility to effectively halt the grain growth. Increasing temperature decrease the activation energy barrier only temporarily since any atomic rearrangement lowers the grain boundary energy and slows down its mobility [167, 168]. A more recent study suggests that in addition to grain boundary energy reduction complex interaction of the anisotropy of grain boundary energy, grain boundary grooving and solute/triple junction drag may contribute to stagnation in grain growth [169]. Stagnation is therefore a key impediment to grain growth in nano-crystalline films.

Externally applied stress can also act as a stimulus for grain growth in nano-crystalline materials that are both pure and [170, 171] and alloyed [172, 173]. Typically, growth is viewed as a grain boundary mediated plastic deformation mode [160, 174, 175]. The phenomenon has been consistently observed at or near room temperature [170, 172, 176-178], which is very intriguing because grain boundary mobility requires higher temperatures. Also diffusional flow does not necessarily imply grain growth. It is suggested that room temperature grain growth is associated with shear stress driven grain boundary migration [176]. The concept is borrowed from recent studies showing shear stress can initiate normal grain boundary migration [179] at high angle boundaries and is energetically more favorable than the pure migration of a grain boundary [180]. When such coupled migration occurs over numerous grains, the global effect is an increased average grain size.

4.2 Experimental Setup

In thus paper, we present experimental evidence of grain growth due to simultaneous action of low stress and low temperature. This is in stark contrast with the grain growth literature, which involves either high stresses and low temperatures or low stress and high temperatures [170, 181]. Since both temperature and stress play role in grain growth; intuitively, external stress applied in nano-crystalline materials could catalyze the temperature driven grain growth and vice versa. However, there is no concerted effort in the literature to investigate such synergy, if any. This motivates us to develop an experimental setup where independently controlled uniform stress and temperature could be applied to a freestanding nano-crystalline thin film in-situ inside a transmission electron microscope (TEM). The advantages of merging high resolution of the TEM with quantitative in-situ characterization have been demonstrated previously to study the dynamics of grain boundary motion [172, 173].

Figure 4.1a shows a custom designed and fabricated micro-electro-mechanical system (MEMS) device with electro-thermal actuator and heater to apply uniaxial tensile stress and temperature on the specimen respectively. The 100 nm thick, 99.99% pure Ni films used in this study were first evaporated on a silicon-on-insulator wafer. Standard photo-lithography and deep reactive ion etching was performed on the wafer so that the actuator and heater structures are co-fabricated with the specimen. Such co-fabrication ensures perfect specimen alignment and gripping [93]. The electro-thermal actuator and heater were calibrated for various values of input current using an infrared microscope with 0.1°K resolution. After calibration, the 3mm x 5mm MEMS devices are mounted on an electrical biasing TEM specimen holder so that the experiments could be performed in-situ in TEM.

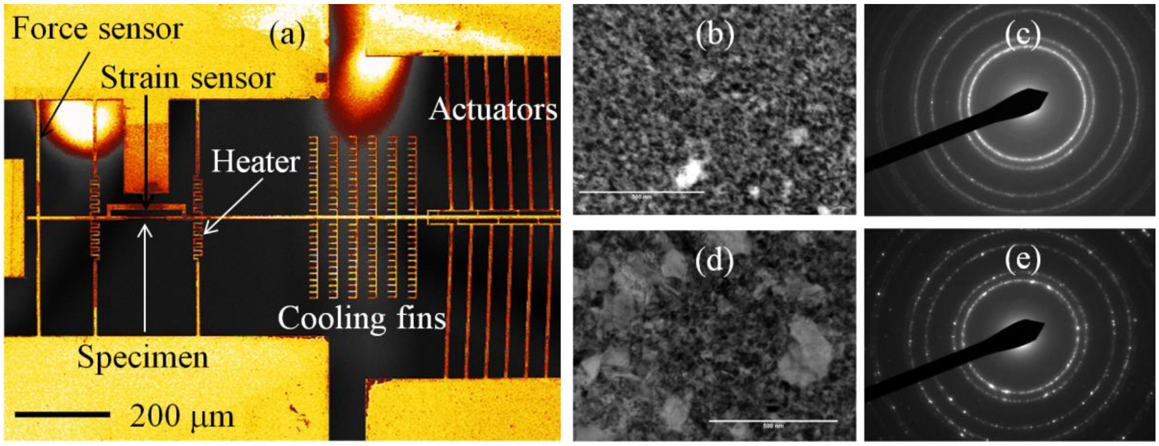

Figure 4.1. (a) Scanning electron micrograph showing various components of a MEMS device for quantitative in-situ TEM testing of thin films (false colored), (b, c) Bright-field and selected area electron diffraction pattern of the as-deposited nano-crystalline Ni specimen (d, e) room temperature grain growth in a span of 30 to 60 days. Scale bar represents 500 nm [182].

4.3 Results and Discussion

In-situ TEM tensile tests on the 100 nm thick freestanding nickel thin films measured Young's modulus and yield stress about 120±5 GPa and 1.8±0.1 GPa respectively, which compares very well with the literature [183]. The as-deposited grain size was approximately 10 nm with a few grains as large as 50 nm. Figures 4.1b and 4.1c show the bright field TEM and selected area diffraction images respective. Figure 4.1d shows secondary grain growth to a bimodal distribution (first mode 25 nm and second mode 100 nm) at room temperature without any applied stress in 30 to 60 days. Grain growth is also evident from the distinct changes electron diffraction pattern (Figure 4.1e). Such growth has previously been reported on nano-crystalline Pd and Cu, but not on Ni [167, 171]. The grain growth stagnated at this point. In a set of in-situ TEM heating (no applied stress) experiments, the specimen temperature was raised to 373°K (about $0.2T_m$) for several hours. This is shown in Figure 4.2a and 4.2b. No appreciable grain growth or grain boundary mobility was observed, which is expected because Ni is thermally stable below 473°K. In a separate set of experiments, room temperature mechanical loading was performed to investigate any stress-assisted grain growth. The results around ultimate stress range (1.7 GPa) are shown in Figure 4.2c and 4.2d, where discernible grain growth is observed in a few hours.

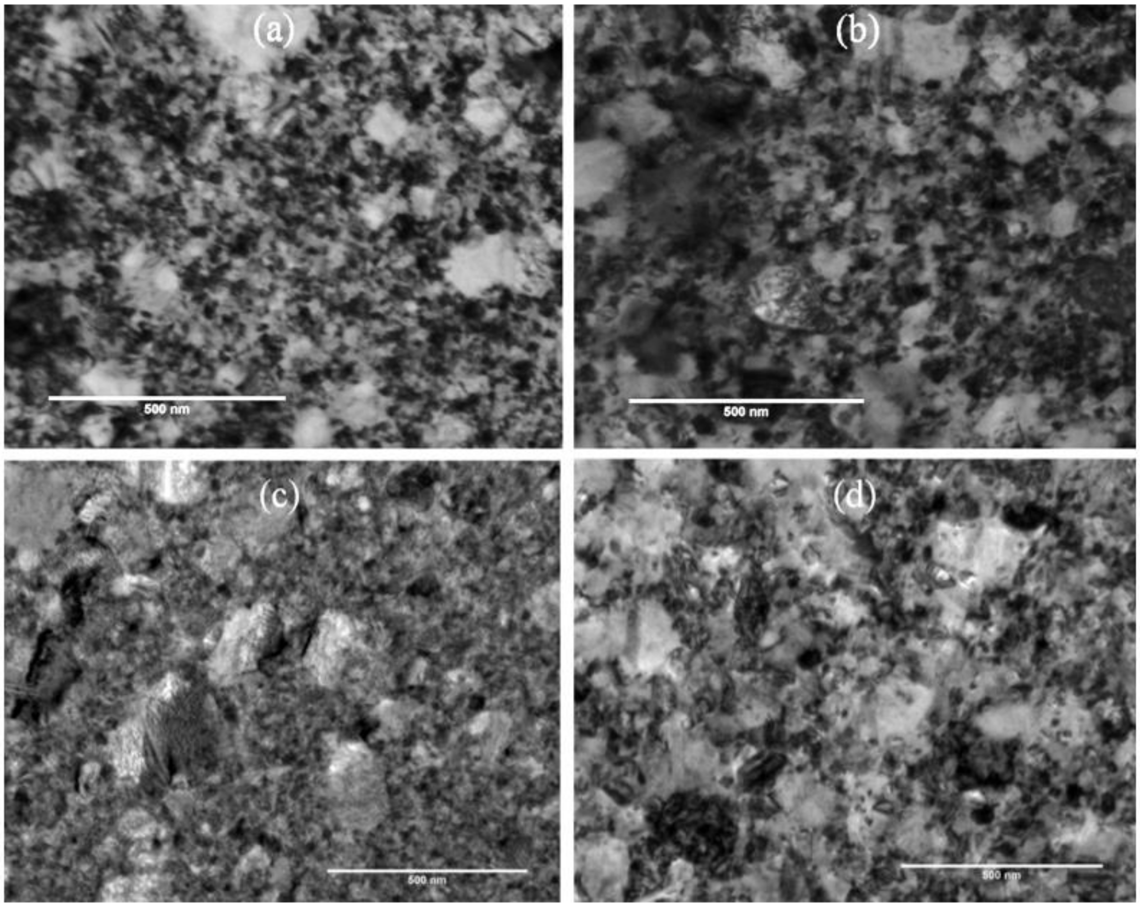

Figure 4.2. TEM images of the specimens at (a) room temperature (b) 0.2 T_m with no applied stress, (c) no applied stress and (b) 1.7 GPa stress at room temperature. Scale bar is 500 nm.

The third set of experiments comprised of applying stresses on heated (373°K or 0.2 T_m for Ni) specimens. The experimental results are given in Figure 4.3, where clearly discernible grain growth started at about 325 MPa stress, which is only about 20% of the yield stress (σ_Y). The growth rate at this low temperature-low stress loading configuration was rapid enough to be visualized in the quasi-statically (on the order of minutes) captured images, which suggests that further growth might have occurred had longer time been allowed. Interestingly, majority of the growth was in normal (or uniform) mode, where the smaller grains grew appreciably with the larger ones. Figure 4.3b shows further grain growth at 0.5σ_Y, resulting in equi-axed grain structure with many grains larger than the thickness. This uniform growth pattern is just opposite to the non-uniform growth as seen in individual temperature and stress loading and as predicted in the literature [184]. Interestingly, the relative magnitude of grain growth decreased with increased stress in the plastic deformation zone, where the in-situ TEM observations clearly show other modes (primarily grain rotation and dislocation) of plastic deformation. This is quite expected since according to the literature normal grain growth saturates once a columnar grain structure develops [184]. Also, for grain sizes larger than 100 nm, conventional plasticity is energetically more favorable than grain growth [185]. To the best of our knowledge, this is the first experimental evidence in the literature on large grain growth at low temperature-low stress loading.

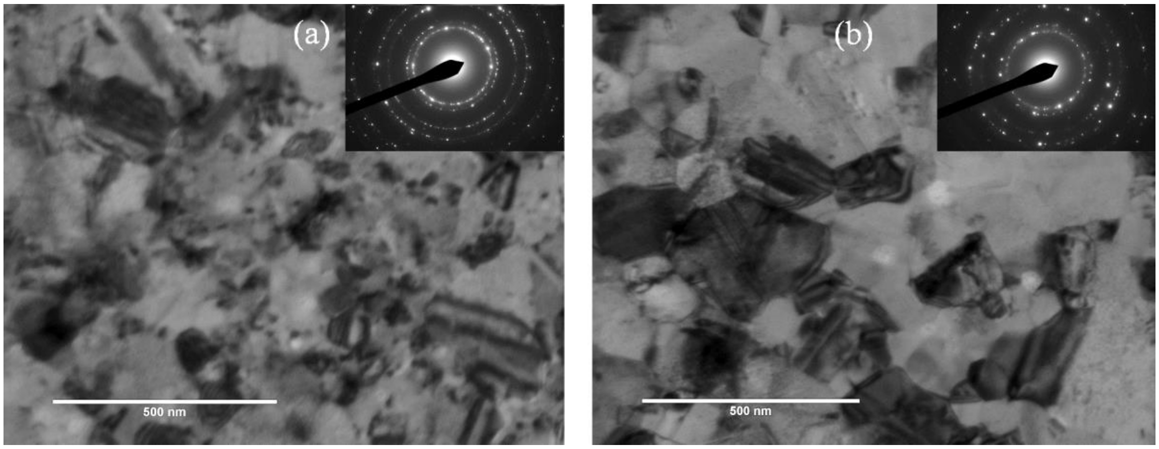

Figure 4.3. TEM and selected area diffraction images of a specimen loaded at (a) $0.2T_m$, $0.2\sigma_Y$ and (b) $0.2T_m$, $0.5\sigma_Y$.

For alloyed or less pure materials, low temperature or low stress mobility of grain boundaries has been reported in the literature [172, 173]. The interesting features of this study are therefore (i) weak stress-assisted growth at stresses close to failure and (ii) prominent growth at the combination of low stress and low temperature, and such for a pure metal. The lack of similarity between the observed grain growth under simultaneous and independent stimuli indicate that none of the individual proposed mechanisms (temperature or stress assisted) are directly applicable for the present study. Since the magnitude of stress required for stress-assisted grain growth varies from material to material (a comprehensive list compiled by [171]), a better metric is the stress value normalized with yield stress. In this respect, we clearly observe that almost all the observations reported in the literature are made near or at plastic deformation region. This includes our recent study on nano-crystalline Pt, where the far field stress of 290 MPa actually resulted in yielding at the notch tip where grain growth was observed [48]. Therefore, the concept of grain growth as a plastic deformation mechanism seems to be well suited for the existing literature. Contrarily, in absence of temperature, we observed very little grain growth even around failure stresses. Clearly, the effects of temperature and stress on grain growth are not additive or complementary in nature. Considering temperature alone, the magnitude of grain growth and the stagnation agrees with the literature, but it is difficult to ascribe the large and rapid grain growth at stresses below the yield point. This is because once stagnated, higher temperature (about $0.4T_m$) is needed to re-initiate grain growth. This is a very large thermal energy value compared to the strain energy supplied through the external stress in this study [186].

4.4 Conclusion

Our observation of stress and temperature driven grain growth agrees with a very recent proposition that grain growth is a deformation-induced thermally activated process [171]. The difference is that we observe the growth at as low as $0.2\ \sigma_Y$, which suggests that grain growth is not necessarily associated with plastic deformation. It is known that grain boundaries in nano-crystalline Ni are mostly high angle type, except abnormally large grains [157]. We propose that externally applied stresses are first localized in these boundaries and triple points [187] and then resolved into shear stresses that promote normal migration of the boundary [188], a process that is facilitated by even low temperatures. This hypothesis is difficult to prove beyond reasonable doubt because it is not possible to measure the local stresses at the high angle grain boundaries or triple points. To impose a quantitative argument, we refer to a computational investigation on nanocrystalline Ni, where Von-Mises stress of up to 8 GPa is seen to be developed at the triple junctions [189]. Assisted by the temperature, such high stresses can be resolved as shear stresses, thereby giving rise to large grain boundary motion. This is supported by our observation of grain growth at $0.2T_m$ and 0.2 σ_Y, where smaller grains grew significantly more than the larger grains. The motivation for such growth is more geometric compatibility (to reduce stress concentration at the high angle boundaries and triple points) than plasticity, a reason the phenomenon is observed below the yield stress of the specimens.

Chapter 5

Electrical (Current Density or Field) Effects

Contents of this chapter are based on the following journal articles:

- **Baoming Wang**, D.E. Wolfe, M. Terrones, M.A. Haque, S. Ganguly, A.K. Roy, "Electro-graphitization and exfoliation of graphene on carbon nanofibers", Carbon, Volume 117, Pages 201-207, 2017

  Author of this dissertation designed the experiment, performed the sample and device preparation, experimentation, data analysis and manuscript writing. Aman Haque took part in experiment design, data analysis and manuscript writing. S. Ganguly, A.K. Roy synthesized the specimen and involved in manuscript writing. D.E. Wolfe and M. Terrones took part in data analysis and discussion and manuscript preparation.

- **Baoming Wang**, Tun Wang, Aman Haque, Michael Snure, Eric Heller, and Nicholas Glavin, "In-situ TEM Study of Domain Switching in GaN Thin Films", Applied Physics Letters (Submitted)

  Author of this dissertation designed the experiment, performed the sample and device preparation, experimentation, data analysis and manuscript writing. Tun Wang participated the experimentation, data analysis and corresponding manuscript writing. Aman Haque took part in experiment design, data analysis and manuscript writing. Michael Snure, Eric Heller, and Nicholas Glavin synthesized the specimen and involved in discussion and manuscript writing.

5.1 Electro-graphitization and Exfoliation of Graphene on Carbon Nanofibers

We present electrical current assisted graphitization as an alternative to conventional high temperature annealing of carbon nanofibers. In-situ experiments were performed on individual vapor grown carbon nanofibers inside a transmission electron microscope to measure the changes in resistance as a function of current density while observing the microstructural changes in real time. About 1000 times decrease in resistivity was measured at current density below 10^6 ampere/cm^2. Further increase in current density leads to the uniform exfoliation of mostly bi-layer graphene flakes from the skin of the graphitic nanofibers, which leads to further reduction of the electrical resistance. The uniformity of the graphene flake growth over the nanofiber surface area achieved in this study is difficult to achieve with conventional approaches. Further experiments on networked nanofibers suggest that the graphene can remarkably reduce the electrical Kapitza resistance of the nanofiber junctions. The demonstrated processing of such hierarchical nanostructured fibers lead to high surface area and high conductivity carbon nanofibers that can impact flexible electrodes in electrochemical energy conversion or high specific strength composites applications.

5.1.1 Literature Review

Various allotropes of carbon in different length-scales have dominated the area of harsh environment electrodes, as in refractories and electro-chemical energy conversion applications [190]. Graphite electrodes are prevalently used in batteries and fuel cells, because they are the cheapest and fastest in charging-recharging efficiency. They are also highly conducting (resistivity ~10^{-5} ohm-cm) and inert at chemically harsh conditions. However, the graphitization process drives out the functional groups and defects, lowering the specific surface area. For electrode applications, the large surface area is critical for deposition and encapsulation of catalyst metals and metal oxides in high concentrations, which is necessary for specific energy [191]. Length-scale can play a major role since shrinking the fiber diameter from micrometers to nanometers enhances the surface area to volume ratio 100-1000 times as well as flexibility and strength [192]. The high aspect ratio (length to diameter ratio) enables the formation of conductive network at an extremely low percolation [193]. More importantly, unique structural and hierarchical design can be implemented in the nanofibers (fibers of diameters in nanometer scale) to enhance surface reactivity. Thus nanofibers can be more attractive than nanotubes because of the feasibility of creating various morphological features, like core/shell structure and hierarchical pores [194]. Nanofibers are also extremely compliant and relevant to flexible/wearable applications such as paper battery or supercapacitor [195]. These unique features have fueled extensive research in carbon nanofibers for applications beyond batteries, such as high specific strength materials [196, 197], water filtration and desalination, hydrogen storage, tissue scaffolding, bio-sensing, electromagnetic interference shielding, to name a few [198].

This study is motivated by two fundamental challenges in electrode applications of carbon nanofibers. These are, (i) graphitization of carbon nanofibers [199] and (ii) the mutual exclusiveness of electrical conductivity and specific surface area [200]. Complete graphitization requires extremely high temperature (> 2800 °C) treatment, making it energy or cost intensive. Currently, carbon nanofibers are manufactured by either catalytic (vapor grown) conversion or carbonization of polymeric precursors. The catalytic process [201] decomposes hydrocarbon gas over elemental transition metals at temperatures around 1100 ºC in a partial hydrogen atmosphere. Partially graphitized carbon nano fibers (CNF) with very good electrical properties (~10^{-2} Ω-cm) are obtained by decomposing the hydrocarbon on the metal surface, where the carbon dissolves and diffuses and finally precipitates in form of graphite at the other side of the metal particles. Another approach is electrospinning of polymeric fiber and then pyrolyze at high temperatures to improve electrical conductivity [194]. The microstructure is a function of the catalyst and precursor, as the literature has shown graphite platelets both perpendicular, parallel or stacked at an angle to the fiber axis [202]. Thermal graphitization significantly increases the crystallite width and thickness. In hollow core type CNF, Lee et. al has shown development of double layer with distinct discontinuity between the layers because of the graphene layer folding [199]. This finding is consistent with Endo et. al, who observed formation of graphene loops between adjacent graphene layers in both the outer and inner surfaces of the hollow core [203]. As a result, the CNF surfaces transform from a relatively to a rugged one, probably resulting from improved stacking within domains connected by loops having limited crystallite size, accompanied by structural reorganization between domains.

In this study, we propose two new approaches to address the above-mentioned challenges. Firstly, we suggest that electrical current induced graphitization has the potential to replace the existing high-temperature based graphitization technique. The hypothesis is that externally applied current density induces secondary thermal and mechanical fields and their overall effects at the nanoscale are synergistic (and not additive). The graphitization energy barrier is too high to achieve by the individual stimuli, such as mechanical stress, temperature or current alone [204]. Figure 5.1 schematically shows the proposed concept of ‘electro-graphitization’, which is motivated by evidence of graphitization under high voltage biasing [205, 206] and high energy electron irradiation [207]. Secondly, we propose a nanoscale hierarchical structure shown in Figure 5.1 to increase the specific surface area. Here, the surface of the carbon nanofibers is uniformly grafted with graphene (two-dimensional carbon with highest electrical conductivity and specific surface area) flakes. The relative uniformity of graphene is anticipated to be a result of ‘electrical exfoliation’ that comes naturally with the proposed graphitization process (no extra steps needed).

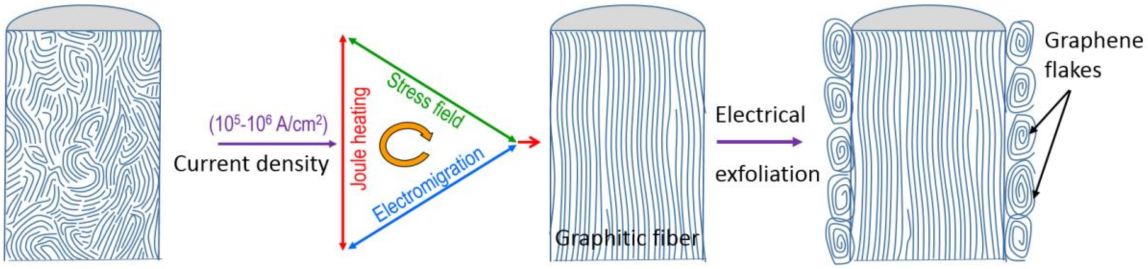

Figure 5.1. Proposed electrical current induced graphitization and subsequent surface exfoliation to create high conductivity graphitic nanofibers with high surface area graphene.

5.1.2 Experimental Setup

The core concept of this study is that electrical annealing (Joule heating accompanied by associated thermo-mechanical stresses) can be more effective in microstructural reconfiguration because the process essentially entails multi-domain (thermo-electro-mechanical) loading. To test the hypothesis, we developed an experimental setup to perform in-situ electro-graphitization tests inside an aberration-corrected transmission electron microscope (TEM, FEI Titan^3). The uniqueness of this setup is that we are able to measure electrical properties as function of annealing current density and observe the corresponding atomic structure in real time for unambiguous interpretation. The CNF specimens were received in clumped bulk powder form from The Applied Sciences, Inc. These were synthesized using chemical vapor growth process where primary feedstock methane is cracked at 1100 ºC in presence of air, NH_3, H_2S and $Fe(CO)_5$. The catalysts are iron particles originating from $Fe(CO)_5$, active by sulphur [201].

Figure 5.2 shows the proposed experimental setup with single fiber and single junction specimens. The vapor grown single fiber specimens were lifted off using a scanning electron microscope based nanomanipulator and positioned on a nanofabricated test chip. The test chips are fabricated from silicon on insulator wafers by patterning the gold-coated electrodes on the top side and then the backside of the wafer is etched through to allow freestanding specimens. After securing the specimens, we used electron beam induced carbon deposition to obtain electrical contacts. We also studied networked specimens made from thousands of such individual fibers.

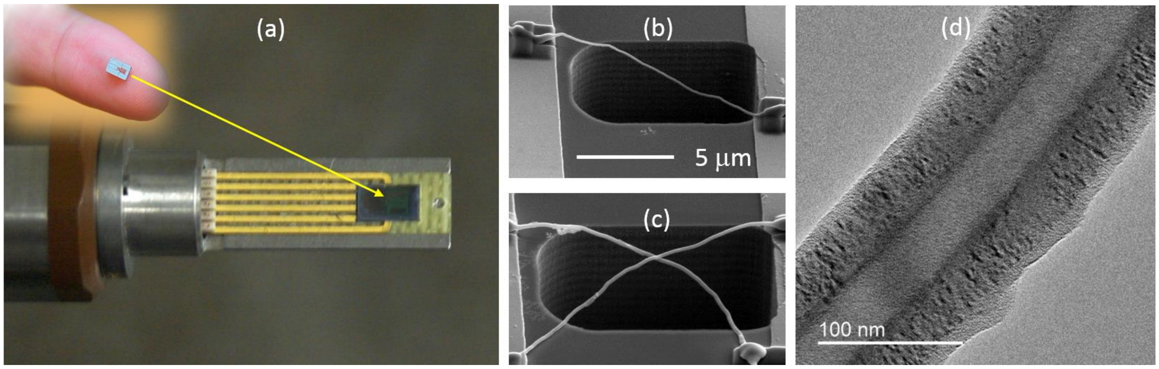

Figure 5.2. Experimental setup (a) nanofabricated chip with microelectrodes mounted on TEM specimen holder, SEM image of (b) single carbon nanofiber and (c) nanofiber-junction-nanofiber specimen, suspended on a micro fabricated through-the-wafer hole (d) zoomed TEM image of the carbon nanofiber.

In a typical experiment, a constant dc current was supplied to the specimen and the corresponding voltage drop was measured. Resistivity of the specimen and the current density were calculated using the fiber geometry. For each current value, the specimen microstructure was observed in both bright field and diffraction modes. It is important to note that the electro-graphitization process is very fast as compared to high temperature annealing as we allow only 15 minutes between the two current supply values. The experiments were continued until the breakdown of the specimens. Unlike the dielectric breakdown or metal electro-migration, carbon nanofiber breakdown is a complex mix of thermo-mechanical stress and the increasing brittleness during the graphitization process.

5.1.3 Experimental Results and Discussion

The first set of experiments in this study involved single fiber specimens to avoid multiple electrical contacts and thus accurately characterize the electrical current density and resistivity. Figure 5.3a shows a representative set of results along with TEM images of the microstructure at the initial, intermediate and final stages of graphitization. The as-received nanofibers were vapor grown at 1200 °C from metal catalysts and were only partially graphitized. The TEM images showed amorphous skin before the electro-graphitization. As the applied current density is increased, the microstructure became more graphitic. The resistivity of as-received specimen was $1.7\text{x}10^{-2}$ Ω-cm, which decreased by 3 orders of magnitude to $1.5\text{x}10^{-5}$ Ω-cm at applied current density of about $1.5\text{x}10^{6}$ A/cm^2. This value is very close to the bulk graphite resistivity, suggesting very high degree of graphitization achieved. This is confirmed by comparing the Raman spectra (Figure 5.3b) before and after the processing operation. The very sharp decrease in electrical resistivity might originate from following events:

(i) Detrapping of charge carriers due to the current stressing. Carriers are typically trapped by defects along the conductive graphitic layers of the carbon nanofibers at room temperature. In addition, some gaseous species adsorbed on the carbon nanofibers can also serve as carrier traps.

(ii) Amorphous to crystalline phase transformation leading to graphitization. This process is described in detail below.

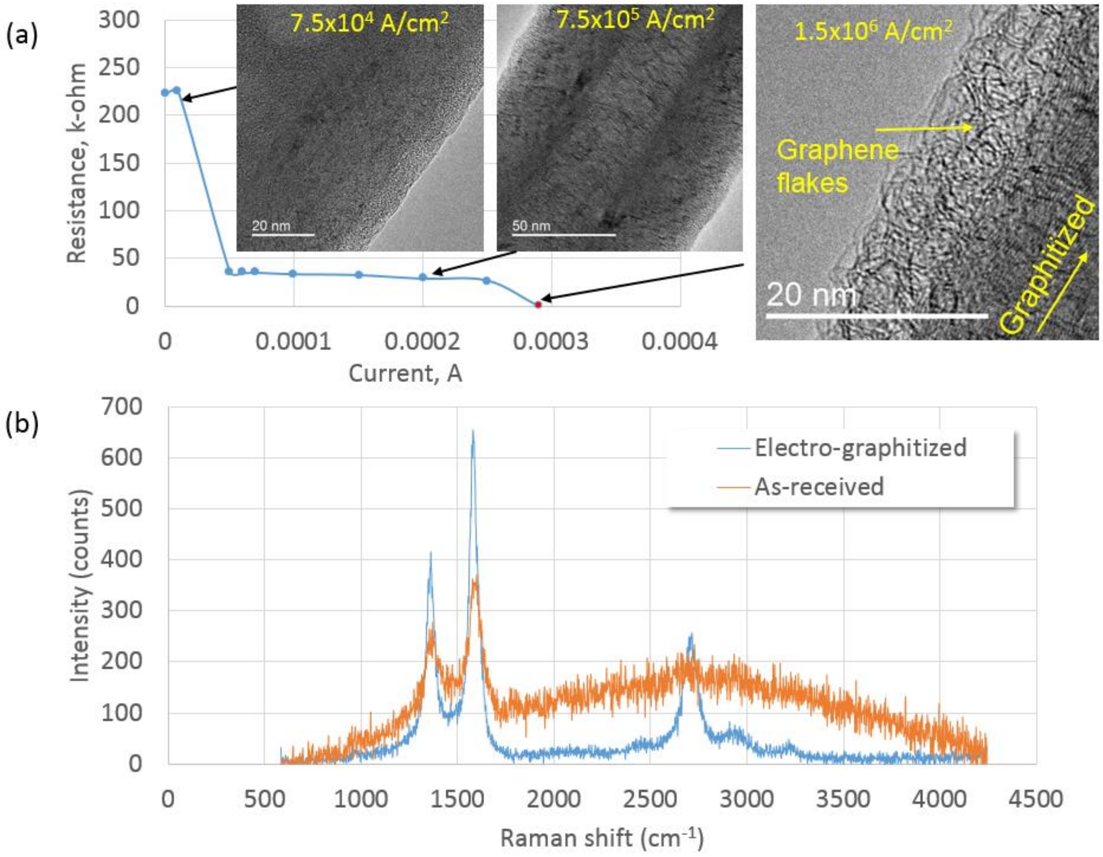

Figure 5.3. (a) Electrical resistance of single carbon nanofiber as function of electrical current. Bright field TEM images are labeled with values of applied current density. (b) Raman spectra of as-received and electro-graphitized carbon nanofiber specimen.

From a mechanistic perspective, graphitization is essentially atomic scale rearrangement while squeezing out disorders or defects from the nanofiber. This is possible only when the defects have enough mobility to exceed the activation barrier. Temperature can increase atomic mobility, but the process of annealing or defect annihilation is very slow, requiring few hours to days. Complete graphitization requires temperatures exceeding 2800 °C. In our case, moderate to high current density generates electron wind force that transfers the momentum in the atomic vacancies, which make them mobile. Such momentum transfer is proportional to the vacancy gradient. In other words, the process is intense only on the defects and is minimal in crystalline lattice, making it effective and energy efficient. It also creates temperature and thermo-mechanical stress fields, which further increases defect mobility. The process is similar to electromigration in metals, except the covalent bonding in carbon does not allow actual mass transport as in metals.

The uniqueness of this study is the synergy of these fields that induce graphitization at lower energy compared to high temperature annealing alone. This is evident from a different set of experiments described below. Figure 5.4a shows the exact same type of specimens in the previous figures, except we dispersed silver nanoparticles on the nanofiber surface. This was achieved with high-energy sputtering of ultrathin silver, which formed the sphere after dewetted by the CNF surface. At higher current densities, Joule heating melts the silver but the de-wetting on the carbon surface make them form very small spheroids. Figure 5.4a shows the spheroids, which coalesce into bigger ones (Figure 5.4b). At about $1x10^6$ A/cm^2 current density, the large spheroids start to evaporate. From the temperature-vapor pressure curve for silver, we estimate the nanofiber surface temperature be around 800 °C, considering the 10^{-7} Torr pressure inside the TEM chamber. This current density is also very close to the values at which graphitization took place in Figure 5.3. This temperature is almost one-fourth of that required for high temperature treatment alone. Figures 5.4d-5.4f show the electrical breakdown of the carbon nanofiber, which occurs at the middle of the specimen gauge section. This shows the fundamental difference between electromigration in metals, where metallic atoms are physically transported inside the material and failure by void formation occurs at the cathode (one end of the specimen).

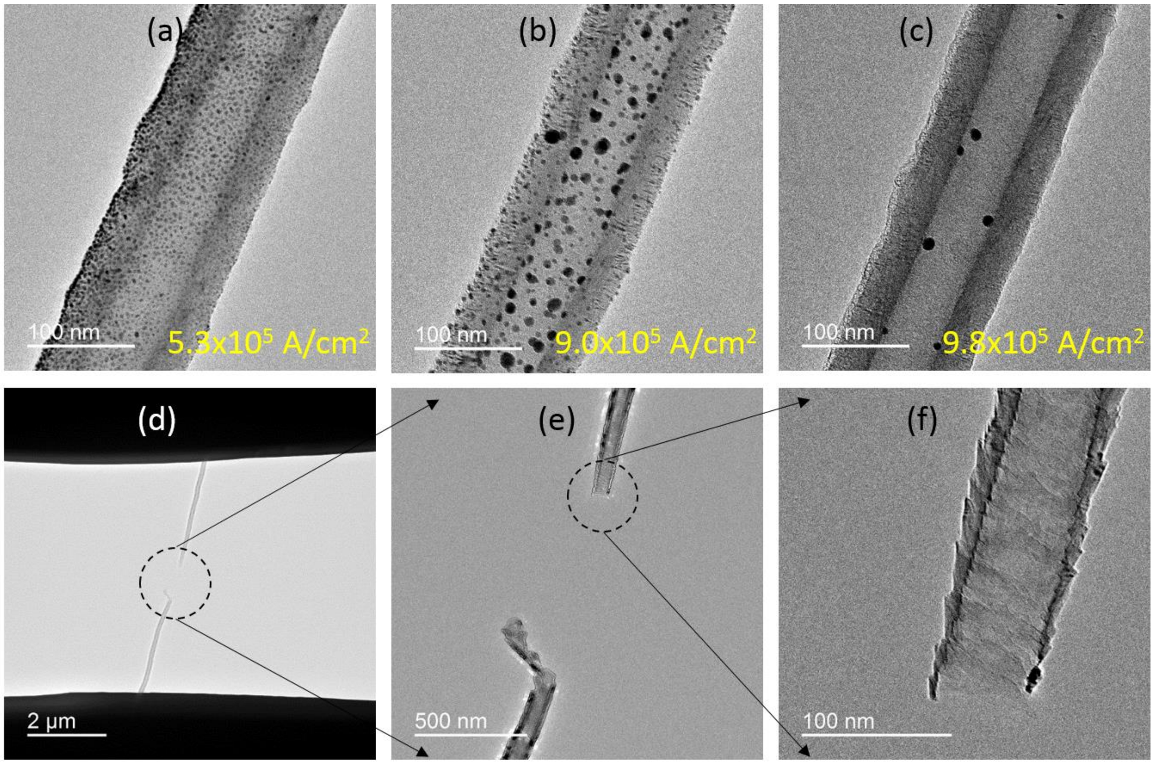

Figure 5.4. (a) Melting of silver on carbon nanofiber, which subsequently (b) coalesce and (c) evaporate inside the TEM chamber. (d-f) failure of the semiconducting nanofiber.

The synergy of temperature, current and stress fields is obvious from the four driving forces in the atomic flux balance equation [208]. These are (1) atomic or vacancy concentration gradients, (2) the electron wind force, (3) temperature gradients, and (4) mechanical stress gradients. Equation 1 shows these respective contributions to the total atomic flux, J_a [209].

$$J_1 = -D\nabla N; \quad J_2 = \frac{NeZ^*D\rho}{kT} j; \quad J_3 = -\frac{NDQ\rho}{kT^2}\nabla T; \quad J_4 = \frac{ND\Omega}{kT}\nabla\sigma \qquad (1)$$

Where, D is diffusivity, k is Boltzmann’s constant, T is absolute temperature, N is vacancy concentration, Z* is effective charge number, e is the elementary charge, j is current density, Q is the heat of transport, ρ is density, Ω is the atomic volume, and σ is the hydrostatic stress. Along the grain boundary, where the diffusion is fastest, we can re-write [210],

$$J_a = \frac{D_{gb}}{kT}\left(\frac{\partial \sigma_n}{\partial l} + \frac{Z^* e j \rho}{\Omega}\right) \qquad (2)$$

Since self-diffusion is an Arrhenius type function of temperature [211], any accompanying temperature field will exponentially promote the atomic flux. This is further promoted in the grain boundaries that have orders of magnitude higher diffusivity compared to grain interior. The implication for nanocrystalline carbon is thus even more pronounced atomic mobility. Mechanical stress field also has a synergistic effect on the electrical annealing process [212]. According to Equations 1 and 2, the vacancy flux decreases as soon as internal stresses build up in the metal due to vacancy transport from cathode end to anode end. The role of an external mechanical field is to counter the effects of the internal stress and the net effect will be higher vacancy flux and mobility [213]. Finally, the electro-graphitization process can be orders of magnitude faster than thermal annealing because of the very high atom drift velocity (V_a),

$$V_a = \left(\frac{D}{kT}\right)|e|Z^* j \rho \qquad (3)$$

In comparison, thermal annealing generates order of magnitude smaller vacancy concentration and thermal drift speed is negligible compared to electrical drift speed [214].

The difference between electro-graphitization and conventional high temperature graphitization can be explained by the fundamental processes involved with each processes. In the conventional process, very high temperature is used to have atomic and defect mobility. The combined effect is increase in the graphitic platelet size and decrease in defect concentration. However, as equations (1-3) suggest, the effect of electrical current is not just Joule heating, but beyond that. The electron wind momentum transfer specifically targets the defects; therefore, defect mobility is significantly higher in our process. The mechanical stress developed also catalyze the diffusion process. This is evident from the time scale (about 15 minutes) of our entire process. However, the most remarkable difference is that electro-graphitization results in exfoliation of the graphene layers. This is shown in Figure 5.5, where exfoliation of the graphitic layers takes place from the inner surface of the initially hollow fiber. Upon further increase in current density, similar exfoliation is seen at the outer surface. The initial and final conditions of the nanofiber are shown in Figures 5.5a and 5.5b respectively. The transformation of the nearly amorphous skin of the as-received specimen to uniform flakes is clearly visible from these two images. Figure 5.5c shows the exfoliation of the layers from inside surfaces of the nanofiber. Dense network of flakes appears to fill in the initially hollow core of the fiber, labeled as location B. At slightly higher current density, similar phenomenon is observed at the outer surface. This is shown in Figure 5.5d, labeled as location A.

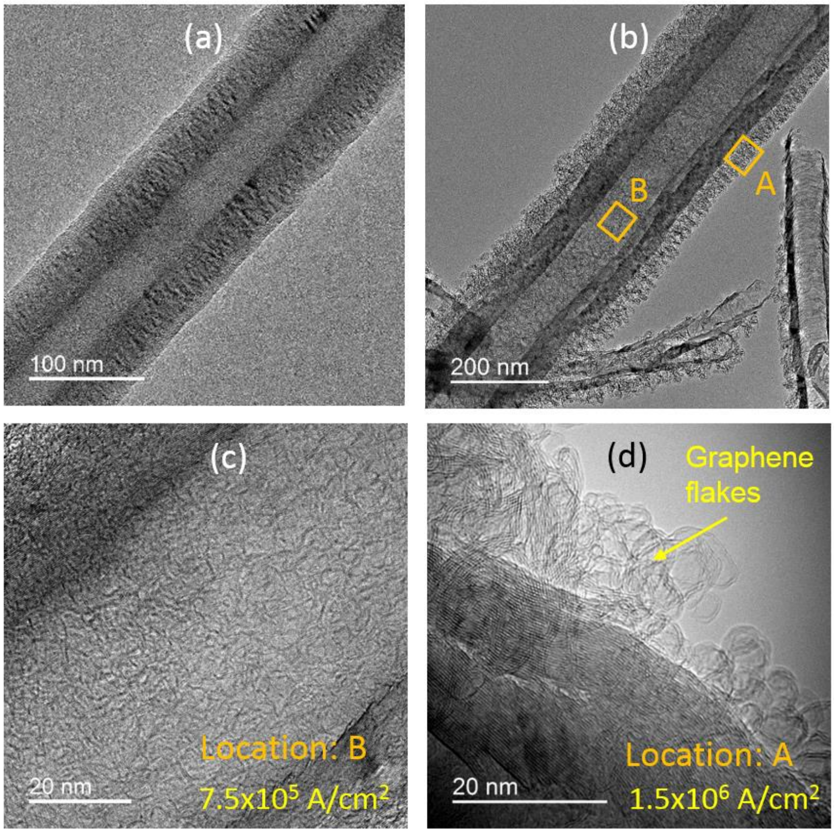

Figure 5.5. TEM images of the (a) as-received specimen and (b) after electro-graphitization and subsequent graphene exfoliation (c) zoomed view of location B and (d) location A showing exfoliated graphene on the carbon nanofiber surfaces.

It is important to note that the exfoliated flakes are mostly bi-layer graphene and not carbon nanotube growths on the nanofiber surface. The presence of graphene flakes is not very obvious in the Raman spectra (Figure 5.3b) because the laser penetrates the flakes and thus most of the spectra characteristic is due to the nanofiber itself. We therefore performed very high-resolution electron energy loss spectroscopy (EELS) inside the TEM, where it was possible to acquire spectra from the flakes and the graphitized nanofiber. This is shown in Figure 5.6. The remarkable difference between the spectra acquired at these two different regions clearly indicate that the flakes are more crystalline compared to the nanofiber. The flake spectra is very different from that for carbon nanotubes and very close to that for graphene. We note that the flakes are folded, therefore even after their high crystallinity; the spectra can never be as sharp as a graphene layer attached to a flat and rigid substrate.

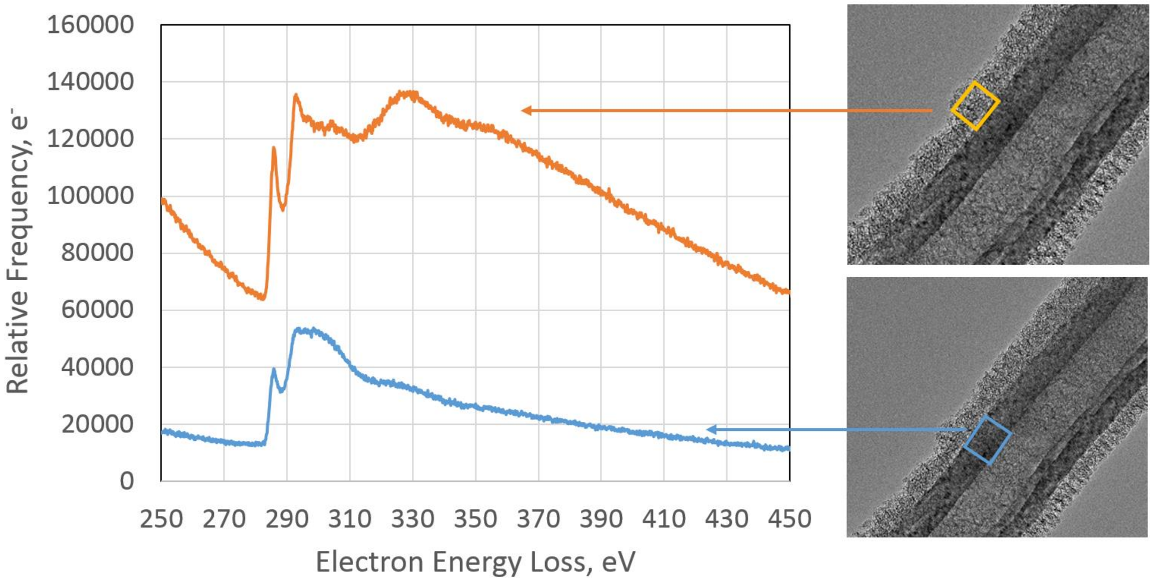

Figure 5.6. Electron energy loss spectra (EELS) obtained from (a) nanofiber shell and (b) exfoliated flakes at the surface.

An impactful aspect of this finding is the nanoscale hierarchical structure (uniformly grafted graphene flakes on carbon nanofiber), which allows us to have both high conductivity and specific surface area. This is achieved in our study naturally (no extra step required) as a part of our graphitization process. After the fiber is graphitized, further increase in temperature and current density will only increase the vibrational energy of the atomic layers. This is because the lattice is crystalline and the electrons rarely experience any momentum transfer. In the individual layers, atoms are bonded covalently, but bonding between layers is via weak van der Waals bonds. We propose that since graphite is a semimetal, the individual layers accumulate electrostatic charge at the fiber surface. This electro-static charge accumulation can lead to the exfoliation of the surface layers. Figure 5.7a shows the mechanism schematically. An indirect evidence for such electrical exfoliation is that it has never been seen under purely thermal heating in the literature. Figures 5.7b-5.7d show the evolution of the graphene flakes. Figures 5.7d and 5.7e show that the distance between two atomic layers is ~0.34 nm, which closely matches the inter-layer gap in graphite. This dimension is too small to be a single nanotube diameter [215]. Figure 5.7f shows further evidence of the graphene flakes that has no resemblance to carbon nanotubes. Prior studies have demonstrated such graphite to graphene conversion, albeit through different processes [216, 217].

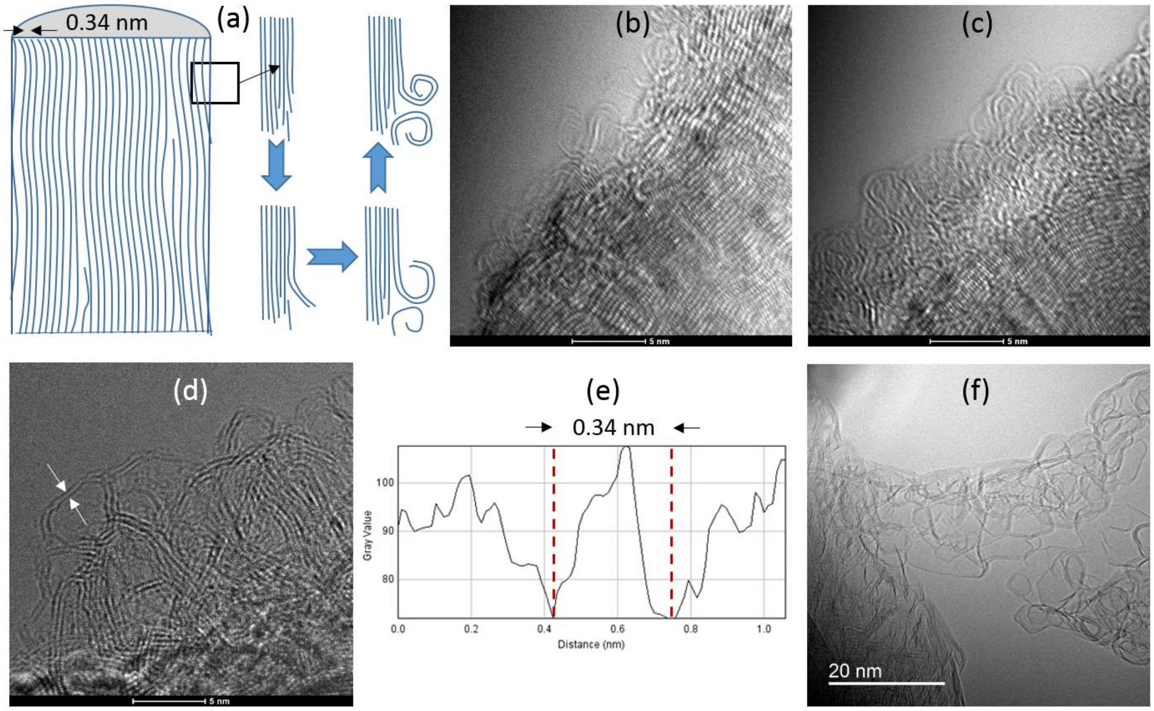

Figure 5.7. (a) Proposed electro-static charge based exfoliation mechanism for surface layers (b-d) TEM image showing evolution of the exfoliated structure, (e) gray scale mapping of the distance between two layers is 0.34 nm, indicating graphene and not nanotube formation (f) high magnification images of the graphene flakes.

An implication of the nanoscale hierarchical structure is the large surface area of graphene mitigating the electrical contact resistance in a network of fibers. In a realistic electrode application, millions of nanofibers would make contacts with each other. The Kaptiza or contact resistance is > 10 times higher than the individual fiber resistance [218, 219] and can be as high as 10 kΩ, because (i) the contact area is too small, thereby constricting the current flow and (ii) the surface of the carbon nanofibers may have amorphous skin. These concerns are shown in Figure 5.8, where two nanofibers are idealized as two cylinders making a point (zero area) contact.

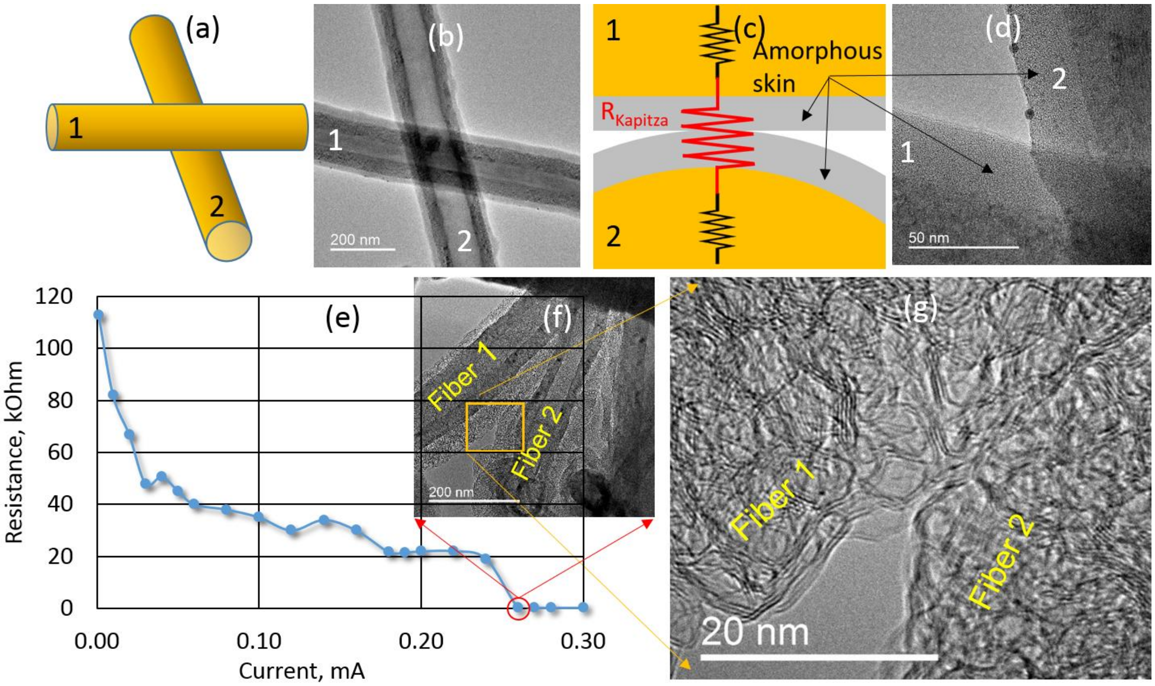

Figure 5.8. (a, b) Very small contact area and (c, d) poorly conducting amorphous skin result in large contact resistance in a carbon nanofiber network (e) electrical resistance of a fiber-contact-fiber configuration as function of electro-graphitization, (f) evolution of graphene flakes resulting in diminishing contact resistance, (g) high magnification TEM image of the graphene-graphene contact between two nanofibers.

To explore the role of surface graphene layers on the Kapitza resistance between two nanofibers, we prepared a single junction specimen similar to Figure 5.2c. Here the two electrodes are patterned on two different fibers, so that the electrical circuit contains the individual fibers and the contact or Kapitza resistance. Figure 5.8e shows the electrical resistance of this fiber 1 – contact – fiber 2 configuration as a function of the current passed through it. The decrease of the resistance is initially due to the nanofiber graphitization, which slows down asymptotically around 20 kΩ. We now compare Figure 5.8c with 8e to note the contributions coming from the two nanofibers and their junction. In our single fiber experiments, we found the electrical resistance after graphitization to be in the range of 50-100 Ω. The nanofiber contribution to the total resistance therefore cannot be more than 200 Ω. In other words, the junction of Kaptiza resistance contributes most of the total value (at least 19.8 KΩ). As shown in Figure 5.8e, the exfoliation of the graphene flakes sharply reduced the contact resistance, which can be explained by the zoomed view of the true contact area in Figure 5.8f. Here, graphene flakes are seen to make intimate contact over large area, similar to nanoscale Velcro. This contact area is orders of magnitude higher compared to Figure 5.8b. The specific surface area is difficult to measure for single electro-graphitized single CNF. However, it can deduced from Kapitza resistance, which is a direct measure of the surface area. In our experiments, the exfoliated graphene flakes replace the near amorphous skin of the as-received nanofibers in Figure 5.8d. These two factors reduce the Kaptiza resistance down by up to three orders of magnitude. The vendor measured specific surface area is 54 m^2/g. Our measured the Kaptiza resistance as low as 50-100 Ω, which is at least 50 times lower compared to the literature [218]. We can thus estimate the surface area to be around 2500 m2/g, for our graphene-grafted nanofibers.

While this study is focused on the fundamental mechanisms behind electrical current driven graphitization in a single CNF, future attempts are expected to develop a process compatible for bulk scales. In particular, we envision that CNF mats in form of thick films can be prepared and electro-graphitized. Future applications of such mats could be in composites that carry current or heat, or for electrodes in electro-chemical applications. CNFs offer opportunities by encapsulating these high capacity materials to obtain both high energy and power densities as well as long cyclic life. These strategies seem to double the specific capacity of carbon nanofiber based electrodes [220, 221]. Opportunities also exist as cathode applications since currently used Lithium metal oxides.

5.1.4 Conclusion

Low cost, high conductivity, excellent charge-recharge cycling and chemical resistance make graphite electrodes a popular choice in electrochemical energy conversion and storage. However, bulk graphite is not structurally compliant. Nanofibers offer unprecedented specific surface area and mechanical flexibility, but the fundamental challenge is the mutual exclusiveness of electrical conductivity and specific surface area. Conventional approach towards graphitization of carbon nanofiber requires very high temperatures (> 2800 °C). Even for completely graphitized nanofibers, the electrical contact resistance remains to be a challenge. The theoretically zero fiber to fiber contact area acts as a constriction for electron flow, which gives rise to very high electrical contact resistance. Prior attempts to address the electrical conductivity have involved mechanical mixing of carbon nanotubes or graphene. The results have not been convincing because of the poor dispersion of the mixture.

In this study, we demonstrated a novel concept of electro-graphitization that induces synergistic thermo-electro-mechanical fields to graphitize carbon nanofibers at around 800 ºC temperature and below 10^6 A/cm^2 current density to reduce nanofiber resistivity from 10^{-2} Ω-cm to 10^{-5} Ω-cm. This opens door to energy efficient, low temperature graphitization not possible otherwise. A unique aspect of the electro-graphitization is the naturally accompanying hierarchical nanofiber grafted with graphene structure. We show high resolution TEM, Raman and electrical measurements as evidence for uniform grafting of graphene that is obtained naturally (no extra step) during graphitization. This approach is fundamentally different from the current art of mechanical mixing, which suffer from agglomeration because it is nearly impossible to disperse graphene uniformly. The hierarchical nanostructure resolves a fundamental exclusiveness between surface area and electrical conductivity. This is because of the orders of magnitude increase of the graphene flakes surface area compared to that of the amorphous skin in as-received carbon nanofibers. Successful translation of the fundamental aspects of this study can potentially open applications of graphite that is currently not possible at the bulk scale. Examples are flexible or paper batteries, super capacitors, water filters and desalinators or smart textiles using graphene coated nanofibers as electrodes.

5.2 Domain Switching in GaN Thin Films

Microstructural response of gallium nitride (GaN) films, grown by metal-organic chemical vapor deposition, was studied as function of applied electrical field in-situ inside a transmission electron microscope. Sudden change in the electron diffraction pattern reflecting 90° domain switching was observed at a 20 V bias, applied perpendicular to the polarization direction. No such switching was observed for thicker films or for the field applied along the polarization direction. This anomalous behavior is explained by the nanoscale size effects on the piezoelectric coefficients of GaN, which can be 2-3 times larger than the bulk value. As a result, large amount of internal energy can be imparted in 100 nm thick films to induce domain switching at relatively lower voltages to induce such events at the bulk scale.

5.2.1 Introduction

Gallium nitride (GaN) is an attractive semiconductor with a bandgap of 3.4 eV, which remains direct and continuous from the visible to ultraviolet spectrum. This has spurred studies on short wavelength optoelectronic applications such as light-emitting diodes [222, 223] and detectors [224]. The compounded effects of high electron mobility and breakdown field have additionally led to development of GaN-based high power and high frequency electronic devices, such as radio-frequency or microwave power amplifiers [225]. Further attractive features, such as high chemical, mechanical and thermal stability as well as thermal conductivity, are instrumental in high power applications otherwise difficult with silicon microelectronics. Attributes such as lower on-resistance, higher speed, higher operating temperature allow reduced volume and weight in power electronics applications such as electric vehicles [226], aircrafts or integration of renewable energy into the electric grid [227].

The outstanding device functionality achieved by GaN-based devices must be matched with an understanding of the reliability during high electrical fields and powers. Accordingly, a large body of reliability studies, from device life testing to fundamental degradation mechanisms, are available in the literature. High electrical fields induce charge trapping and generation of deep levels or interface states leading to time dependent breakdown mechanisms. In the device, these effects manifest as threshold voltage shifts and gate-drain or drain-source catastrophic breakdown [228]. A major hypothesis is that the inverse piezo-electric effect (IPE) drives the strain in the barrier layer beyond a critical value, leading to mechanical degradation. These electrically active defects cause a sudden and non-reversible increase in the gate leakage current of several orders of magnitude [229]. Direct evidence of field-induced defect has been captured by Transmission Electron Microscopy (TEM) [230] and micro-Raman spectroscopy [231]. Electrons accelerated by the high electric field underneath the drain side of the gate of the device are known to degrade the device by de-passivating the hydrogen passivated defects within the GaN, which was studied through electroluminescence microscopy [232]. Surface potential of an operating device was mapped in real time to study steady-state and transient charge distribution due to point defects [233]. It is accepted that the degradation involves a complex thermo-electro-mechanical field [234, 235], characterization of which remains to be a challenging pursuit [236].

In this study, we adopt an in-situ TEM approach towards understanding the microstructural response of GaN towards applied electrical field. The attractive feature is that high-resolution imaging and diffraction patterns are obtained in real time as the electrical field is changed. In comparison, most breakdown or domain switching studies are ex-situ or post mortem in nature. Accordingly, we present in-situ TEM diffraction evidence of 90° domain switching under electrical field, which is yet to be reported in the literature for GaN. This is because GaN typically exhibits electrical breakdown before the domain switching. Domain switching is a unique property of piezoelectric materials, where unit cells changes their crystallographic orientation by aligning the polarization axis towards the field direction. It is a highly nonlinear and irreversible process that can originate from mechanical [237], electrical [238] and electromechanical [239] loading. *Hwang et al.* [240] treated the material as an agglomerate of randomly oriented grains, each with the ability to change its direction of polarization under an applied stress and/or electric field. The macroscopic properties a calculated from the volume average of the properties of each grain. The difference in Gibbs' energies has been proposed to be the driving force for polarization switching to derive a thermodynamics-based criterion [241]. Here, each grain is modeled as a mixture of distinct types of domains. *Chen et al* [242] formulated the domain switching conditions, the evolution of microstructures, the incremental mechanical and electrical relations by analyzing the coupled microscopic electroelastic fields and using the internal variable theory. More recently, *Wang et. al* [243] employed phase-field simulations and demonstrated the temporal evolution of the polarization switching, macroscopic polarization and strain changes under an electric field or a stress field. *Fotinich et al.* [244] used electric displacement along with stability arguments as a criterion of polarization switching under electromechanical loads.

There are two commonly used criteria for domain switching in piezoelectric materials. One of the criteria is based on work done, and the other is internal energy density switching criterion. The first criterion [240] suggests polarization switching when the electrical and mechanical work exceeds a critical value.

$$\sigma_{ij}\Delta\varepsilon_{ij} + E_i\Delta P_i \geq 2P^S E_C \tag{1}$$

where E_i is the electric field intensity, E_C is a coercive electric field, P^S is spontaneous polarization, $\Delta\varepsilon_{ij}$ and ΔP_i are the changes in the spontaneous strain and polarization during switching, respectively. A second criterion was proposed based on internal energy density after large discrepancy was observed between the theory and experiment on piezo and ferroelectric materials [245]. Here, domain switching takes place whenever the internal energy due to mechanical or electrical loading exceeds a critical value U_C. For example, 90° switching in the x_3x_1 plane, the internal energy density is [245]:

$$U_C = \frac{1}{2}(\sigma_{11}\varepsilon_{11} + \sigma_{33}\varepsilon_{33} + 2\sigma_{31}\varepsilon_{31} + D_1E_1) \tag{2}$$

Where D_1 = $D_1 = \varepsilon_{11}E_1$. Even though GaN has a wurtzite crystal structure lacking inversion symmetry along the c-axis, the literature does not have any prior evidence on domain switching in this material for electrical or mechanical stressing.

5.2.2 Materials and Methods

To study the microstructural changes in GaN as function of electrical stressing, we developed an in-situ TEM experimental setup. Here, the specimen is integrated with a microfabricated device that is custom designed with micro-electrodes, electro-thermal actuators and microheaters for various types of loading. Fabrication and operation details of this microdevice fab are given elsewhere [116]. The epitaxial GaN film was grown on a hBN/sapphire substrate by metal-organic vapor phase epitaxy (MOCVD). A 15 nm AlN nucleation layer was grown at 1000°C followed by a 2 µm GaN layer using a standard high temperature growth process [246]. Various studies using the x-ray photoemission spectroscopy and convergent beam electron diffraction have established that the polarity of GaN film on sapphire is along either (0001) or (000-1) direction [247, 248]. Our synthesis involved a sapphire substrate and as shown in Figure 5.9, the specimen preparation results in the poling direction perpendicular to the applied electrical field for our in-situ TEM experiments.

The TEM specimen is prepared using focused ion beam (FIB) with the processing steps shown in Figure 5.9. The sapphire illustrated in Figure 5.9a has a (0001) growth direction, typical for GaN growth. A microscale coupon is cut from the GaN film (Figure 5.9b) using coarse current density, which is then ion milled using fine current density to minimize ion beam damage. At around 100 nm thickness, the specimen is electron transparent in the direction perpendicular to [0001]. A rectangular coupon from the GaN film is then cut and transferred on a microfabricated device so that its [0001] lies vertical to the electron beam and electrical field. The entire setup can be accommodated in a custom designed TEM holder with electrical biasing capability for in-situ testing. Also shown in Figure 5.9g is a Raman spectra obtained from a Horiba Vlabinir tool using 532 nm wavelength laser and a 2048 x 512 pixel back-illuminated, liquid nitrogen cooled InGaAs array detector. The spectra is obtained while the GaN film is on the sapphire substrate. The sharp peak at 570 cm^{-1} is indicative of hexagonal structure and about 470 MPa residual stress during deposition [249].

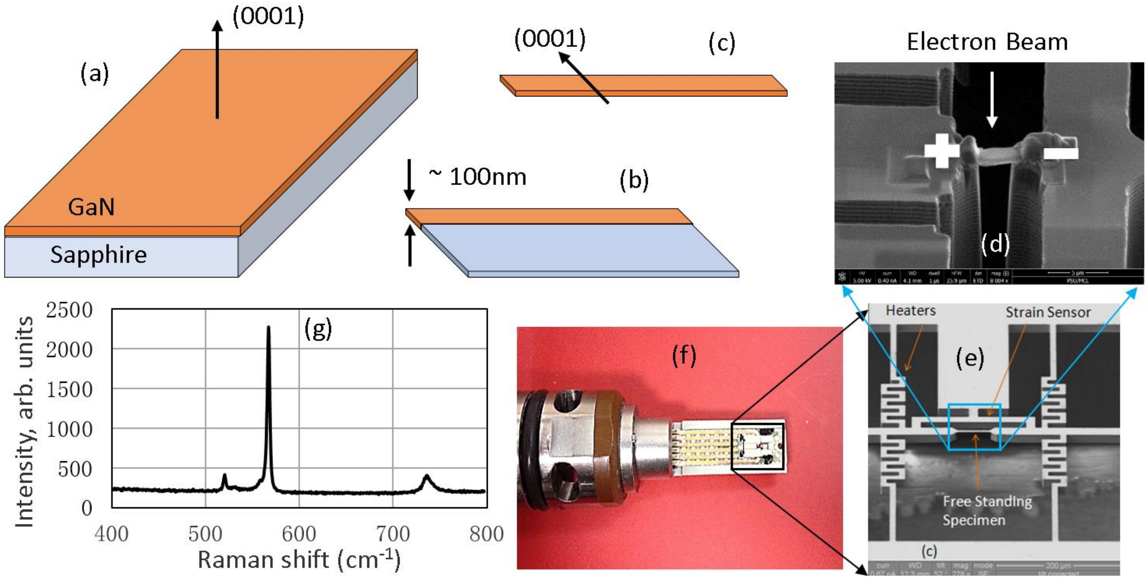
(0001)
(a)
GaN
Sapphire
(0001)
(c)
~ 100nm
(b)
Electron Beam
+
−
(d)
2500
2000
1500
1000
500
0
Intensity, arb. units
(g)
400
500
600
700
800
Raman shift (cm-1)
(f)
Heaters
Strain Sensor
(e)
Free Standing Specimen
(c)

Figure 5.9. (a-c) TEM sample preparation process using FIB. A 100 nm thin coupon is milled and then rotated before (d) mounting on two electrodes on (e) micro device that fits a (f) TEM specimen holder with electrical biasing capability. (g) Raman spectra of the GaN specimen showing excellent crystallinity.

5.2.3 Results and Discussion

Electrical stressing experiments were performed in-situ inside a FEI Tecnai TEM with an acceleration voltage of 200 kV. Bright field TEM images and selected area diffraction patterns are recorded at each biasing step. Figure 5.10 shows a few representative snapshots of the experiments, showing the single crystallinity of the specimens. Other than appearances of a few dark spots, which could be dislocation loops, we did not observe any dramatic changes till the voltage level of 20 V. At this voltage level, the diffraction pattern showed a dramatic change within a very short instant of time. Such dynamics is common with the highly nonlinear nature of domain switching [250].

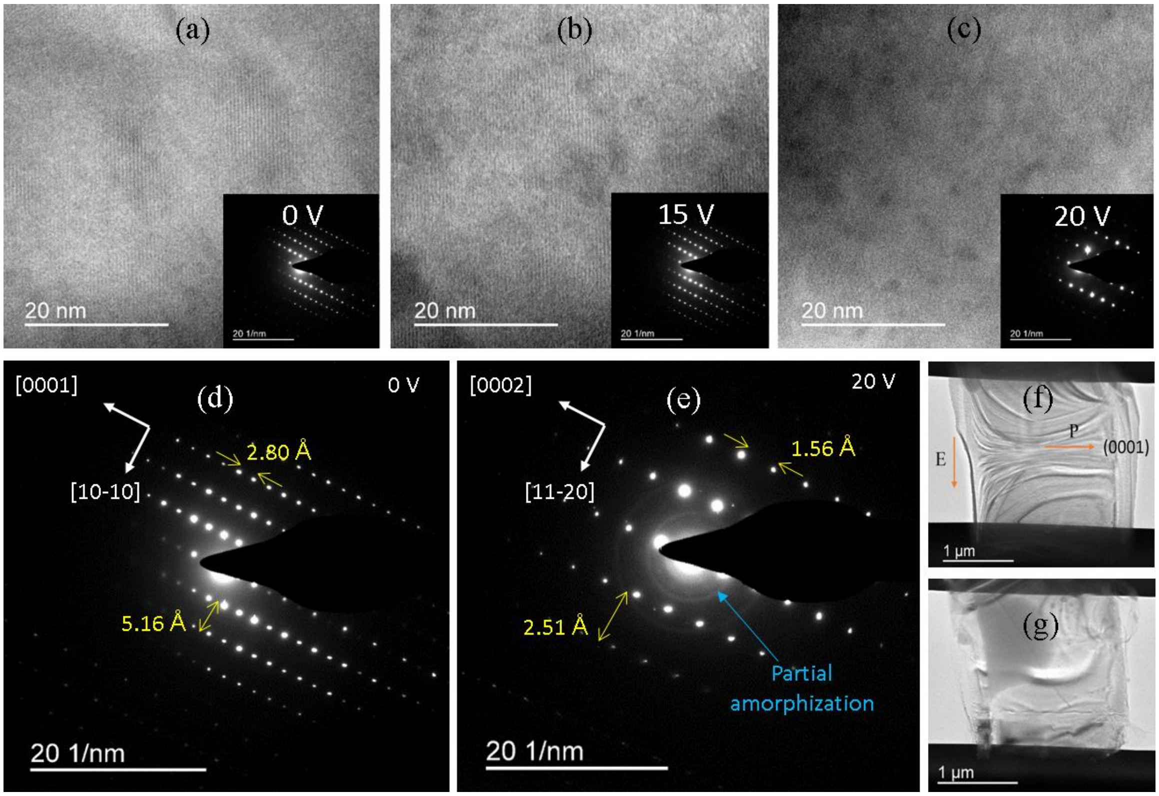
(a)
0 V
20 nm
20 1/nm
(b)
15 V
20 nm
20 1/nm
(c)
20 V
20 nm
20 1/nm
[0001]
(d)
0 V
2.80 Å
[10-10]
5.16 Å
20 1/nm
[0002]
(e)
20 V
1.56 Å
[11-20]
2.51 Å
Partial amorphization
20 1/nm
(f)
P
(0001)
E
1 μm
(g)
1 μm

Figure 5.10. (a-c) Bright field TEM image at various levels of electrical biasing. (d) Selected area diffraction pattern before biasing and (e) at 20 V. Low magnification images of the specimen (f) and (g) after domain switching and catastrophic failure. The poling and electrical field directions are highlighted using arrows.

To highlight the effects of domain switching, we show low magnification bright field TEM images before and after the domain switching in Figures 5.10d and 5.10e. We measured the reciprocal lattice constants of GaN before and after biasing. Before biasing, the lattice constants are measured to be 0.516 nm and 0.280 nm, which corresponds to [0001] and [10-10] directions, respectively. At 20 V, a dramatic difference in the d-spacings were measured as 0.254 nm and 0.156 nm, which are verified to be along [0002] and [11-20] directions, respectively. These values indicate a 90° rotation in the crystalline structure of GaN [251]. Intriguingly, both these directions in GaN are non-polar, and one would rather expect the polar [0001] to align with the electrical field. The sudden event of the rotation does not allow us to elucidate the detailed mechanisms with the 32 frames per second video acquisition in the TEM. Figures 5.10f and 5.10g show low magnification images of the specimen. The fringes visible in these images is due to single tilt TEM specimen holder used to image the single crystal specimen. These figures show sudden and appreciable change in crystallinity, which is also evident from Figure 5.10e. Here, partial amorphization is evident from the emergence of the rings in the diffraction pattern. We did not observe any grooving or pitting type structural degradation reported in the literature [252, 253]. This is because our specimen is a blanket film, whereas these stress relaxation mechanism need an interface between AlGaN and GaN, where the stress in inherently concentrated. These defects are observed in time dependent loading, compared to catastrophic failure in our case.

Domain switching is a non-linear and irreversible process. This agrees with the leakage current measured during the in-situ TEM experiments shown in Figure 5.11a, where the leakage current increases as a function of the applied bias. However, the domain switching was too fast to record the leakage current, which turned to zero, indicating catastrophic mechanical breakdown. This could be a result of increased stress intensity factor due to electrical loading and domain switching [254]. We performed few sets of experiments, which consistently showed similar behavior, albeit the value of switching voltage varied from specimen to specimen. Such variation was most likely due to the introduction of contamination in the specimen during focused ion beam milling of the specimen. We also performed separate sets of experiments, where the electrical field direction coincided with the poling direction, where we did not observe any domain switching in these cases.

We hypothesize that the observed domain switching in our 100 nm thick specimens is a size effect, compounded from both electrical and mechanical domains. In the electrical domain, piezoelectric coefficients of GaN are larger compared to the bulk, which suggests higher internal energy for the same applied bias. For example, experiments suggest that GaN nanowires with similar cross-section (65 -190 nm diameter) can exhibit order of magnitude stronger piezoelectricity compared to bulk [255]. Around the 100 nm length-scale, the d_{13} coefficient for GaN is measured to be -9.2 pm/V [255], compared to the literature value of -1.0 pm/V [256]. According to equation 1, 20 V in our specimen configuration results in the critical internal energy for 90° domain switching, which would take place in a typical GaN film at 55 Volts. This is too large field for bulk GaN, which means dielectric breakdown will take place before domain switching. To verify this hypothesis, we performed dielectric breakdown tests on a 2 micron thick GaN film. The results are shown in Figure 5.11b, where the large increase in leakage current reflects typical electrical breakdown and not domain switching. From a mechanical perspective, nanoscale GaN can absorb significantly higher energy before fracture. For example, fracture strength of 100 nm diameter GaN nanowires is about six times higher compared to 700 nm diameter ones. Similarly, fracture strain can be two times higher [257]. It is therefore plausible that large internal energies can be generated in nanoscale GaN films at comparative smaller applied bias. The mechanical size effect makes the material is stronger, so that it does not fracture before the critical energy for domain switching is achieved.

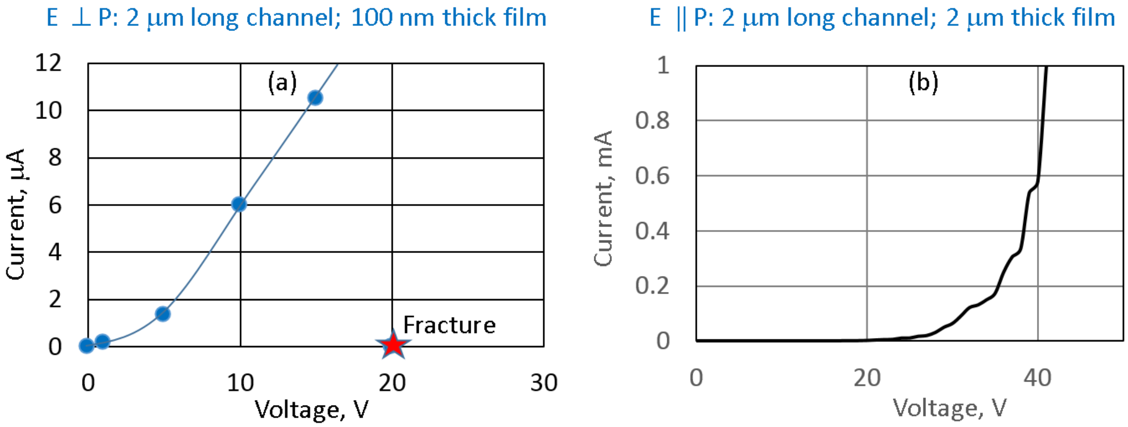

Figure 5.11. (a) Domain switching in 100 nm thick film occurs at 20 V (b) about 55 V is needed to store the same internal energy in a 2 micron thick film, which is long preceded by electrical breakdown, a reason domain switching in GaN is typically not observed at the bulk scale.

5.2.4 Conclusion

In conclusion, we report in-situ TEM evidence of 90° domain switching in 100 nm thick GaN films. Even though the underlying physics of domain switching is studied for a variety of piezoelectric materials, it is not reported in the literature before for GaN. This is because of the weaker piezoelectric coefficients for GaN, which imply that very large electrical field is needed for the critical internal energy needed for domain switching and the material fails by ordinary electrical breakdown. This mechanism changes at the nanoscale, where the strong piezoelectric size effect enables storage of the critical energy at electrical fields below the breakdown field, allowing us to observe domain switching in nanoscale GaN films.

Chapter 6

Degradation

Contents of this chapter are based on the following journal articles:

- **Baoming Wang**, Aman Haque, Alexander E. Mag-isa, Hak-Joo Lee "High temperature and current density induced degradation of multi-layer graphene", *Applied Physics Letters* 107, 163103 (2015)

  Author of this dissertation designed the experiment, performed device preparation, experimentation, data analysis and manuscript writing. Aman Haque took part in experiment design, data analysis and manuscript writing. Alexander E. Mag-isa, Hak-Joo Lee prepared the sample and involved in corresponding manuscript preparation.

- **Baoming Wang**, SM Eichfield, Dixiong Wang, JA Robinson, MA Haque, "In situ degradation studies of two-dimensional WSe_2–graphene heterostructures", *Nanoscale*, 2015,7, 14489-14495

  Author of this dissertation designed the experiment, performed device preparation, experimentation, data analysis and manuscript writing. Aman Haque and JA Robinson took part in experiment design, data analysis and manuscript writing. SM Eichfield, Dixiong Wang prepared the sample and involved in corresponding manuscript preparation.

6.1 High Temperature and Current Density Induced Degradation of Multi-layer Graphene

We present evidence of moderate current density, when accompanied with high temperature, promoting migration of foreign atoms on the surface of multi-layer graphene. Our *in situ* transmission electron microscope (TEM) experiments show migration of silicon atoms at temperatures above 800 °C and current density around 4.2×10^7 A/cm^2. Originating from the micro-machined silicon structures that clamp the freestanding specimen, the atoms are observed to react with the carbon atoms in the multi-layer graphene to produce silicon carbide at 900-1000 °C temperature. In absence of electrical current, there is no migration of silicon and only pyrolysis of polymeric residue is observed.

6.1.1 Background and Motivation

Graphene is a two-dimensional (2D) layer of sp2-hybridized carbon atoms arranged in a honeycomb lattice. Atomic thickness, covalent in plane bonding and pristine all-surface features make it a transformational material with close to theoretical limits performance characteristics in almost all physical and chemical domains. Young’s modulus and intrinsic strength of graphene are reported to be 1 TPa and 130 GPa respectively [258], dwarfing those of steel (0.2TPa and 0.7 GPa). It shows outstanding room temperature electronic mobility [259], as high as 2.5×10^5 cm^2 V^{-1} s^{-1} and thermal conductivity [260] exceeding 5000 W m^{-1} K^{-1}. It is an attractive electronic material with far reaching application potentials as in high-frequency devices, touch screens, flexible and wearable devices, ultrasensitive sensors, nano- electromechanical systems (NEMS), super-dense data storage, photonic/photo-voltaic devices, batteries and super-capacitors [261, 262].

The foundational concept of this letter is that presence of foreign atoms, whether from unintentional contamination or intentional doping, has a strong influence on the properties of graphene and hence reliability of the graphene based devices [263]. Significant efforts in both contamination cleanup [150, 264] and developing contamination free processes [265, 266] involve lower temperatures. Electrical annealing has also been studied for graphene [267, 268]. The motivation for this study comes from the observation that very little or no studies are available on the combination of thermal and electrical annealing. We propose that the contamination effects can be worse at higher temperatures and current density for two reasons. Firstly, even for the cleanest transfer process, high current density and temperature can facilitate migration of atoms through electro and thermo migration phenomena. For example, the diffusion barrier for silicon on graphene can be as small as 0.06 eV [269], suggesting surface diffusion based migration and accumulation of silicon from the substrate to graphene at higher temperatures. Secondly, high temperature can initiate localized alloying of the foreign material with graphene, thereby changing its crystallinity. In this letter, we demonstrate these effects by preparing freestanding multi-layer graphene specimens with initial contamination and then raise the temperature and current density in-situ inside a TEM to visualize the migration of atoms from the substrate and subsequent alloying. The results show that thermal and electrical annealing mechanisms are not straightforward as often claimed in the literature – a finding that will impact our understanding in the reliability issues in graphene based devices.

6.1.2 Experimental Setup

We adopt an in-situ TEM technique so that both high-resolution imaging and diffraction patterns can be obtained from the specimen in real time. Figure 6.1a shows a micro-electro-mechanical (MEMS) device with a set of electro-thermal actuators and a heater. The device is fabricated from heavily doped silicon-on-insulator wafers as described previously [270]. Pristine multi-layer graphene flakes were mechanically exfoliated from natural graphite (NGS Naturgraphit GmbH) and collected on an oxide coated silicon substrate. They were then transferred to the MEMS device using 50 nm thick PMMA (950 A4, Microchem) carrier films supported by a thermal release tape (TRT) containing a 7 mm- hole in the center and then soaked in 30% Potassium hydroxide solution. After etching, the TRT supports the fragile PMMA membrane which in-turn carries the multi-layer graphene crystal. After rinsing in de-ionized water and subsequent drying, the specimen is positioned and aligned so that the multi-layer graphene side is in contact with the silicon structures of the MEMS device. Adhesion is ensured by lightly pressing the PMMA/multi-layer graphene structure onto the device followed by heating in an oven at 120°C for 4 hours. Finally, the PMMA is removed by soaking in acetone for at least 1 hour. Figure 6.1a shows the MEMS device on which locations X and Y schematically shows specimens aligned to the perpendicular and parallel to the direction of electrical biasing. In these locations, the multi-layer graphene flakes are freestanding and supported only at the two ends by the heavily doped silicon MEMS structures. This is schematically shown in Figure 6.1b. Figures 6.1c and 6.1d show scanning electron micrographs of these specimens for zoomed view. Even though the actuators and heaters mainly raise the specimen temperature upon electrical biasing, the difference is the electrical current flow in the specimen. The multi-layer graphene flake located on the actuator (Figure 6.1c) has negligible current density in its freestanding segments. When located on the serpentine heater, (Figure 6.1d), the freestanding segment acts as a current flow path parallel to the silicon heater and the current density depends on the respective electrical resistance values.

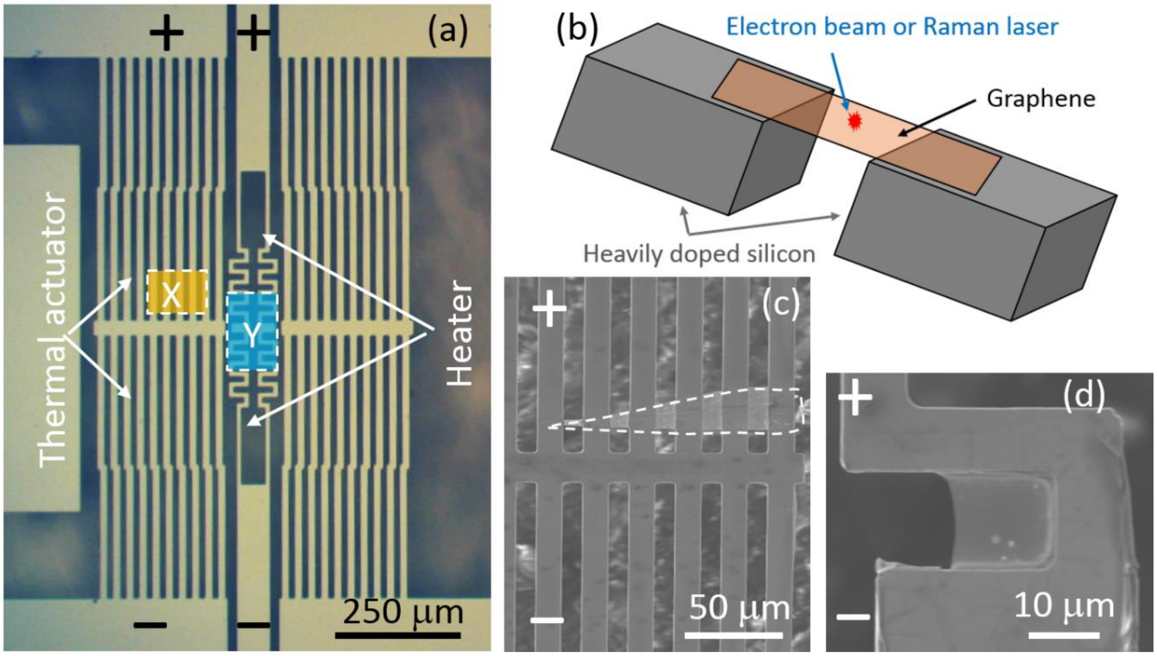

Figure 6.1. (a) Optical image of a micro-electro-mechanical device with specimens schematically located at X and Y positions, (b) schematic diagram of the freestanding specimen (c, d) scanning electron image of the specimens at X and Y locations.

To characterize the as-prepared specimen, we performed both TEM electron diffraction and Raman spectroscopy. Figure 6.2a shows the TEM diffraction pattern of one specimen indexed with multi-layer graphene lattice (red dots are slightly displaced to show the actual diffraction spots). The Raman spectra of the as-prepared specimens also showed excellent agreement with the signature spectra of graphene [271]. This is shown in Figure 6.2b. By comparing the ratio of the G and 2D peak intensities with reference studies in the literature [271], we note that the specimens are mostly about 4-5 layers of graphene. The resistance of the multi-layer graphene segment is about 7.5±2.5 ohms, which is very close to that of the heater (5 ohms). To approximate the current density, we multiply the specimen width (fairly uniform as shown in Figure 6.1d), we obtain the cross-sectional area of the specimen by) with the thickness of 4-5 layers graphene. Depending on the applied bias, we can achieve current density of up to 4.5x10^{7} A/cm^{2}, which is lower than the known breakdown strength reported in the literature [272]. The temperature of the device is measured with an infrared microscope under 1x10^{-4} Torr vacuum for various values of input current, which is then used to calibrate a finite element model to estimate the actual values in this study.

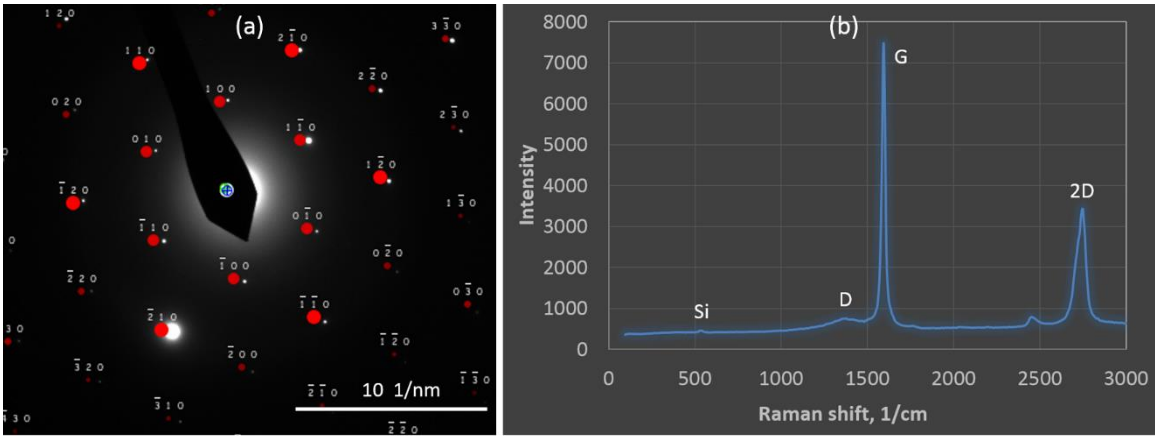

Figure 6.2. (a) TEM electron diffraction and (b) Raman spectra of the freestanding multi-layer graphene specimen before the passage of heat and/or current.

6.1.3 Results and Discussion

The MEMS device fits a JEOL 2010 TEM specimen holder with electrical biasing capability. All the experiments were performed at 80 kV acceleration to minimize electron beam damage. The first set of experiments was performed on the specimen on the serpentine heater that allows both heat and current flow in the specimen. The temperature and resistance of the heater are measured for each values of input current. The resistivity of the multi-layer graphene specimen is approximated as $\rho(T)/\rho(T=300\ K) = 1.436 - 0.00147\ T$ [273]. This allows us to estimate the current density in multi-layer graphene. At about 900 ºC, we observed motion of foreign atoms, similar to waves, on the multi-layer graphene. Figures 6.3a-c show the motion of the wave front with speed as high as 80 nm/sec. The arrows indicate the location of the wave front only, and the overall direction of the motion is towards the direction of the current. The migrating material is not any polymeric residue since, at this temperature, it would pyrolize and produce electron diffraction pattern similar to amorphous carbon. As analyzed later, the contaminant is silicon, coming from the MEMS structures that support two ends of the freestanding multi-layer graphene specimen. Since silicon melts at 1414 °C, we are confident that this is not due to melting of the silicon structures that clamp the freestanding specimen at the two ends. We hypothesize that the motion of silicon atoms is facilitated by the electro-thermal drift that originates from scattering of charge carriers in multi-layer graphene carrying electrical current. Since the motion of silicon wavers is aligned to the current flow direction, the underlying mechanism is electrical in nature. The driving force in electromigration has been traditionally decomposed into the sum of a direct electrostatic force F_d (= $q_{eff}E$) and the electron wind force F_w. The wind force originates from the scattering of the charge carriers of graphene by the impurity atoms. This process results in a transfer of momentum from the scattered charge carriers to the impurities [274]. Typically, atomic diffusion is a random process with no preference in the direction of atomic jumps. However, when subjected to electron scattering, the atoms move out of the lattice equilibrium position with a bias provided by the momentum transfer from the electron to the atom biases the atomic jump in the direction of the electron flow [275]. Density functional theory studies have shown the charge transfer mechanisms in metals on top of graphene sheets [276, 277]. For bulk materials, the electron wind force on surface impurity atoms is insignificant. However, this can be tremendous for single layer graphene where motion of metallic clusters and adsorbates [274, 278] moving as fast as 1-10 cm/sec

[279] is reported. For our about 4-layer specimens, this force is somewhat weaker (we observed 80 nm/sec motion) but not negligible because of the predominance of the surface. A more recent study shows that silicon can migrate on graphene surface even with electron irradiation (no current flow) [280].

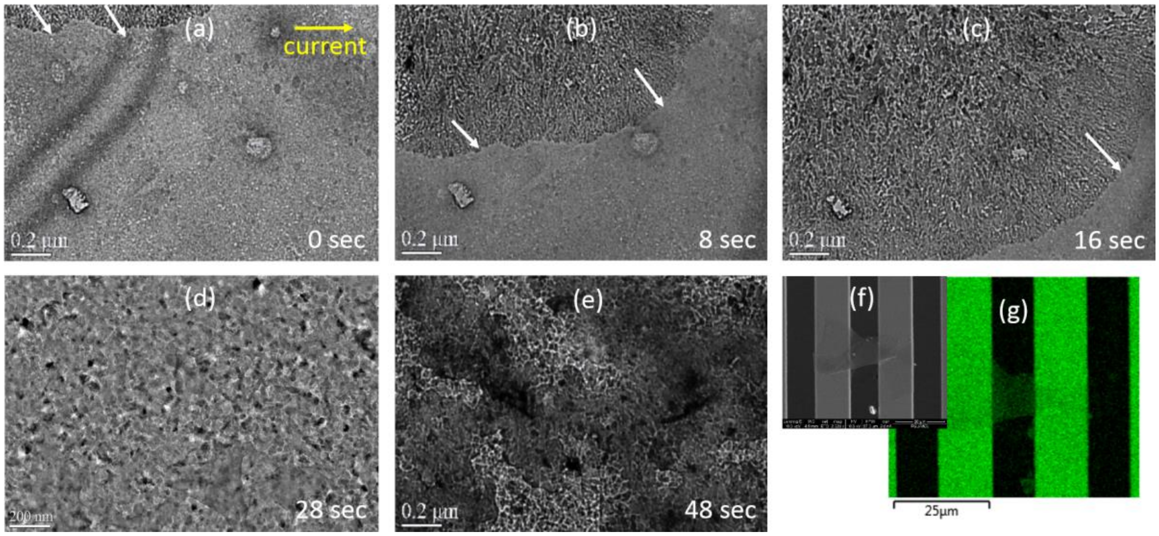

Figure 6.3. (a-c) Migration of silicon atoms on multi-layer graphene in form of waves at about 930 °C. The arrows indicate the silicon atom wave fronts. (d) microstructural change related to silicon carbide formation (e) continued migration of silicon atoms (f) SEM image of a specimen showing no melting of the silicon clamping ends (g) energy dispersive spectroscopy showing silicon over the freestanding region.

At temperatures around 900-1000 °C, the specimen microstructure dramatically changed in to nanocrystalline. This is also confirmed by the corresponding electron diffraction pattern in Figure 6.4a, when compared to Figure 6.2a. We have indexed the diffraction pattern, which did not match that of the diamond or graphitic forms of carbon, but a rather remarkable match was obtained for silicon carbide. This indicates that the migrating silicon and the carbon atoms from the multi-layer graphene have reacted at this temperature to form nanocrystalline silicon carbide. This reaction has been reported at temperature as low as 700 °C [281]. We propose that this reaction can continue as long as carbon atoms are available for the incoming flux of silicon atoms. Once the carbon atoms from the specimen are consumed by the silicon-carbon reaction, the subsequent silicon atoms cannot react and thus accumulates on the silicon carbide film as silicon layers. A surface probing technique, such as Raman spectroscopy, would therefore show signature silicon peaks, which is confirmed in Figure 6.4b.

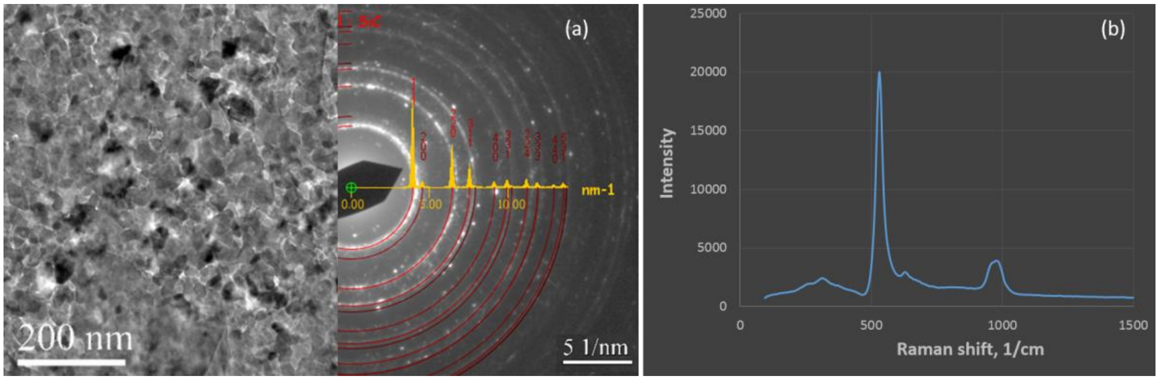

Figure 6.4. (a) TEM image of the nanocrystalline silicon carbide and corresponding diffraction pattern after indexing (b) Raman spectra of specimen corresponding to Figure 6.3f confirming decomposition of the carbon atoms followed by excessive migration of silicon.

A remarkably different scenario is seen when the graphene specimen is heated without electrical current flow in it. In this case, at lower temperatures, the PMMA residue is seen to move over the specimen surface due to thermo-migration. However, in absence of electrical current, the residue is not eliminated completely. Rather, it remains in percolated form on the multi-layer graphene. This is shown in Figure 6.5a. Further increase in temperature only converts the residue to amorphous carbon as shown in Figure 6.5b. The diffraction patterns do not match with silicon carbide, which suggest that electrical current flow is the main reason of migration of silicon atoms over graphene.

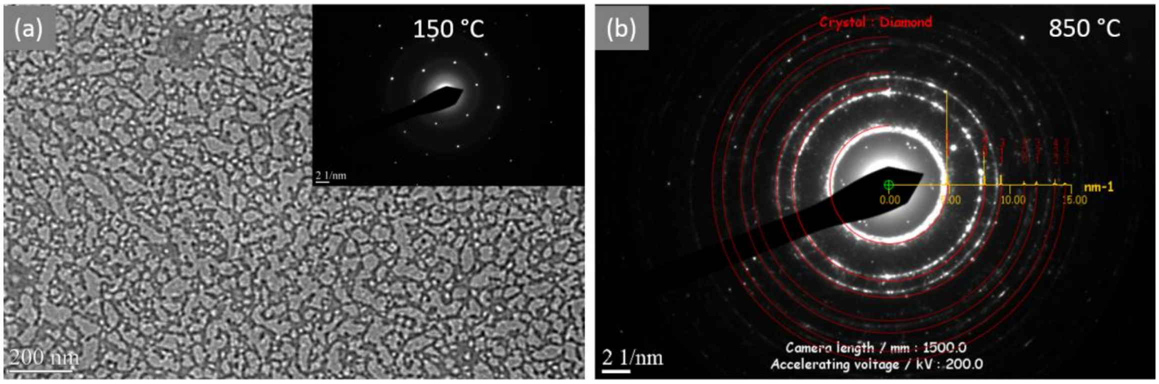

Figure 6.5. (a) Heating multi-layer graphene specimen in absence of electrical current induces thermal motion of polymeric residue, which (b) pyrolizes at elevated temperatures. No migration of silicon is seen.

6.1.4 Conclusion

In conclusion, using the example of a popular polymer (PMMA) for graphene transfer, we aimed to understand of the fundamentals of competing mechanisms in thermal and electrical annealing. Since our annealing experiments are performed under vacuum, and not under air or oxygen-rich environments, we did not observe complete removal of the PMMA contamination. However, the contribution of this study is in the role of current density and combination higher temperature, which is not studied in the literature. We show that while thermal annealing processes may remove contaminants and defects, electromigration can bring in new contaminants by giving them exceptional mobility over the multi-layer graphene surface. In particular, we show migration of silicon from the supporting MEMS structures to freestanding multi-layer graphene that finally led to alloying in form of silicon carbide at high temperatures. These findings may have implications on the performance and reliability of graphene based applications, with or without apparent contamination and insinuate the inherent risks of alloying during mass transport of graphene at higher temperature and current density.

6.2 In-situ Degradation Studies of Two-dimensional WSe_2-Graphene Heterostructures

Heterostructures of two-dimensional materials can be vulnerable to thermal degradation due to structural and interfacial defects as well as thermal expansion mismatch, yet a systematic study is yet to exist in the literature. In this study, we investigate the degradation of freestanding WSe_2-graphene heterostructures due to heat and charge flow by performing insitu experiments inside the transmission electron microscope. Experimental results show that purely thermal loading requires higher temperatures (>850 °C), about 150 °C higher than that under combined electrical and thermal loading. In both cases, selenium is the first element to decompose and migration of silicon atoms from the test structure to the freestanding specimen initiate rapid degradation through the formation of tungsten disilicide and silicon carbide formation. The role of current flow is to enhance the migration of silicon from the sample holder and to knock-out the selenium atoms. The findings of this study add fundamental insights to the degradation of WSe_2-graphene heterostructures and inspire their application in harsh environment electronics.

6.2.1 Introduction

Two-dimensional materials and their heterostructures have received tremendous attention for unusual physical phenomena and promise in opto/electronics, energy conversion, physical and bio sensing as well as bulk composite applications [261]. Their layered structure, with strong in-plane covalent or ionic and weak cross-plane van der Waals bonding, enables stability in mono to few-layer form. The predominance of surface atoms without the deleterious dangling bond defects results in unprecedented charge and heat transport confined to a plane [282]. This allows aggressive transistor channel length scaling without compromising the materials intrinsic properties. Starting with graphene, the literature has seen explosive growth in these phenomena and applications, especially after materials with complementary characteristics. For example, electrically insulating yet thermally conducting hexagonal boron nitride [269] and semiconducting 2D transition metal dichalcogenides (TMD), such as MoS_2 and WSe_2 [283] have catalysed the concept and realization of heterostructures [284]. In comparison, structural stability of these atomic layered structures have received less attention. In particular, very little is known about their thermal stability or degradation mechanisms, probably because their high temperature compatibility. Nevertheless, the predominance of surface atoms also makes 2D materials susceptible structural and topological defects as well as external stimuli. This is the core theme of this study, where we investigate the effects of heat and charge flow on the degradation of 2D WSe_2-graphene structure. The experiments are performed in-situ inside a transmission electron microscope (TEM) after integrating the specimens with micro-electro-mechanical devices for thermal and electrical loading.

Compared to graphene, TMDs are more attractive because of their electronic structure and its tunability that gives to rise the valley polarization, which lends to device physics in addition to charge and spin [285]. Quantum confinement effect alters the electronic structures in monolayer TMDs from an indirect to direct bandgap [118], enhancing light-matter-charge interactions as well as electrochemical reactivity. Even though MoS_2 has been popular in the literature, we focus on the emerging 2D version of WSe_2. It possesses mechanical flexibility, optical transparency and direct band gap of 1.65 eV, making monolayer WSe_2 attractive for electronic and optoelectronic devices.

[286, 287] It is composed of two-dimensional trilayer Se–W–Se structures, with a W atom plane in the middle of two hexagonal Se atom planes. It is also the first TMD material combining p-type and n-type characteristics (depending on the metal contact used), [288, 289] offering the possibility of complementary logic circuits in the same monolayer. Exfoliated monolayer WSe_2-based transistors show impressive carrier mobility [290] (up to 650 $cm^2 V^{-1} s^{-1}$) with $>10^6$ on/off ratio [291].

In this study, we focus on the structural stability and degradation of 2D heterostructure of WSe_2 on graphene, which is critical for device performance and reliability. Our motivation comes from the striking lack of research in this area involving 2D materials and their heterostructures. Limited studies on thermal degradation of graphene [292, 293] and layer by layer thinning of MoS_2 [294] indicate the influence of temperature. The reason could be the known electro-chemical and thermal stability of commonly studied 2D materials, such as graphene [295]. However, this may not necessarily true for emerging materials. [296] Even for chemically and thermal stable components, their heterostructures can be vulnerable to degradation due to structural and interfacial defects, especially at higher temperatures and/or electrical current densities. Thermal expansion mismatch can have strong influence since their negative thermal expansion coefficients imply tensile strain at higher temperatures. To the best of our knowledge, no study exists in the literature on degradation of either WSe_2 or any related heterostructures. Similar shortcoming for most other 2D materials in the literature highlights the significance of this research. We also note that synthesis of 2D WSe_2 [297], in particular heterostructures [298], remains challenging and emerging area of research in the literature.

6.2.2 Experimental Setup

The experimental setup consists of a freestanding WSe_2-graphene heterostructure integrated with a micro-electro-mechanical device with a micro-actuator and a micro heater. Figure 6.6a shows the entire setup, where the 5mm x 3 mm size device is mounted on an electrical biasing TEM specimen holder. The test chip was fabricated on a heavily doped silicon-on-insulator wafer with 20 micron thick device layer. After photolithographic patterning, deep reactive ion etching was used to realize the device structure. A second lithography with backside alignment was performed on the handle layer, followed by a through-the-thickness deep reactive ion etching. The buried oxide was removed by vapor phase hydro-fluoric acid etch to make the device freely suspended. This allows imaging and diffraction of any electron transparent specimen inside the TEM. Figure 6.6b shows scanning electron micrograph of the device after wire-bonded to the TEM specimen holder. It also shows two sets of electrodes, PQ and RS, to power up the heaters and thermal actuators respectively. Even though they both operate on Joule heating, their different geometry leads to different specimen configuration upon electrical biasing. Figure 6.6c shows the heaters. When transferred on to it, 2D materials would form rectangular bridges along the direction of the current flow as shown in Figure 6.6c. When the PQ electrodes are electrically biased, the current will pass through both the silicon heater and the freestanding specimen. Therefore, the specimen experiences both thermal and electrical loading. Figure 6.6e illustrates the different nature of specimen transfer in the actuator area, where the suspended specimens are aligned perpendicular to the direction of electrical biasing (electrodes RS). This results in pure thermal loading of the specimen.

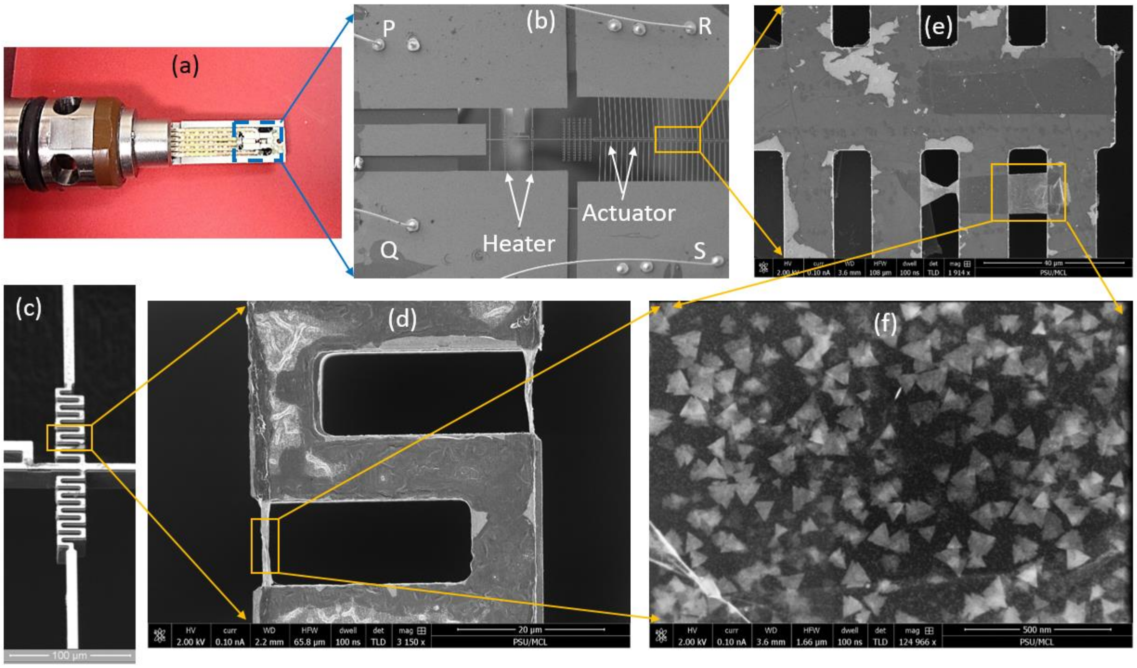

Figure 6.6. (a) Experimental setup consisting of a micro-electro-mechanical devices mounted on an electrical biasing TEM holder (b) Zoomed view of the device showing heater and actuator areas (c) Zoomed view of a heater (d) Zoomed view of a freestanding WSe_2-graphene heterostructure on the heater area (e) Zoomed view of a freestanding specimen in the actuator area (f) Triangle shaped domains of highly crystalline WSe_2 on graphene.

While most of the monolayer WSe_2 is commonly obtained from mechanical exfoliation, [290, 299] we directly chemical vapour deposited (CVD) the WSe_2 on freestanding bilayer graphene already laid out on the micro device. CVD growth of WSe_2 is only emerging in the literature [297] and is better suited towards building heterostructures [300] on graphene compared to other vapour transport, [301] or transition metal selenization [302] processes. Graphene films are grown via chemical vapor deposition on copper substrates [303], and subsequently transferred to the fabricated TEM test structures (Fig 1a-d). Subsequently, samples were loaded into a metal-organic chemical vapour deposition system, where WSe_2 domains were synthesized from tungsten hexacarbonyl ($W(CO)_6$) and dimethylselenide ($(CH_3)_2Se$) on the suspended graphene layers at 800ºC and 700 Torr using Se/W ratio of 14000 [298] (Fig. 1f). All the experiments in this study were performed at 80 kV acceleration voltage in a JEOL 2010 TEM. Signs of electron beam induced damage was rigorously monitored in the specimen.

6.2.3 Results and Discussion

In-situ TEM experiments were performed to visualize the degradation of WSe_2-graphene heterostructure under purely thermal as well as thermo-electrical loading. To estimate the temperature of the micromachined heaters as function of the supplied current, an infrared microscope was used to measure the real temperature of a similar device at 20 milli-Torr vacuum. The experimental data is then used to calibrate a finite element model that simulates the device temperature. The model accounts for the radiation losses that dominates over convection at these vacuum levels. The technique is then validated by melting thin films of pure metals with known melting points. Details of the temperature estimation technique is given elsewhere [116].

As shown in Figure 6.6, the position and orientation of the 2D heterostructure can be exploited to control the flow of heat and charge in it. Figure 6.7 shows TEM images and diffraction patterns after passing current through the thermal actuator (Figure 6.6e). The discrete spots in the diffraction pattern come from two layers of graphene, while the ring patterns come from the smaller WSe2 domains. In this specimen configuration, there is no current flow in the specimen and the degradation effects are due to temperature only. The specimen temperature was incremented by 20 °C after 700 °C with hold times of 30 minutes between each increments. The specimen showed remarkable thermal stability up to about 800°C, since almost no change in microstructure or diffraction pattern was observed. . Figure 6.7a shows the specimen at 820°C when the sharp edges of the triangular WSe_2 domains start to lose sharpness. This is quite expected since the edges of the domains possess higher energy, they are the first ones to show instability. The degradation process was very rapid at this phase since WSe_2 started to melt at 860°C. This matches well with the decomposition temperature of bulk WSe_2 in vacuum [298]. The diffraction pattern at this temperature suggests that graphene maintains its integrity. It also suggests presence of silicon carbide in the specimen. The observation of degradation at temperature similar to deposition indicates stability of the heterostructure under high vacuum condition inside the TEM. In comparison, the deposition was performed at 700 Torr pressure. At only 880°C, graphene also becomes unstable and undergoes a phase change reflected by very strong change in contrast in the bright field mode. The multitudes of diffused rings in the corresponding diffraction patterns suggests that the single crystal degraded to nanocrystalline domains of many different alloys or elements. We indexed these rings to identify the constituents and found no trace of pure tungsten or selenium. The pattern matched very well with silicon carbide. However, there were other rings that could not be unambiguously indexed, suggesting other alloys than pure tungsten or selenium.

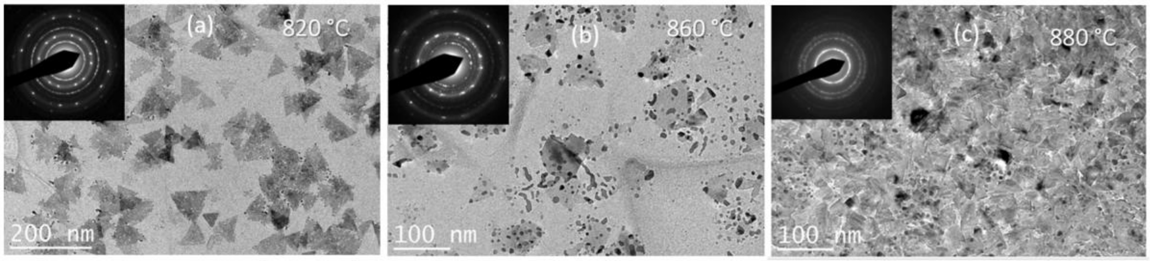

Figure 6.7. In-situ TEM observation of the microstructure and corresponding electron diffraction patterns at various temperatures.

To understand the basic mechanisms behind thermal degradation, we performed both energy dispersive (EDS) and Raman spectroscopy on the specimen. A WITec confocal Raman system with a 488nm excitation wavelength was used this study. These results are shown in Figure

6.8. Very strong presence of silicon was observed which is interesting since the freestanding specimen was supported at the ends by the micromachined silicon structures. The growth and transfer process are least likely to contaminate with silicon. The gradient in the silicon profile (Figure 6.8a) indicates the migration of silicon from the test device structures to the freestanding WSe_2-graphene surface. This atomic scale mass transfer takes place due to surface diffusion. Density functional theory (DFT) suggests the diffusion barrier for silicon on graphene can be as small as 0.06 eV, and van der Waals interaction between silicon adatom and graphene sheet has only a minimal effect on the diffusion barrier[3]. While high mobility of silicon adatoms on graphene can explain the presence of silicon in our specimen, the Raman peak at 520 cm^{-1} is most likely from the micromachined silicon structures. The Raman spectra confirms the other alloys originating from silicon, carbon and tungsten. For example the 330 and 450 cm^{-1} peaks indicate presence of due to tungsten disilicide [269]. Tungsten disilicide can nucleate at as low as 500 °C with ultra-fine grains that increase up to 160 nm at 800 °C [285]. Another alloy present was silicon carbide (SiC). The 800 cm^{-1} peak is the signature of 3C-SiC while the 900 band is for amorphous SiC [283]. Thermal degradation of the graphene is reflected by the G-band at about 1580 cm^{-1} showing the in-plane displacement of carbon atoms in the hexagonal sheets. The band at about 1350 cm^{-1} (D-band) is due to the disorder of the structure.

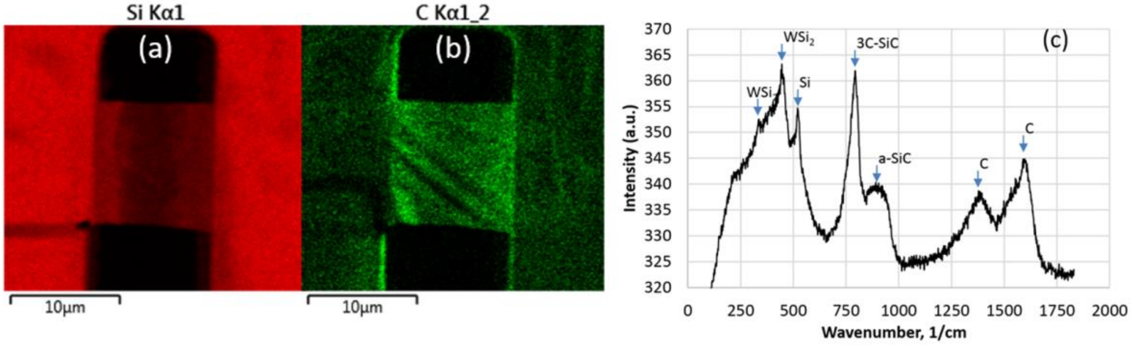

Figure 6.8. Energy dispersive spectroscopy of the thermally degraded WSe_2-graphene heterostructure showing (a) surface diffusion of silicon and (b) carbon (c) Raman spectra suggesting various alloys of tungsten, silicon and carbon.

The serpentine silicon heater structure (Figures 6.6c and 6.6d) induces a temperature field, which is uniform given the small size of the specimen. Since the specimen is electrically parallel to the heater and along the electrical biasing direction, it also experiences current flow. For such a parallel current flow, the current density in the specimen can be obtained from the respective resistances of the specimen and silicon structures. The resistance of the 10 micron wide, 10 micron long and 20 micron thick silicon beam is approximately 1 ohm after we measured its resistivity to be 0.002 ohm·cm. Similarly, resistance of the 2.7 micron wide, 10 micron long and 0.345 nm thick graphene specimen can be estimated to be 4625 ohms after measuring the resistivity to be $4.31e^{-5}$ ohm·cm. The current density in the specimen can be estimated from these figures after passing a known current in the heater.

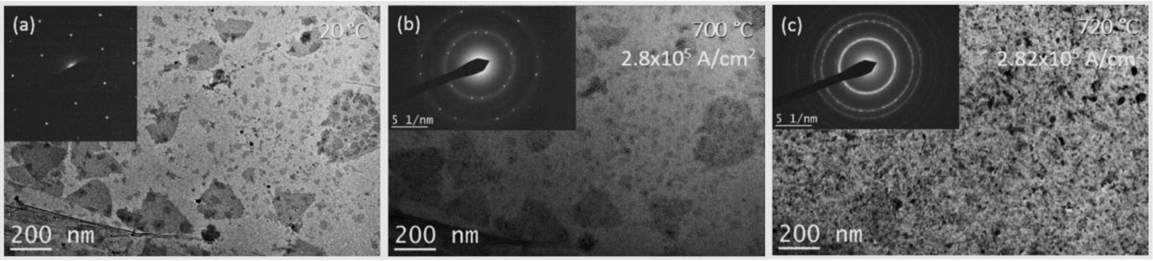

Figure 6.9. In-situ TEM observation of the microstructure and corresponding electron diffraction patterns at various temperatures and current densities.

A remarkable difference in degradation temperature and mechanism was observed (Figure 6.9) when passing current through the heater section (Figure 6.6c). At about 700 °C, the WSe_2 domains appear to blister and the corresponding TEM diffraction pattern shows tungsten only, suggesting the decomposition of selenium. We propose that the effect of the current density (about $2.8x10^5$ A/cm^2) in the specimen is to facilitate the knockout of the selenium atoms due to the momentum transfer of the electrons. At higher current density, the electron wind can promote transfer of silicon atom contaminants from the silicon heater to the graphene-WSe2 heterostructure through phenomena similar to electro and thermo migration [304, 305]. The role of silicon contamination is to create alloying effects after reacting with highly crystalline graphene. These alloys create nanocrystalline grains, thereby catastrophically degrading the specimen. In other words, the electron wind catalyses the decomposition, thereby lowering the temperature. We suggest that the influences of temperature and current are synergistic because the presence of current density results in the initiation of degradation at about 160 °C lower than thermal only decomposition. At about 720 °C, there is a very sharp contrast change in the specimen, after which the microstructure and diffraction pattern essentially appear to be similar to thermal degradation (Figure 6.7c) alone.

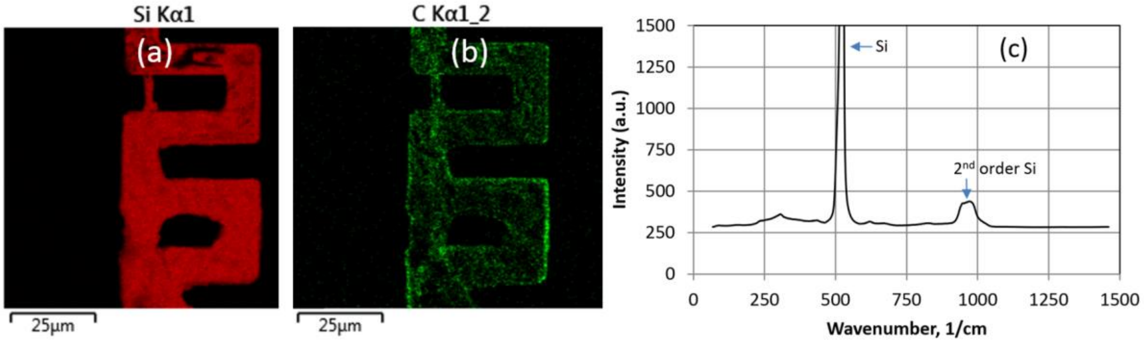

Figure 6.10. Energy dispersive spectroscopy of the electro-thermally degraded WSe_2-graphene heterostructure showing (a) surface diffusion of silicon and (b) carbon (c) Raman spectra suggesting alloying of silicon carbide and tungsten disilicide.

Energy dispersive spectroscopy in Figures 6.10a and 6.10b clearly show the presence of silicon, tungsten (overlaps with silicon) and carbon in the degraded specimen. The Raman spectroscopy in Figure 6.10c however shows predominance of silicon only. The wide (940 cm^{-1} to 990 cm^{-1}) peak can be related to the second-order transversal optical phonons as observed in bulk crystalline silicon [306]. SiC crystallites also show a wide peak at this wavenumber [307], but in that case, a first order peak would also have been present at 790 cm^{-1} This conflicts with the finding in Figure 6.10b, because carbon in form of alloys or allotropes must be present in the specimen. To resolve this, we examine the TEM diffraction patterns in Figures 6.7 and 6.9, where they were not indexed for legibility. The results are shown in Figure 6.11, where expected diffraction patterns for both Si and SiC are superimposed. Clearly, SiC is a better match, comparing the first two rings. We propose that both Si and SiC are present depending on the availability of Si through surface migration, which is not captured in the Raman spectra because it collects information from the specimen surface only. The migrated Si reacts with the carbon from degraded graphene to form SiC. At some point, all the carbon becomes depleted through this process. This is supported by the absence of carbon peaks, compared to purely thermal loading (Figure 6.8c). After this, Si continue to migrate over the SiC layer. Since TEM is a through the thickness technique, it shows both Si and SiC, whereas Raman spectroscopy shows the surface elements only. The depletion of carbon in Figure 6.10c indirectly suggests that the Si migration rate is higher in case of current flow compared to purely thermal degradation (Figure 6.8c). This can be explained by the fact that both electron wind and thermal effects (surface diffusion can be expressed as an Arrhenius type equation) are active in the former case.

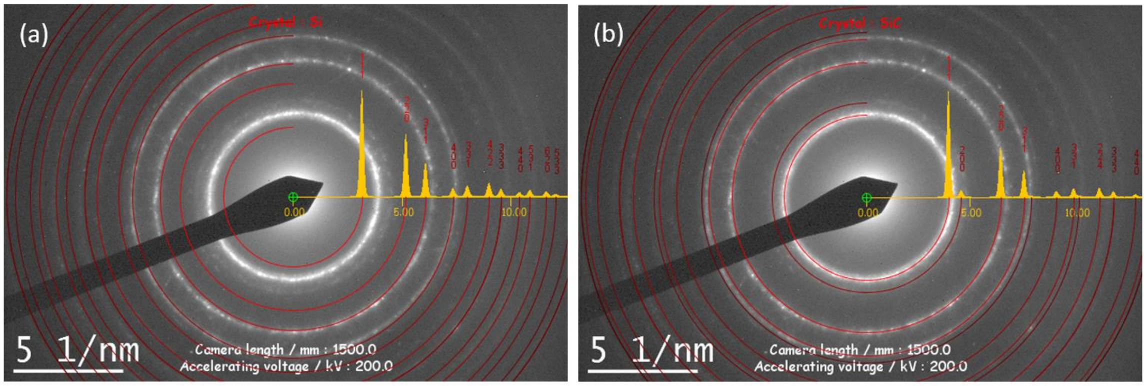

Figure 6.11. TEM diffraction pattern shown in Figures 6.7 and 6.9 indexed against (a) silicon and (b) silicon carbide.

6.2.4 Conclusion

In this study, we experimentally investigate the structural stability and degradation of 2D WSe_2-graphene heterostructures. We developed a micro-machined test bed with heaters electrodes to apply purely thermal as well as electro-thermal fields on the directly grown freestanding heterostructure specimens. The small size of the test bed allows us to perform the experiments in-situ inside a TEM. For purely thermal loading, we found that the degradation starts with the loss of selenium at around 850 °C. This temperature is very close to that for WSe_2 deposition, which suggests remarkable stability of the heterostructure under vacuum conditions. The study also shows that the high temperature facilitates migration of foreign (contaminant) atoms, which lead to catastrophic degradation in crystallinity. For example, silicon atoms from the test-bed structure migrates to the freestanding specimen through surface diffusion. This creates instability in the crystallographic structure and it becomes very sensitive to further increase in temperature. At about 900 °C, the migrated silicon spontaneously react with the tungsten and carbon to create nanocrystalline alloys of tungsten disilicide and silicon carbide. Under both electrical and thermal loading, the degradation process starts at temperatures 160 °C lower than thermal only loading. Even after this temperature difference, the final product is very similar, except the degraded material contains excess silicon and no carbon peaks in Raman spectra. Tungsten carbide does not form because of its very high formation temperature (around 1400 °C) for direct reaction between tungsten and carbon. In comparison, silicon reacts with carbon at 800 °C -1000 °C to form various polytypes of SiC, while tungsten reacts with carbon at even lower temperatures (700 °C -900 °C) to form WSi_2 [308]. Even though the present study is performed under idealized (vacuum) condition that far away from real life applications point of view, the findings inspire 2D applications under harsh environments and projects insights on degradation mechanisms. The contribution of this study is therefore to show that high temperature and current density can induce migration of foreign contaminants (silicon atoms that move from the supporting structures towards the specimen) due to phenomena similar to thermo and electromigration and alloying with foreign elements lead to catastrophic degradation in crystallinity.

Chapter 7

Sensitivity to Photons and Ions

Content of this chapter are based on the following journal articles:

- **Baoming Wang**, Christopher Muratore, Andrey A Voevodin, Md Amanul Haque, "Photo-sensitivity of large area physical vapor deposited mono and bilayer MoS_2", Nano Convergence, 2014. 1(1): p. 1-5

  Author of this dissertation designed the experiment, performed device preparation, experimentation, data analysis and manuscript writing. Aman Haque took part in experiment design, data analysis and manuscript writing. Christopher Muratore and Andrey A Voevodin prepared the sample and involved in corresponding manuscript preparation.

- **Baoming Wang**, Vikas Tomar, Khalid Hattar, Aman Haque, “Self-ion irradiation effects on mechanical properties of nanocrystalline zirconium films” Acta Materialia (submitted)

  Author of this dissertation designed the experiment, performed thin film and device preparation, experimentation, data analysis and manuscript writing. Aman Haque took part in experiment design, data analysis and manuscript writing. Vikas Tomar and Khalid Hattar performed ion-irradiation on the specimen and involved in corresponding manuscript preparation.

7.1 Photo-Sensitivity of Large Area Physical Vapor Deposited Mono and Bilayer MoS_2

We present photosensitivity in large area physical vapor deposited mono and bi-layer MoS_2 films. Photo-voltaic effect was observed in single layer MoS_2 without any apparent rectifying junctions, making device fabrication straightforward. For bi-layers, no such effect was present, suggesting strong size effect in light-matter interaction. The photo-voltaic effect was observed to highly direction dependent in the film plane, which suggests that the oblique deposition configuration plays a key role in developing the rectifying potential gradient. To the best of our knowledge, this is the first report of any large area and transfer free MoS_2 photo device with performance comparable to their exfoliated counterparts.

7.1.1 Introduction

Atomically thin semiconductor materials with large band gaps are touted for aggressively scaled electronic and optoelectronic applications [309]. Even though graphene does not have a band gap, its advent has galvanized the research on two-dimensional (2D) materials, notably the transition metal di-chalcogenides (TMD) [122]. The best example is molybdenum di-sulfide (MoS_2), which has received significant attention in the scientific community due to high carrier mobility, large current on/off ratio and excellent interface quality with the gate dielectrics [310]. Bulk MoS_2 has an indirect band gap of 1.2 eV which changes to a direct band gap of 1.83 eV for a monolayer MoS_2 [118, 311]. This leads to unprecedented light-matter interaction (high absorption coefficient and efficient electron-hole pair generation under photo-excitation) that has been studied in the form of photoluminescence, photoreponsivity, photoconductivity and photo-voltaics [119, 309, 312-315]. While the existing literature on mono or few-layer MoS_2 opto-electronics promise revolutionary capabilities of next generation devices, all these studies are performed on exfoliated flakes. Since exfoliation is not a sustainable path beyond basic science, there is a critical need for large area growth of mono-layer MoS_2 and its opto-electronic characterization. This provides the motivation for the present study, where we deposit large area (> cm^2) mono and bi-layer MoS_2 through magnetron sputtering and then study the effect of layer number on the interaction of matter and light. Since the deposition is directly performed on the desired substrate, our fabrication processes are performed directly on the specimen. Since no specimen transfer to another substrate is needed, contamination is potentially avoided. To the best of our knowledge, this is the first report of any large area, transfer free monolayer MoS_2 photo-voltaic or photo-detector device with performance comparable to their exfoliated counterparts.

7.1.2 Materials and Methods

We employed physical vapor deposition with base pressure below $5x10^{-9}$ Torr for atomically sharp and cleanliness of the interfaces. The mono and bi-layer specimens were grown on 100 nm thick thermal oxide coated silicon wafer pieces via magnetron sputtering using a solid 3.3 cm diameter MoS_2 target of 99.95% purity. The substrates were ultra-sonically cleaned prior to introduction via a vacuum load-lock and mounted on an electrically grounded fixture with heating and rotation features. The substrates were then heated to 350°C while ultra-high purity argon gas was introduced at a constant flow rate of 25 sccm to a pressure of 15 mTorr. Figure 7.1a shows the deposition setup schematically. Figure 7.1b shows the cross-sectional transmission electron microscopy of the specimens using a FEI Titan microscope for thickness measurements and calibration. The red dashed lines are superimposed on the figure to reveal the parallel atomic layers with likely turbo-stratic structure, where all basal planes are parallel and coplanar, but rotated about the crystals' z-axes. Or in other words, the specimens are not single crystal layers, but rather a large ensemble of small MoS_2 grains with uniform thickness and excellent lateral coherence. Specific processing conditions in terms of power modulation to the sputtering cathode were selected based on prior work [316, 317] to obtain atomic scale thickness control and very high crystallinity. Both Raman and x-ray photoelectron spectroscopy were then employed to characterize the specimens for thickness and stoichiometry. Figure 7.1c shows high resolution Mo 3d spectra with Mo peak shift to 229.0 eV indicating the +4 oxidation state for Mo, the hallmark of covalent bonding with sulfur in MoS_2 [318]. Figure 7.1c also shows a peak identified at 232.2 eV, which is the 3d3/2 peak for Mo and its shift from 231.4 eV also indicates bonding to S.

To verify the continuity and integrity of the deposited films, we prepared specimens with 1cm x 1cm active area, whereas the conventional practice is to pattern the semiconducting material as micro to nanoscale strips with metallic contacts as source and drain for a transistor configuration. A physical shadow mask was used to protect the specimen while exposing the four corners, on which 5 nm thick titanium and 100 nm thick gold were evaporated to make the electrical contacts. The chip is then mounted on another wafer piece with large gold plated electrodes using a thermal tape. The four corners of the specimen are then wire-bonded to the larger pads. Figure 7.1c shows a specimen prepared for van der Pauw characterization [319] of the electrical resistivity under both dark and illuminated conditions. The van der Pauw setup was calibrated with a calibration specimen to achieve ± 5% error limit. Table 1 shows the dark dc conductivity results for the specimens. Such high values of resistivity are due to the fact that ultra-high vacuum condition results in cleaner MoS_2 surfaces and domain structures. More importantly, the device fabrication process did not require the film to be transferred to a different substrate, so the associated contamination is avoided.

Table 7.1. Dark dc resistivity of the mono and bi-layer MoS_2 specimens.

Specimen type	Specimen 1	Specimen 2
Mono-layer	1.87×10^{-5} ohm-cm	1.88×10^{-5} ohm-cm
Bi-layer	2.98×10^{-5} ohm-cm	2.93×10^{-5} ohm-cm

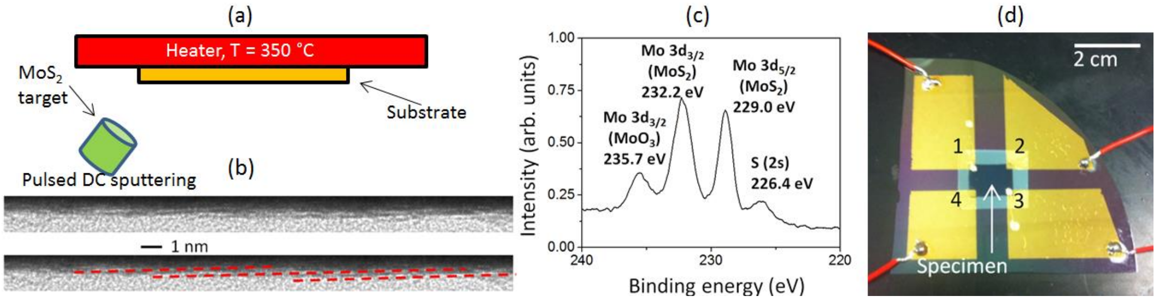

Figure 7.1. (a) Schematic of the pulsed dc magnetron sputtering configuration (b) Cross-sectional TEM (dashed lines are added for highlighting the MoS_2 layers, (c) X-ray photoelectron spectroscopy data revealing the structure (d) 1cm x 1cm MoS_2 specimen packaged for van der Pauw measurements showing the large active area.

7.1.3 Results and Discussion

After dark dc characterization, we illuminated the devices with a 30W light-bulb located at about 10 cm distance. The measured luminous flux per unit area was measured to be about 24 kLux using a light-meter. Figures 7.2a and 7.2b show the experimental results for the mono and bi-layer specimens. For the mono-layer, we observed the highest open circuit photo induced voltage of about 9.25 mV (without any applied bias). This value is significantly reduced to about 0.75 mV for the bi-layer specimen. These experiments were performed for negative bias to exhibit consistent behaviour. For even thicker specimens, we did not observe any appreciable photo-voltaic effects. We also observe that the effect is extremely direction dependent. For example, Figures 7.2c and

7.2d shows the photo-voltage measurement on the terminals perpendicular to that shown in Figures 7.2a and 7.2b. Such change in direction resulted in dramatic changes in the voltage obtained from the monolayer specimens (Figure 7.2c) and completely eliminated any such voltage in the bilayer specimens (Figure 7.2d). Note that in Figure 7.2d, the dark and illuminated behaviour is almost the same.

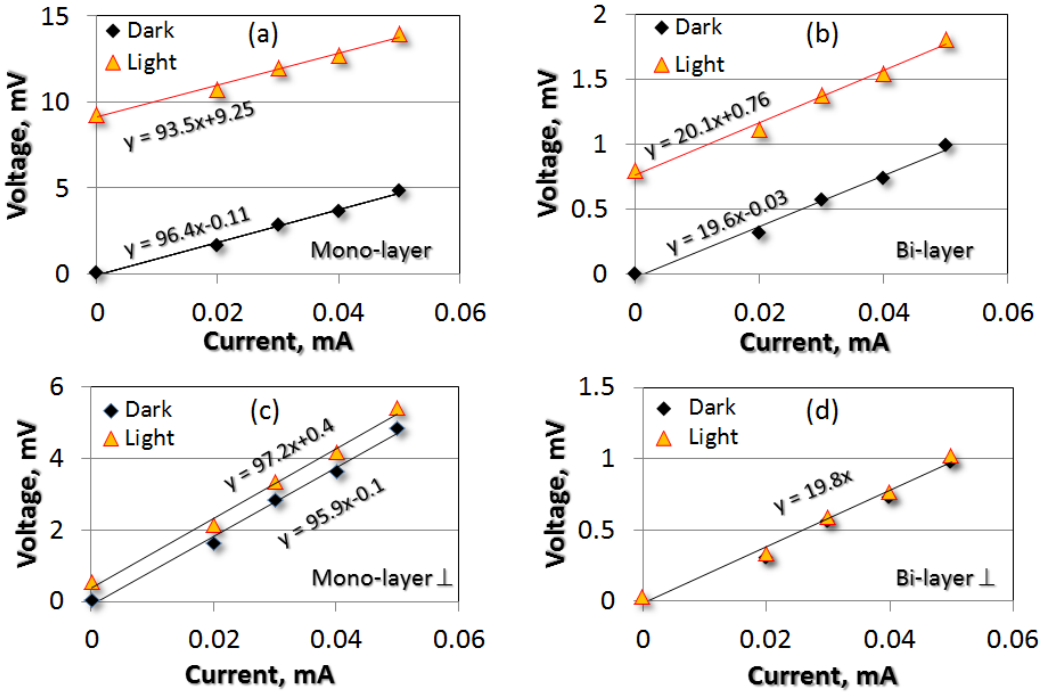

Figure 7.2. I-V characteristics under dark and 1.2 milli-Watts illumination for (a) mono-layer and (b) bi-layer MoS_2 devices. The corresponding values, when measured with electrodes at perpendicular (⊥) direction in (c) monolayer and (d) bilayer devices exhibit remarkable anisotropy in photo-sensitivity. Predominant nature of ohmic contact is seen for all the devices.

A remarkable feature of this study is the apparent ohmic nature of the electrical contacts, as shown in Figure 7.2. Almost all existing photo-detector devices in the literature [119, 312-314, 320-322] present Schottky type contact and the choice of electrode work function is very critical in

2D devices to obtain ohmic contacts. Desired features of the contact are (i) small lattice mismatch at the interface (ii) maximized overlap between the density of states (DOS) at both sides of the interface, (iii) large DOS at the Fermi level throughout the interface region to form delocalized states with low effective electron mass in order to efficiently transfer electrons between the metal and the semiconductor, (iv) a minimized potential barrier at the interface to maximize current injection [323]. Our choice of metals for the electrical contacts therefore appears to be satisfying these conditions. While it is expected that the direct band gap will enhance the photon absorption, formation of an electrical bias through predominantly ohmic contact as seen in Figure 7.2 is unprecedented. One way to view the observed phenomenon could be the negative-photoconductivity (increase in resistivity under photo-excitation) effect. Essentially, the resistivity of the mono and bilayer specimens increased to 3.5 and 1.1 times respectively under illumination. This is contrary to the conventional observation where light induced charge generation actually increases conductivity. This clearly indicates that the generated charge has been isolated and trapped at the electrodes. To achieve negative photo-conductivity, either a hetero-structure to accept and trap the charge [324-327] or surface plasmon resonance [328] is needed. Both these mechanisms may be partially responsible. For example, if the MoS_2 specimen is terminated with a Mo layer, it can transport the generated charge to trap it in the oxide substrate of the 2D layers. The obtained experimental results therefore suggest a mechanism for maintaining a potential gradient or asymmetry. While a photo-thermo-electric mechanism has been proposed [309] to be an alternative for conventional Schottky barriers, this is not the case for our study. To prove this, we have varied the location of the light source (along the plane perpendicular to the distance between the source and specimen) and observed that the maximum photo-voltage occurs when the light source is about 45° angles inclined to the vertical. Since this is not the smallest distance from the specimen, we also do not expect this to provide highest photo-thermal energy.

To explain the anomalous observation of photo-voltaic effect, we closely examine the giant photovoltaic (voltages many times larger than the potential drop across the energy gap) effects in thin semiconducting films. The early literature [329] indicates occurrence of this intriguing phenomenon in many materials, however the inconsistency in experimental results has contributed to the lack of understanding and technological relevance. Nevertheless, a consistent observation is that an electro-motive potential gradient (the end closer to the source shows negative polarity) is seen in semiconducting thin films when the insulating substrate is inclined with respect to the incident deposition flux. This is exactly same as our deposition configuration as shown in Figure 7.1a. Interestingly, this specific condition is impossible to achieve in the conventional techniques (exfoliation, chemical vapour deposition). It is hypothesized that the oblique deposition creates nanoscale p-n junctions due to stacking fault, domain boundaries (Figure 7.1b suggests turbostratic structure of the films) or the Dember effect [329].

A counter-argument could be that even though the I-V profile is linear and no rectifying junction was intentionally fabricated in the devices, there could be Schottky barriers due to the work function of the Ti electrode [330] or through the localized doping of the MoS_2 (similar to graphene induced doping [331]). If this were the case, the effect would be the same for all of the four electrodes and there would not be any anisotropic behaviour observed. At the same time, if the fundamental mechanism indeed involves the oblique deposition of the MoS_2, we would observe large potential between the ends closest and farthest to the deposition source and minimal potential in the perpendicular direction. To corroborate this hypothesis, we measured the open circuit voltage due to illumination by simply changing the electrical terminals in our van der Pauw structure. It is expected that the end of the specimen closest to the deposition source will have negative while the farthest end will have positive polarity. The two other ends that are equidistant to the deposition source should have the same potential and thus will not show any photo-voltaic effect. Or in other words, the observed photovoltaic effects should be highly anisotropic. As shown in Figures 7.2c and 2d, this is indeed the case. This evidence corroborates our hypothesis since the MoS_2 layers are not expected to show in-plane electrical anisotropy of such large magnitude. The literature contains evidence of thermal anisotropy in 2D MoS_2 [332], where the degree of anisotropy is around 0.8.

We further characterized the monolayer based devices by controlling the illumination through an aperture and exposing only the electrical contact areas. This is commonly observed in 2D opto-electronic devices [119, 309, 314]. Unfortunately, we were not able to accurately measure the effective area for illumination. According to the literature, the photo-current decays about 2 microns away from the electrical contact. If we conservatively estimate this decay length to be 5 microns, the effective illumination area for the approximately 10 mm long edges for the four electrical contacts is about 5×10^{-8} m^2. For the illumination intensity of 24 kLux, the effective illumination power is estimated to be about 1.2×10^{-3} Watts. The highest measured steady state photo-current for the monolayer specimens is about 96.4 μA, which results in photo-responsivity of 0.08 A/W. The extrinsic quantum efficiency (η, ratio of the number of charge carriers generated to the number of incident photons) was calculated to be 0.17 using Equation 1.

$$\eta = (hc/e)(I/P\lambda) \tag{1}$$

where h is the Planck constant, c the speed of light in vacuum, and e the electron charge. The photocurrent, incident power per unit area P, and excitation wavelength are denoted by I, P and λ respectively. In an absolute sense, both photo-responsivity and quantum efficiency values are smaller compared to the MoS_2 literature. However, these quantities are typically reported for exfoliated flakes and also at micro to nano Watt levels. They nonlinearly decrease with increasing power due to screening of the built-in electric field by the excited electrons in the conduction band [119] or saturation of the trap states at the MoS_2 or MoS_2-substrate interface. For example, the highest MoS_2 photo-responsivity is about 880 A/W at 150 pico-Watts, which monotonically decreases to 2 A/W at 1 micro-Watts [314]. Similarly, quantum efficiency of about 0.2 is reported for exfoliated flakes at 20 micro-Watt power [119]. Given our conservative estimate of the illumination area and power level at milli-Watts range, extrapolation of these performance metrics to the comparable power levels in the literature is extremely encouraging for further research. Currently, we are exploring the role of temperature, carrier concentration and back-gate voltage dependence for the present study.

7.1.4 Conclusion

In conclusion, we present evidence of photo-voltaic effects in mono and bi-layer ultra-high vacuum magnetron sputtered large area MoS_2 specimens in absence of intentionally fabricated p-n junction or Schottky type contact. The photo-responsivity and extrinsic quantum efficiency were estimated to be 0.08 A/W and 0.17 respectively. We also present evidence of potential gradient in oblique deposition of ultrathin semiconducting films and propose that this gradient is instrumental in generating the photo-voltaic effect in ohmic contacts. While most of the MoS_2 opto-electronics literature is based on photo-transistors fabricated on exfoliated flakes, the extremely simple design (no need for rectifying junctions) involving large area physical vapor deposited 2D MoS_2 presented in this study can significantly impact technology development in this area.

7.2 Self-Ion Irradiation Effects on Mechanical Properties of Nanocrystalline Zr Films

Zirconium thin films were irradiated at room temperature with an 800 keV Zr^+ beam using a 6 MV HVE Tandem accelerator to 1.36 displacement per atom damage. Freestanding tensile specimens, 100 nm thick and 10 nm grain size, were tested in-situ inside a transmission electron microscope. Significant grain growth (>300%), texture evolution, and displacement damage defects were observed. Stress-strain profiles were mostly linear elastic below 20 nm grain size, but above this limit the samples demonstrated yielding and strain hardening. Experimental results support the hypothesis that grain boundaries in nanocrystalline metals act as very effective defect sinks.

7.2.1 Introduction

Radiation in nuclear applications adversely influences the microstructure of the fuel, cladding, and other component materials. Depending on the radiation fluence, flux, temperature and other environmental conditions, such influence on grain size, shape, texture, and dislocation density may inflict anisotropic dimensional change, hardening, and even amorphization [333, 334]. This is manifested with the loss of ductility and plastic instability that is known to degrade the structural performance of these materials [335]. Zirconium and its alloys have been historically popular as cladding materials because of their low thermal neutron capture cross section, high temperature, corrosion resistance and satisfactory mechanical properties. Post irradiation mechanical behavior of zirconium and Zr alloys is characterized by an increase of yield strength and hardness [336, 337], which comes at the cost of reduced ductility and fracture toughness [333].

This study is motivated by the application potentials of nanocrystalline materials, which are hypothesized to exhibit better resistance to irradiation by reducing irradiation induced dislocation and cavity density [338]. It is postulated that grain boundaries in nanocrystalline systems are effective sinks for radiation-induced defects. Since the volume fraction of grain boundary increases exponentially at <25 nm grain size, nanocrystalline materials may exhibit enhanced radiation tolerance [339]. There is also indication that radiation tolerance could be grain size dependent and strongly influenced by temperature [340]. At these grain sizes, nanocrystalline metals also show very high strength and low ductility [341]. We hypothesize that radiation induced defects are actually beneficial at this length-scale, because of the very high strength due to defect confinement and increases mobile defect density (due to irradiation) enhancing ductility. We therefore design a set of experiments where irradiation is performed on specimens with initial grain sizes around 10 nm and then measure their mechanical properties inside a TEM so that the irradiation induced microstructural changes could be connected to the deformation behavior. In particular, we employ self-ion irradiation, which is suggested to be surrogate of neutron irradiation with distinct advantages such as: (a) lower time and cost since damage rates (~10^{-2} dpa/s) are higher compared to the typical ~10^{-7} dpa/s for nuclear reactors (b) little or no residual radioactivity and (c) precise control of irradiation conditions [342]. The majority of ion irradiation studies in Zr to date have been focused on coarse grain, bulk, and alloys [343, 344]. The effect of ion irradiation for nanocrystalline zirconium is therefore yet to be completely understood.

7.2.2 Experimental Setup

To study our hypothesis that radiation induces beneficial features to nanocrystalline metals, we developed a set of experiments where uniaxial tensile tests are performed on self-ion irradiated specimens. The process starts with design and fabrication of a micro-electro-mechanical (MEMS) device. As shown in Figure 7.3a, the devices integrates electro-thermal actuators, mechanical displacement sensors with the specimen. Thin zirconium films of 99.99% purity were sputter deposited on a silicon-on insulator (SOI) wafer with 20 µm-thick device layer. The device design was then patterned on the wafer using photolithography and subsequent deep reactive ion etching on both front and backsides using techniques detailed elsewhere [60]. At this stage, the specimen is not freestanding and the two reference points (marked as B and C) on its two ends are connected. We then perform ion irradiation on the device, which has been a popular surrogate for neutron irradiation.

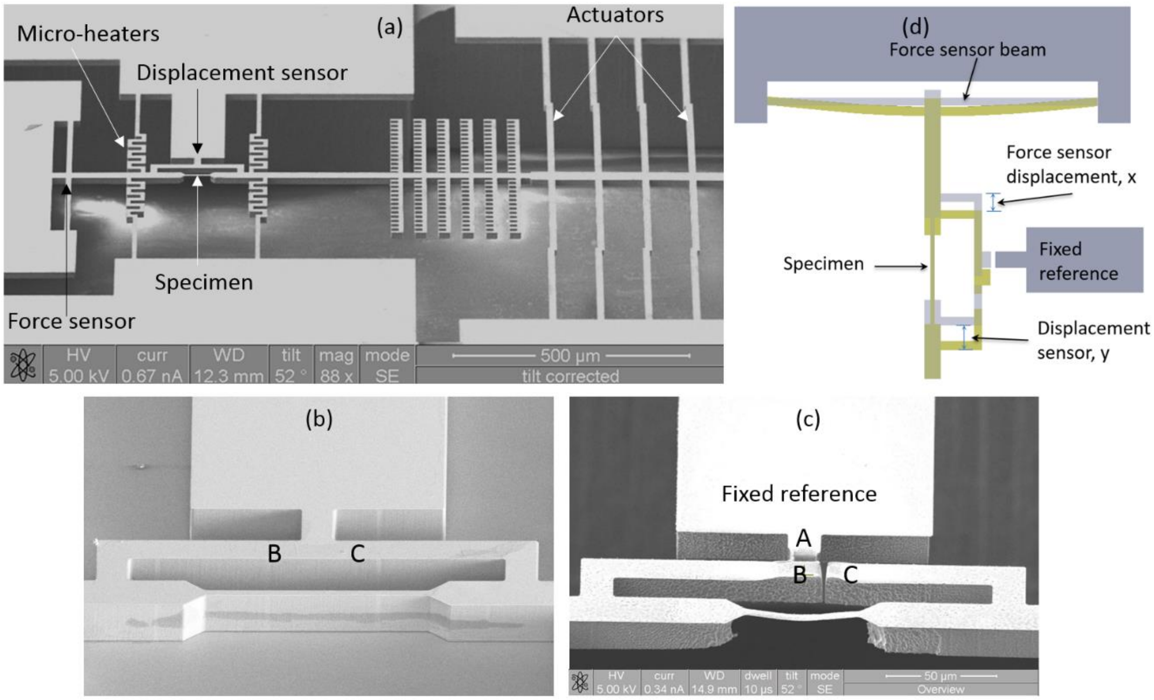
(a)
Micro-heaters
Displacement sensor
Actuators
Specimen
Force sensor
HV 5.00 kV
curr 0.67 nA
WD 12.3 mm
tilt 52 °
mag 88 x
mode SE
500 µm
tilt corrected
(d)
Force sensor beam
Force sensor displacement, x
Specimen
Fixed reference
Displacement sensor, y
(b)
B
C
(c)
Fixed reference
A
B
C
HV 5.00 kV
curr 0.34 nA
WD 14.9 mm
dwell 10 µs
tilt 52 °
mode SE
50 µm
Overview

Figure 7.3. (a) Micro-machined electromechanical device for mechanical testing of thin films (b) zoomed-in view of the specimen gauge section before ion irradiation (c) the same location after ion irradiation and subsequent substrate etching (d) schematic showing displacement and force measurement.

After the ion irradiation, the silicon substrate underneath the specimen gauge length is selectively removed using isotropic reactive ion etching. This step releases the specimen from the substrate (Figure 7.3c). The freestanding specimen remains suspended and essentially spring-loaded by the micro-machined silicon beams. We then use a focused ion beam to cut a narrow slit to separate the two ends of the specimen frame (marked as B and C). Similarly, we separate the two points (marked as A and B) so that the displacements of the left and right ends of the specimens can be measured by comparing the motion of the points B and C respectively from the immobile location A. In a typical experiment, the 3 mm x 5 mm footprint device is mounted on a commercially available TEM holder for in-situ electrical biasing. The actuation imposes a displacement to the silicon structures, which is transmitted through the specimen. The displacement on the left side of the specimen is taken by the force sensing. This displacement (x, in Figure 7.3b) gives the force on the specimen when multiplied by the spring constant of the silicon beams. The displacement at the right side of the specimen (y) is the rigid body motion of the actuators. The difference between these two displacements (y-x) is the specimen elongation. Figure 7.3d shows the displacement measurement schemes. These displacements are measured inside the TEM, which makes the measurements slow, but robust and accurate. We achieve about 50 nm displacement resolution in our in-situ TEM experiments, which gives at least 0.1% strain resolution for a nominally 50 µm-long specimen.

7.2.3 Results and Discussion

Individual dies containing multiple partially processed microfabricated samples were ion irradiated with an 800 keV Zr^+ beam using the 6 MV HVE Tandem accelerator at Sandia's Ion Beam Lab. The ion energy was chosen based on a Stopping and Range of Ions in Matter (SRIM) simulations [345] (Figure 7.4) to have a relatively uniform damage profile. The six doses achieved were: $3x10^{10}$ ions/cm^2, $3x10^{11}$ ions/cm^2, $3x10^{12}$ ions/cm^2, $3x10^{13}$ ions/cm^2, $3x10^{14}$ ions/cm^2 and $3.26x10^{14}$ ions/cm^2. Irradiation damage in Zr/Si specimen by 800 keV Zr ions was calculated using SRIM-2013 with full damage cascades and the displacement energy of 40 eV, typical for metals.

Damage level in term of displacement per atom can be calculated as:

$$dpa = \frac{\emptyset \times 10^{8} \times Damage\ rate}{N} \tag{1}$$

where $\emptyset$ is the fluence in ions/cm^2. The damage rate expressed in vacancies/ion/A° is obtained from SRIM. From Figure 7.4, we used an average damage rate of 1.8 vacancies/ion/A° was used in the calculation, and N is the atomic number density 4.28x10^{22} atoms/cm^3. It is predicted using SRIM that this ion irradiation conditions will result in damage levels in the 100 nm-thick Zr film of 1.26^{-04}, 1.26^{-03}, 1.26^{-02}, 1.26^{-01}, 1.26 and 1.37 dpa (peak value through the Zr thickness) respectively.

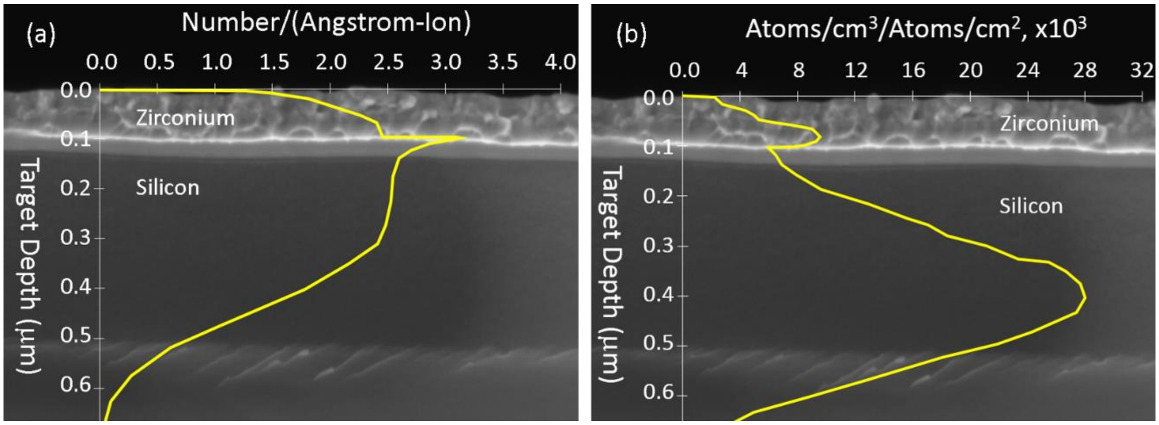

Figure 7.4. SRIM simulation of (a) collision events and (b) ion ranges in 100 nm thick zirconium thin films on silicon substrate irradiated with 800 keV Zr$^+$ ions. The plots are super-imposed on an SEM image of the specimen before the silicon layer is etched away.

After irradiation, the silicon substrate beneath the specimen is etched away using reaction ions of SF$_6$ and O$_2$. At least three specimens of each irradiation dosage were first investigated for microstructural changes and then tested for uniaxial stress-strain behavior. All the experiments were performed at room temperature.

Irradiation Effects on Microstructure: Figure 7.5 shows bright-field TEM images of the specimens as function of the radiation dosage and associated damage level. Grain growth was prominent for all doses, which is consistent across the literature [340, 346, 347]. Ion-irradiation induced grain growth exhibits three regimes (i) a purely thermal regime, (ii) a thermally-assisted regime where thermal motion and irradiation effects combine to increase the rate of grain growth and (iii) a low temperature regime, where ballistic (direct collisional impacts) effects at the grain boundaries dominate the grain growth process [347]. Defect-driven models are therefore more appropriate for this study [348], where the high concentration of irradiation-induced defects caused by collision cascades would pronounce atomic diffusion and mobility at the grain boundaries. This is enhanced below the 10 nm scale.

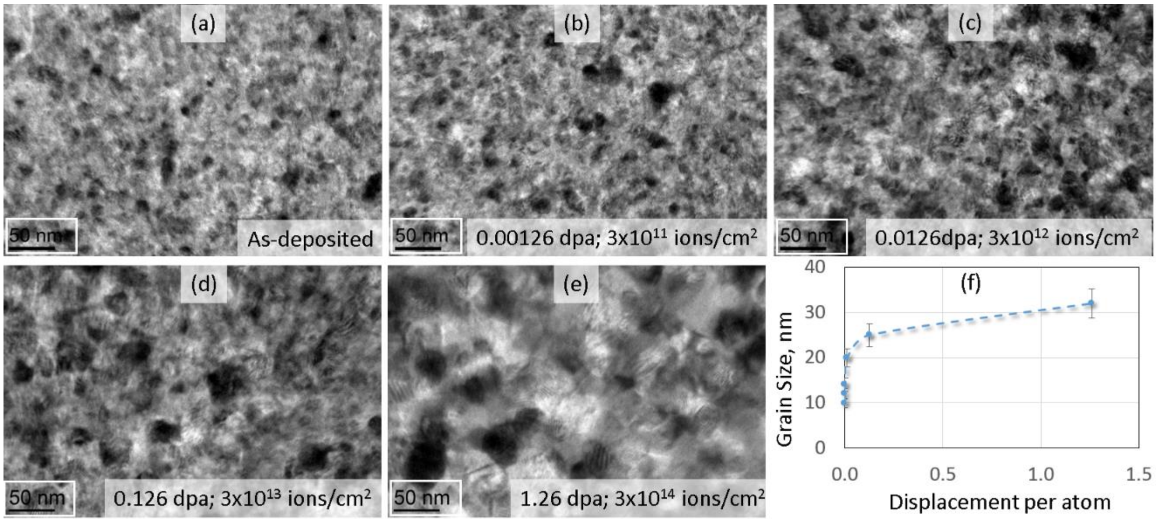
(a)
50 nm
As-deposited
(b)
50 nm
0.00126 dpa; 3x10¹¹ ions/cm²
(c)
50 nm
0.0126dpa; 3x10¹² ions/cm²
(d)
50 nm
0.126 dpa; 3x10¹³ ions/cm²
(e)
50 nm
1.26 dpa; 3x10¹⁴ ions/cm²
(f)
Grain Size, nm
0
10
20
30
40
0.0
0.5
1.0
1.5
Displacement per atom

Figure 7.5. (a-e) TEM images of the specimens after various levels of irradiation damage, (f) increase in measured grain size from the 10 nm as-deposited value as function of irradiation damage.

In addition to grain growth, irradiation leads to texture development as shown in Figure 7.6. The selected area electron diffraction (SAD) patterns becomes discontinuous or spotty (reflecting grain growth) and the rings associated with various crystallographic planes appear or disappear, suggesting changes in composition or texture. For example, the [105] and [222] planes become weak or invisible, while the [82] plane becomes prominent. From the diffraction patterns, we measured the inter-atomic spacing of these planes, which shows strain fields generated, resembling anisotropic diffusion driven growth in absence of any external mechanical loading. Figure 7.6 also shows oxidation of zirconium (at about 0.126 and 1.26 dpa), where an additional ring representing the [24] plane in ZrO_2 was clearly visible. This can be explained by the formation of an oxide originating from trace oxygen in the ion beam line during ion irradiation. Such oxide has been shown to impede defect mobility during annealing in nanocrystalline Ni [349].

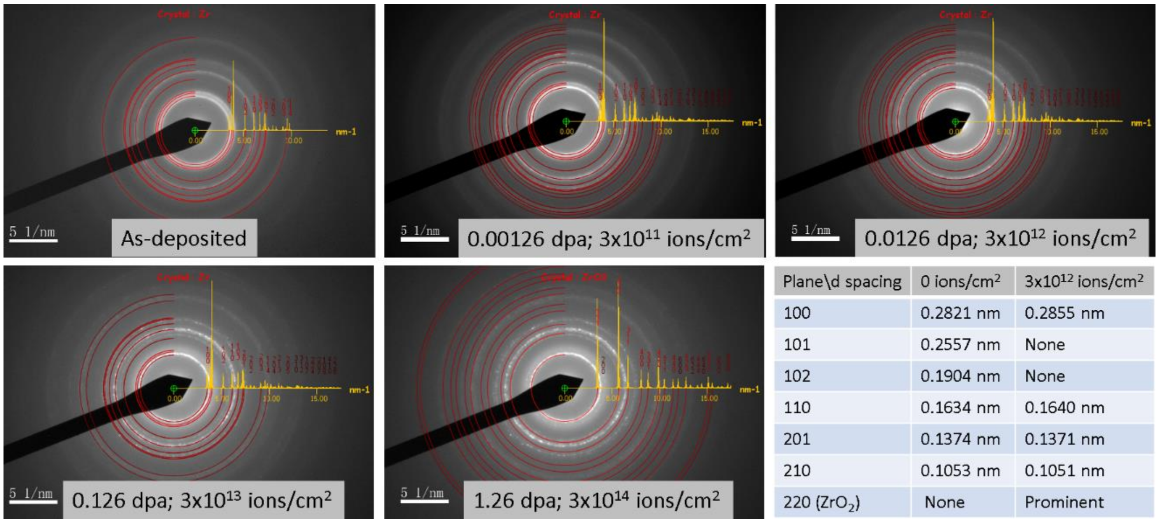
5 1/nm
As-deposited
5 1/nm
0.00126 dpa; 3x10¹¹ ions/cm²
5 1/nm
0.0126 dpa; 3x10¹² ions/cm²
5 1/nm
0.126 dpa; 3x10¹³ ions/cm²
5 1/nm
1.26 dpa; 3x10¹⁴ ions/cm²
nm-1

Plane\d spacing	0 ions/cm^2	3x10^{12} ions/cm^2
100	0.2821 nm	0.2855 nm
101	0.2557 nm	None
102	0.1904 nm	None
110	0.1634 nm	0.1640 nm
201	0.1374 nm	0.1371 nm
210	0.1053 nm	0.1051 nm
220 (ZrO_2)	None	Prominent

Figure 7.6. Select area electron diffraction patterns of the specimens at various irradiation dosage.

Irradiation Effects on Mechanical Properties: Uniaxial tensile tests performed on the irradiated specimens showed strong influence on both elastic and plastic properties. The as-deposited specimens showed no visible plastic deformation mechanisms and the stress-strain diagram was linear elastic up to failure. This is typical for nanocrystalline metals with grain sizes smaller than the cross-over size, d_c [1]. Here the grain is too small to accommodate any significant dislocation activity, as such the grains are typically referred to as dislocation starved. For higher doses, vacancy clusters are thought to agglomerate into dislocation loops. Irradiation in nanocrystals therefore add plastic deformation mechanisms. Figure 7.7 shows about 100% increase in ductility without any loss in strength in the sample irradiated to 1.26 dpa in comparison to the pristine sample.

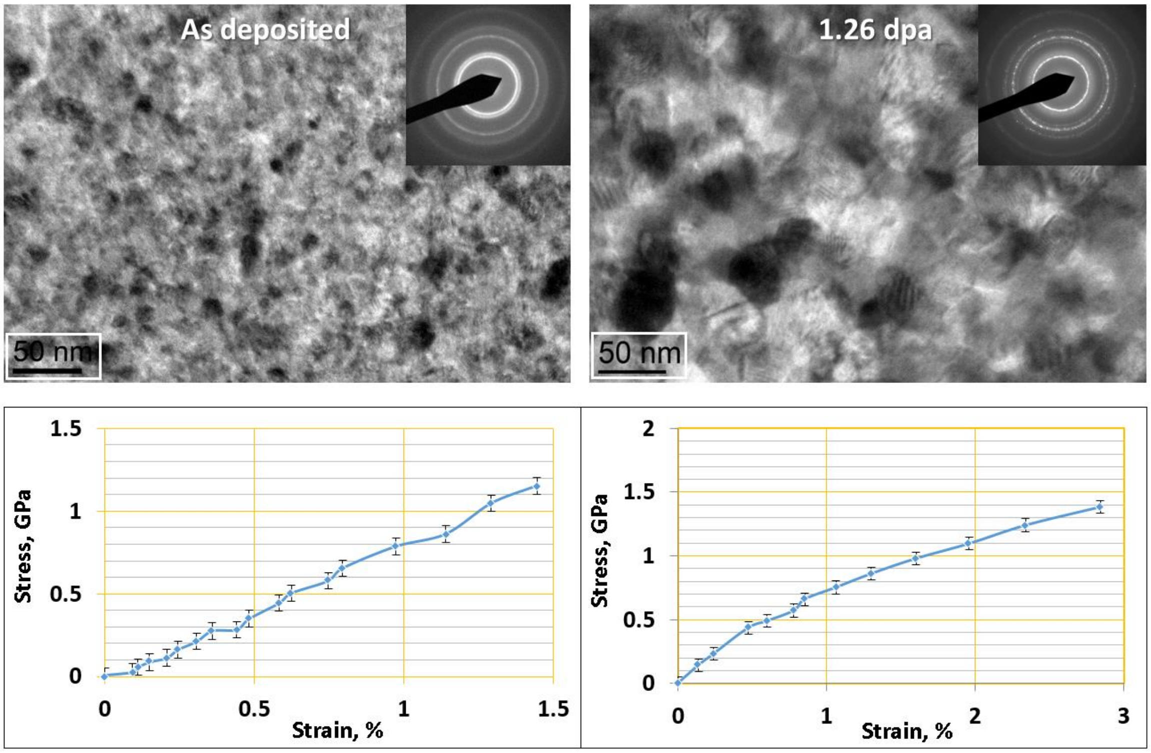

Figure 7.7. Effect of self-ion irradiation driven microstructural changes on the mechanical properties of nanocrystalline zirconium thin films.

Experimental results on elastic and plastic properties of self-ion irradiated zirconium thin films are shown in Figure 7.8. For grain sizes below 20 nm, the volume fractions of grain boundary and triple junction are significantly larger than bulk and also strong functions of the grain size. The abundance of these defect sinks and increased atomic disorder due to irradiation reduces the Young's modulus for very small grain sizes. However, radiation also results in grain size increase as shown by the inset of Figure 7.8a. The increase of grain size implies that the volume fraction of grain boundaries is not predominant. Figure 7.8a suggests that the influence role of irradiation on the moduli is negligible for grain sizes greater than about 20 nm. Above this grain size, the fraction of grain boundary atoms falls below 10% [350], which nullifies the sensitivity of the non-equilibrium grain boundary structure. Above 20 nm grain size (0.126 dpa), we observe the familiar increasing trend. Interestingly, this is also the grain size where we start observing plastic deformation in the specimens. As shown in Figure 7.8b, both ultimate stress and strain increase in samples exposed to higher doses. Therefore, the role of irradiation damage is two-fold, (a) increase the grain size and (b) supply additional defects in the previously the dislocation starved grains with mechanisms for plasticity. However, the maximum grain size in this study is too small compared to bulk to accommodate large densities of dislocations, so that the ultimate strain is still below 5%.

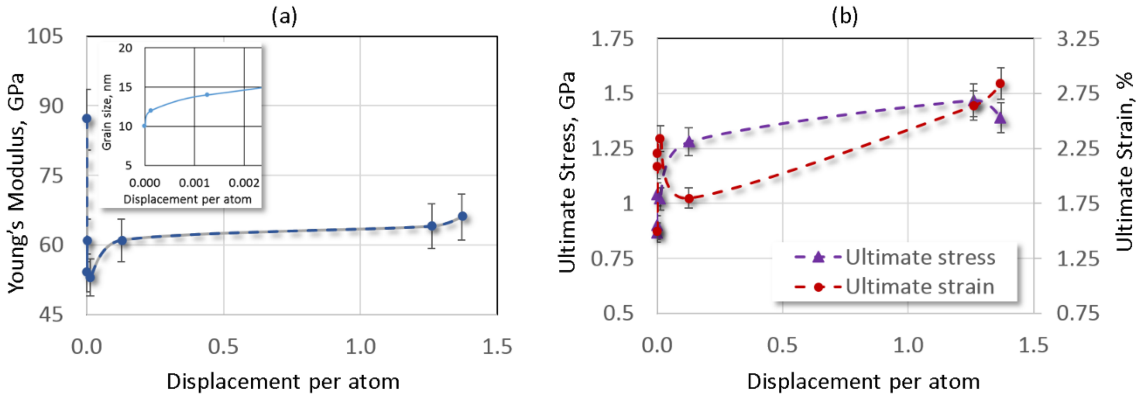

Figure 7.8. Effect of self-ion-irradiation on (a) Young's modulus (inset shows the grain size as function of damage that correlates grain size with Young's modulus) and (b) strain hardening of nanocrystalline (as-deposited grain size ~10 nm) zirconium thin films.

7.2.4 Conclusion

The effect of ion irradiation on the microstructure and mechanical properties nanocrystalline zirconium was studied in-situ inside a TEM. The specimens with average grain size of about 10 nm were irradiated at room temperature with an 800 keV Zr^+ beam using a 6 MV HVE Tandem accelerator to achieve displacement per atom ranging from $2.1x10^{-4}$ to 2.28. The experimental measurements and observations lead to the following conclusions:

i. The primary effect of self-ion irradiation is to inject vacancies and their clusters in the grain boundaries of the nanocrystalline metal. The abundance of grain boundaries at the nanoscale strongly influence the evolution of microstructure (and hence properties).

ii. Below about 15 nm grain size, the Young's modulus is very sensitive to irradiation. However, a direct consequence of irradiation is grain growth, which leads to recovery of the Young's modulus at higher damage levels.

Strength and ductility are influenced by irradiation in a different manner than the bulk. Because the specimens are nanocrystalline, they exhibit very high strength but low ductility because of dislocation starvation. At the same time, the high volume fraction of grain boundaries are infused with the defects from radiation – thereby giving the plastic deformation mechanisms to increase ductility. We therefore observed sustained strain hardening, indicating improved radiation tolerance at the 10-30 nm grain size range.

References

1. Arzt, E., *Size effects in materials due to microstructural and dimensional constraints: a comparative review.* Acta Materialia, 1998. 46(16): p. 5611-5626.
2. Vinci, R.P. and J.J. Vlassak, *Mechanical Behavior of Thin Films.* Annual Review of Material Science, 1996. 26: p. 431-462.
3. Mayadas, A. and M. Shatzkes, *Electrical-resistivity model for polycrystalline films: the case of arbitrary reflection at external surfaces.* Physical Review B, 1970. 1(4): p. 1382.
4. Durkan, C. and M.E. Welland, *Size effects in the electrical resistivity of polycrystalline nanowires.* Physical Review B, 2000. 61(20): p. 14215-14218.
5. Steinhogl, W., et al., *Size-dependent resistivity of metallic wires in the mesoscopic range.* Physical Review B, 2002. 66(7).
6. Huang, Q.J., et al., *Surface and size effects on the electrical properties of Cu nanowires.* Journal of Applied Physics, 2008. 104(2).
7. Raop, M.A., et al. *CADENCE simulation studies on the effect of transistor width size on internal resistance in CMOS rectifier using two PMOS and NMOS*. in *Industrial Electronics and Applications (ISIEA), 2013 IEEE Symposium on*. 2013.
8. Seong-Jin, K., et al., *Gate-Length Dependence of Negative Differential Resistance in InGaAs/InAlAs Quantum Well Field-Effect Transistor.* Japanese Journal of Applied Physics, 2000. 39(11R): p. 6152.
9. Park, J.S., et al., *Review of recent developments in amorphous oxide semiconductor thin-film transistor devices.* Thin Solid Films, 2012. 520(6): p. 1679-1693.

10. Asheghi, M., et al., *Phonon-boundary scattering in thin silicon layers.* Applied Physics Letters, 1997. 71(13): p. 1798-1800.

11. Li, D.Y., et al., *Thermal conductivity of individual silicon nanowires.* Applied Physics Letters, 2003. 83(14): p. 2934-2936.

12. Zhong, Z. and X. Wang, *Thermal transport in nanocrystalline materials.* Journal of Applied Physics, 2006. 100(4): p. 044310.

13. Zhong, Z., X. Wang, and J. Xu, *EQUILIBRIUM MOLECULAR DYNAMICS STUDY OF PHONON THERMAL TRANSPORT IN NANOMATERIALS.* Numerical Heat Transfer, Part B: Fundamentals, 2004. 46(5): p. 429-446.

14. Chang, Y.A. and L. Himmel, *Temperature Dependence of the Elastic Constants of Cu, Ag, and Au above Room Temperature.* Journal of Applied Physics, 1966. 37(9): p. 3567-3572.

15. Shigeki, N., et al., *Mechanical properties of a micron-sized SCS film in a high-temperature environment.* Journal of Micromechanics and Microengineering, 2006. 16(4): p. 715.

16. Park, K.-I., et al., *HIGH TEMPERATURE MECHANICAL PROPERTIES OF CVD-SiC THIN FILMS.* Modern Physics Letters B, 2009. 23(31n32): p. 3877-3886.

17. Li, X., et al., *Strain effects on the thermal conductivity of nanostructures.* Physical Review B, 2010. 81(24): p. 245318.

18. Kuczynski, G.C., *Effect of Elastic Strain on the Electrical Resistance of Metals.* Physical Review, 1954. 94(1): p. 61-64.

19. Lai, M.Z., P.S. Lee, and A. Agarwal, *Thermal effects on LPCVD amorphous silicon.* Thin Solid Films, 2006. 504(1–2): p. 145-148.

20. Dong Kim, B., et al., *Solid phase crystallization of amorphous silicon on glass by thin film heater for thin film transistor (TFT) application.* Microelectronics Journal, 2003. 34(9): p. 767-771.

21. Park, C.-D., et al., *Solid-phase crystallization of hydrogenated amorphous silicon/hydrogenated microcrystalline silicon bilayers deposited by plasma-enhanced chemical vapor deposition.* Thin Solid Films, 2000. 359(2): p. 268-274.

22. Meng, F.Q., K. Tsuchiya, and Y. Yokoyama, *Crystalline to amorphous transformation in Zr–Cu–Al alloys induced by high pressure torsion.* Intermetallics, 2013. 37(0): p. 52-58.

23. Law, M., J. Goldberger, and P.D. Yang, *Semiconductor nanowires and nanotubes.* Annual Review of Materials Research, 2004. 34: p. 83-122.

24. Bhowmick, S. and V.B. Shenoy, *Effect of strain on the thermal conductivity of solids.* Journal of Chemical Physics, 2006. 125(16).

25. Ghosh, R., D. Basak, and S. Fujihara, *Effect of substrate-induced strain on the structural, electrical, and optical properties of polycrystalline ZnO thin films.* Journal of Applied Physics, 2004. 96(5): p. 2689-2692.

26. Lee, H.F., S. Kumar, and M.A. Haque, *Role of mechanical strain on thermal conductivity of nanoscale aluminum films.* Acta Materialia, 2010. 58(20): p. 6619-6627.

27. Li, X.B., et al., *Strain effects on the thermal conductivity of nanostructures.* Physical Review B, 2010. 81(24).

28. Yong, Z., C. Alberto, and D.E. Horacio, *A thermal actuator for nanoscale in situ microscopy testing: design and characterization.* Journal of Micromechanics and Microengineering, 2006. 16(2): p. 242.

29. Ismail, K., et al., *Electron transport properties of Si/SiGe heterostructures: Measurements and device implications.* Applied Physics Letters, 1993. 63(5): p. 660-662.

30. Xie, Y.H., et al., *Molecular Beam Epitaxial Growth of Very High Mobility Two-Dimensional Electron Gases in Si/GeSi Heterostructures.* MRS Online Proceedings Library, 1991. 220: p. null-null.

31. Vogelsang, T. and K.R. Hofmann, *Electron mobilities and high-field drift velocities in strained silicon on silicon-germanium substrates*. Electron Devices, IEEE Transactions on, 1992. 39(11): p. 2641-2642.

32. Stier, O., M. Grundmann, and D. Bimberg, *Electronic and optical properties of strained quantum dots modeled by 8-band k·p theory*. Physical Review B, 1999. 59(8): p. 5688-5701.

33. Suzuki, M. and T. Uenoyama, *Strain effect on electronic and optical properties of GaN/AlGaN quantum-well lasers*. Journal of Applied Physics, 1996. 80(12): p. 6868-6874.

34. Kim, S.Y. and H.S. Park, *Utilizing Mechanical Strain to Mitigate the Intrinsic Loss Mechanisms in Oscillating Metal Nanowires.* Physical Review Letters, 2008. 101(21): p. 215502.

35. Meng, J.F., et al., *Multifold enhancement of the thermoelectric figure of merit in p-type BaBiTe3 by pressure tuning.* Journal of Applied Physics, 2001. 90(6): p. 2836-2839.

36. Polvani, D.A., et al., *Large Improvement in Thermoelectric Properties in Pressure-Tuned p-Type Sb1.5Bi0.5Te3.* Chemistry of Materials, 2001. 13(6): p. 2068-2071.

37. Banerjee, S., et al., *Natural convection in a bi-heater configuration of passive electronic cooling*. International Journal of Thermal Sciences, 2008. 47(11): p. 1516-1527.

38. Shi, Y., et al., *Tailoring grain size distribution for optimizing strength and ductility of multi-modal Zr*. Materials Letters, 2013. 108(0): p. 228-230.

39. Kumar, S., M.T. Alam, and M.A. Haque, *Fatigue Insensitivity of Nanoscale Freestanding Aluminum Films.* Journal of Microelectromechanical Systems, 2011. 20(1): p. 53-58.

40. Tabachnikova, E.D., et al., *Mechanical properties of ultrafine-grain zirconium in the temperature range 4.2-300 K.* Low Temperature Physics, 2008. 34: p. 969-975.

41. Kad, B.K., et al., *Ultrafine-grain-sized zirconium by dynamic deformation.* Acta Materialia, 2006. 54(16): p. 4111-4127.

42. Yuan, C., et al., *The tensile properties and fracture behavior of gradient nano-grained/coarse-grained zirconium.* Materials Letters, 2013. 107(0): p. 134-137.

43. Guo, D., et al., *Simultaneously enhancing the ductility and strength of cryorolled Zr via tailoring dislocation configurations.* Materials Science and Engineering: A, 2012. 558(0): p. 611-615.

44. Guo, D., et al., *High strength and ductility in multimodal-structured Zr.* Materials & Design, 2012. 34(0): p. 275-278.

45. Zhang, J.Y., et al., *Deformation crossover in nanocrystalline Zr micropillars: The strongest external size.* Scripta Materialia, 2013. 68(8): p. 639-642.

46. Liu, M.C., et al., *A nanoscaled underlayer confinement approach for achieving extraordinarily plastic amorphous thin film.* Scripta Materialia, 2009. 61(8): p. 840-843.

47. Shu, B.P., et al., *Deformation twinning and detwinning in the lamella copper observed by in-situ TEM.* Materials Letters, 2013. 106(0): p. 225-228.

48. Kumar, S., T. Alam, and A. Haque, *Quantitative in-situ TEM study of stress-assisted grain growth.* MRS Communications, 2013. 3(02): p. 101-105.

49. Mohan Prasad, M., et al., *Room temperature amorphous to nanocrystalline transformation in ultra-thin films under tensile stress: an in situ TEM study.* Nanotechnology, 2010. 21(50): p. 505707(1-6).

50. Manoharan, M.P., et al., *Elastic Properties of 4-6 nm-thick Glassy Carbon Thin Films.* Nanoscale Research Letters, 2010. 5(1): p. 14-19.

51. Wang, B., V. Tomar, and A. Haque, *In-situ TEM mechanical testing of nanocrystalline zirconium thin films.* Materials Letters, 2015. 152: p. 105-108.

52. Carlton, C.E. and P.J. Ferreira, *What is behind the inverse Hall–Petch effect in nanocrystalline materials?* Acta Materialia, 2007. 55(11): p. 3749-3756.

53. Luo, J.K., et al., *Young's modulus of electroplated Ni thin film for MEMS applications.* Materials Letters, 2004. 58(17–18): p. 2306-2309.

54. Bergers, L.I.J.C., et al., *Measuring time-dependent deformations in metallic MEMS.* Microelectronics Reliability, 2011. 51(6): p. 1054-1059.

55. Nowick, A.S. and B.S. Berry, *Anelastic Relaxation in Crystalline Solids*. 1972: Academic Press.

56. Guisbiers, G., et al., *Study of creep/relaxation mechanisms in thin freestanding nanocrystalline palladium films through the lab-on-chip technology.* Journal of Applied Physics, 2013. 113(2): p. 024513-6.

57. Trusov, L.I., et al., *Low temperature stress relaxation of nanocrystalline nickel.* Journal of Materials Science, 1995. 30(11): p. 2956-2961.

58. Choi, I.-C., et al., *Nanoscale room temperature creep of nanocrystalline nickel pillars at low stresses.* International Journal of Plasticity, 2013. 41(0): p. 53-64.

59. Samuel, B.A. and M.A. Haque, *Room temperature relaxation of freestanding nanocrystalline gold films.* Journal of Micromechanics and Microengineering, 2006. 16(5): p. 929-934.

60. Kumar, S. and M.A. Haque, *Fracture Testing of Nanoscale Thin Films Inside the Transmission Electron Microscope.* International Journal of Applied Mechanics, 2010. 2(4): p. 745-758.

61. Wang, B. and M.A. Haque, *Low temperature viscoelasticity in nanocrystalline nickel films.* Materials Letters, 2014. 118: p. 59-61.

62. Egan, J., *A new look at linear visco-elasticity*. Materials Letters, 1997. 31(3–6): p. 351-357.

63. Kê, T.i.-S., *Experimental Evidence of the Viscous Behavior of Grain Boundaries in Metals.* Physical Review, 1947. 71(8): p. 533-546.

64. Kolobov, I.U.R. and Y.R. Kolobov, *Grain Boundary Diffusion and Properties of Nanostructured Materials*. 2007: Cambridge International Science Pub.

65. Horváth, J., R. Birringer, and H. Gleiter, *Diffusion in nanocrystalline material.* Solid State Communications, 1987. 62(5): p. 319-322.

66. DeVoe, D.L., *Thermal issues in MEMS and microscale systems.* Components and Packaging Technologies, IEEE Transactions on, 2002. 25(4): p. 576-583.

67. Mahajan, R., C. Chia-pin, and G. Chrysler, *Cooling a Microprocessor Chip.* Proceedings of the IEEE, 2006. 94(8): p. 1476-1486.

68. Long, J., et al., *Thermal monitoring mechanisms for chip multiprocessors.* ACM Trans. Archit. Code Optim., 2008. 5(2): p. 1-33.

69. Sinha, S. and K.E. Goodson, *Thermal conduction in sub-100&#xa0;nm transistors.* Microelectronics Journal, 2006. 37(11): p. 1148-1157.

70. Han, S., et al. *Temperature-dependent behavior of thin film by microtensile testing*. in *Electronics System-Integration Technology Conference, 2008. ESTC 2008. 2nd*. 2008.

71. Olliges, S., et al., *Thermo mechanical properties and plastic deformation of gold nanolines and gold thin films.* Materials Science and Engineering: A, 2011. 528(19–20): p. 6203-6209.

72. Sato, M. and K. Sumino, *Effect of Dislocations on the Low Temperature Thermal Conductivity in Germanium.* Journal of the Physical Society of Japan, 1974. 36(4): p. 1075-1083.

73. Wasserbäch, W., S. Abens, and S. Sahling, *Low-Temperature Thermal Conductivity and Specific Heat of Plastically Deformed High-Purity Tantalum Single Crystals.* Journal of Low Temperature Physics, 2001. 123(5-6): p. 251-274.

74. Alam, M.T., et al., *Influence of strain on thermal conductivity of silicon nitride thin films.* Journal of Micromechanics and Microengineering, 2012. 22(4): p. 045001.

75. Alam, M.T., et al., *Mechanical Strain Dependence of Thermal Transport in Amorphous Silicon Thin Films.* Nanoscale and Microscale Thermophysical Engineering, 2014: p. 1-16.

76. Ihlefeld, J.F., et al., *Room-Temperature Voltage Tunable Phonon Thermal Conductivity via Reconfigurable Interfaces in Ferroelectric Thin Films.* Nano Letters, 2015. 15(3): p. 1791-1795.

77. Wasserbach, W., *Low-Temperature Acoustic and Thermal Properties of Plastically Deformed, High-Purity Crystalline Specimens of Al, Nb and Ta.* Defect and Diffusion Forum, 2002. 203-205: p. 4.

78. Shevchenko, S.A., *Electrical conductivity of germanium with dislocation grids.* Journal of Experimental and Theoretical Physics, 1999. 88(1): p. 66-71.

79. Feng, B., Z. Li, and X. Zhang, *Prediction of size effect on thermal conductivity of nanoscale metallic films.* Thin Solid Films, 2009. 517(8): p. 2803-2807.

80. Hatta, I., *Thermal characteristics in a nanometer scale.* Journal of Thermal Analysis and Calorimetry, 2002. 69(3): p. 717-725.

81. Lee, H.-F., B. Samuel, and M.A. Haque, *In-plane thermal conductance measurement of one-dimensional nanostructures.* Journal of Thermal Analysis and Calorimetry, 2010. 99(2): p. 495-500.

82. Arriagada, A., E.T. Yu, and P.R. Bandaru, *Determination of thermal parameters of one-dimensional nanostructures through a thermal transient method.* Journal of Thermal Analysis and Calorimetry, 2009. 97(3): p. 1023-1026.

83. Jain, A. and K.E. Goodson, *Measurement of the Thermal Conductivity and Heat Capacity of Freestanding Shape Memory Thin Films Using the 3ω Method.* Journal of Heat Transfer, 2008. 130(10): p. 102402-102402.

84. Zhang, X., et al., *Thermal and Electrical Properties of a Suspended Nanoscale Thin Film.* International Journal of Thermophysics, 2007. 28(1): p. 33-43.

85. Gurrum, S.P., et al., *Size Effect on the Thermal Conductivity of Thin Metallic Films Investigated by Scanning Joule Expansion Microscopy*. Journal of Heat Transfer, 2008. 130(8): p. 082403-082403.

86. Berman, R., *Thermal conduction in solids*. Oxford studies in physics. 1976, Oxford [Eng.]: Clarendon Press. p.143.

87. Dames, C., et al., *Low-dimensional phonon specific heat of titanium dioxide nanotubes.* Applied Physics Letters, 2005. 87(3): p. -.

88. Zhang, Y., et al., *Phonon spectrum and specific heat of silicon nanowires.* Journal of Applied Physics, 2007. 102(10): p. -.

89. Heino, P. and E. Ristolainen, *Thermal conduction at the nanoscale in some metals by MD.* Microelectronics Journal, 2003. 34(9): p. 773-777.

90. Chantrenne, Raynaud, and Barrat, *STUDY OF PHONON HEAT TRANSFER IN METALLIC SOLIDS FROM MOLECULAR DYNAMIC SIMULATIONS.* Microscale Thermophysical Engineering, 2003. 7(2): p. 117-136.

91. Feng, B., Z.X. Li, and X. Zhang, *Role of phonon in the thermal and electrical transports in metallic nanofilms.* Journal of Applied Physics, 2009. 105(10): p. 104315.

92. Koch, C.C., *Structural nanocrystalline materials: fundamentals and applications*. 2007, Cambridge: Cambridge University Press.

93. Haque, M.A. and M.T.A. Saif, *Deformation mechanisms in free-standing nanoscale thin films: A quantitative in situ transmission electron microscope study.* Proceedings of the National Academy of Sciences of the United States of America, 2004. 101(17): p. 6335-6340.

94. Haque, M.A. and M.T.A. Saif, *In situ Tensile Testing of Nanoscale Freestanding Thin Films Inside a Transmission Electron Microscope.* Journal of Materials Research, 2005. 20(07): p. 1769-1777.

95. Romanov, A.E., *Continuum theory of defects in nanoscaled materials.* Nanostructured Materials, 1995. 6(1–4): p. 125-134.

96. Gryaznov, V.G., et al., *Size effects of dislocation stability in nanocrystals.* Physical Review B, 1991. 44(1): p. 42-46.

97. Scattergood, R.O. and C.C. Koch, *A modified model for hall-petch behavior in nanocrystalline materials.* Scripta Metallurgica et Materialia, 1992. 27(9): p. 1195-1200.

98. Hahn, H., P. Mondal, and K.A. Padmanabhan, *Plastic deformation of nanocrystalline materials.* Nanostructured Materials, 1997. 9(1–8): p. 603-606.

99. Witney, A.B., et al., *Fatigue of nanocrystalline copper.* Scripta Metallurgica et Materialia, 1995. 33(12): p. 2025-2030.

100. Nieman, G.W., J.R. Weertman, and R.W. Siegel, *Mechanical behavior of nanocrystalline Cu and Pd.* Journal of Materials Research, 1991. 6(05): p. 1012-1027.

101. Manoharan, M., et al., *Elastic Properties of 4-6 nm-thick Glassy Carbon Thin Films.* Nanoscale Research Letters, 2009. 5(1): p. 14 - 19.

102. Haque, M.A., H.D. Espinosa, and H.J. Lee, *MEMS for In Situ Testing—Handling, Actuation, Loading, and Displacement Measurements.* MRS Bulletin, 2010. 35(05): p. 375-381.

103. Alam, M.T., et al., *Thermal conductivity of ultra-thin chemical vapor deposited hexagonal boron nitride films.* Applied Physics Letters, 2014. 104(1): p. -.

104. Bradshaw, F.J., *The Optical Emissivity of Titanium and Zirconium.* Proceedings of the Physical Society. Section B, 1950. 63(8): p. 573.

105. Alam, M.T., et al., *Structural size and temperature dependence of solid to air heat transfer.* International Journal of Thermal Sciences, 2013. 73(0): p. 1-7.

106. Wang, B., R. Pulavarthy, and M.A. Haque, *Grain size-induced thermo-mechanical coupling in zirconium thin films.* Journal of Thermal Analysis and Calorimetry, 2016. 123(2): p. 1197-1204.

107. Fink, J.K. and L. Leibowitz, *Thermal conductivity of zirconium.* Journal of Nuclear Materials, 1995. 226(1–2): p. 44-50.

108. Takahashi, Y., M. Yamawaki, and K. Yamamoto, *Thermophysical properties of uranium-zirconium alloys.* Journal of Nuclear Materials, 1988. 154(1): p. 141-144.

109. Zhang, X.Y., *Understanding corrosion resistance of nanocrystalline materials: electrochemical influences*, in *Corrosion Protection and Control Using Nanomaterials*, V.S. Saji and R.M. Cook, Editors. 2012, Elsevier Science: Cambridge, UK. p. 34-58.

110. Chang, T.-H. and Y. Zhu, *A microelectromechanical system for thermomechanical testing of nanostructures.* Applied Physics Letters, 2013. 103(26): p. 263114.

111. Haque, M.A. and M.T.A. Saif, *Thermo-mechanical properties of nano-scale freestanding aluminum films.* Thin Solid Films, 2005. 484(1-2): p. 364-368.

112. Simões, S., et al., *In situ TEM study of grain growth in nanocrystalline copper thin films.* Nanotechnology, 2010. 21(14): p. 145701.

113. Saka, H., et al., *In Situ Heating Transmission Electron Microscopy.* MRS Bulletin, 2008. 33(02): p. 93-100.

114. Ang, W.C., et al., *Novel development of the micro-tensile test at elevated temperature using a test structure with integrated micro-heater.* Journal of Micromechanics and Microengineering, 2012. 22(8): p. 085015.

115. Wonmo, K. and M.T.A. Saif, *A novel SiC MEMS apparatus for in situ uniaxial testing of micro/nanomaterials at high temperature.* Journal of Micromechanics and Microengineering, 2011. 21(10): p. 105017.

116. Wang, B. and M.A. Haque, *In Situ Microstructural Control and Mechanical Testing Inside the Transmission Electron Microscope at Elevated Temperatures.* JOM, 2015: p. 1-8.

117. Geim, A.K. and K.S. Novoselov, *The rise of graphene.* Nat Mater, 2007. 6(3): p. 183-191.

118. Mak, K.F., et al., *Atomically Thin MoS2: A New Direct-Gap Semiconductor.* Physical Review Letters, 2010. 105(13).

119. Britnell, L., et al., *Strong Light-Matter Interactions in Heterostructures of Atomically Thin Films.* Science, 2013. 340(6138): p. 1311-1314.

120. RadisavljevicB, et al., *Single-layer MoS2 transistors.* Nat Nano, 2011. 6(3): p. 147-150.

121. Yoon, Y., K. Ganapathi, and S. Salahuddin, *How Good Can Monolayer MoS2 Transistors Be?* Nano Letters, 2011. 11(9): p. 3768-3773.

122. Wang, Q.H., et al., *Electronics and optoelectronics of two-dimensional transition metal dichalcogenides.* Nat Nano, 2012. 7(11): p. 699-712.

123. Jo, I., et al., *Thermal conductivity and phonon transport in suspended few-layer hexagonal boron nitride.* Nano letters, 2013. 13(2): p. 550-554.

124. Geim, A.K. and I.V. Grigorieva, *Van der Waals heterostructures.* Nature, 2013. 499(7459): p. 419-425.

125. Novoselov, K.S. and A.H.C. Neto, *Two-dimensional crystals-based heterostructures: materials with tailored properties.* Physica Scripta, 2012. 2012(T146): p. 014006.

126. Gao, G., et al., *Artificially Stacked Atomic Layers: Toward New van der Waals Solids.* Nano Letters, 2012. 12(7): p. 3518-3525.

127. Lin, Y.-C., et al., *Direct Synthesis of van der Waals Solids.* ACS Nano, 2014. 8(4): p. 3715-3723.

128. Najmaei, S., et al., *Vapour phase growth and grain boundary structure of molybdenum disulphide atomic layers.* Nat Mater, 2013. 12(8): p. 754-759.

129. van der Zande, A.M., et al., *Grains and grain boundaries in highly crystalline monolayer molybdenum disulphide.* Nat Mater, 2013. 12(6): p. 554-561.

130. Lee, Y.-H., et al., *Synthesis of Large-Area MoS2 Atomic Layers with Chemical Vapor Deposition.* Advanced Materials, 2012. 24(17): p. 2320-2325.

131. Li, H., et al., *From Bulk to Monolayer MoS2: Evolution of Raman Scattering.* Advanced Functional Materials, 2012. 22(7): p. 1385-1390.

132. Liu, K.-K., et al., *Growth of Large-Area and Highly Crystalline MoS2 Thin Layers on Insulating Substrates.* Nano Letters, 2012. 12(3): p. 1538-1544.

133. Yu, Q., et al., *Control and characterization of individual grains and grain boundaries in graphene grown by chemical vapour deposition.* Nat Mater, 2011. 10(6): p. 443-449.

134. Ovidko, I., *Review on grain boundaries in graphene. Curved poly-and nanocrystalline graphene structures as new carbon allotropes.* Rev. Adv. Mater. Sci, 2012. 30: p. 201-224.

135. Lee, J., et al., *High-Angle Tilt Boundary Graphene Domain Recrystallized from Mobile Hot-Wire-Assisted Chemical Vapor Deposition System.* Nano Letters, 2014. 14(8): p. 4352-4359.

136. Bresnehan, M.S., et al., *Prospects of direct growth boron nitride films as substrates for graphene electronics.* Journal of Materials Research, 2014. 29(03): p. 459-471.

137. Duerloo, K.-A.N., Y. Li, and E.J. Reed, *Structural phase transitions in two-dimensional Mo- and W-dichalcogenide monolayers.* Nat Commun, 2014. 5.

138. Taniguchi, T., et al., *Phase transformation of amorphous boron nitride under high pressure.* Chemistry of Materials, 2003. 15(14): p. 2744-2751.

139. Liu, F., J. Yu, and X. Bai, *Crystallinity improvement of hexagonal boron nitride films by molybdenum catalysts during microwave plasma chemical vapor deposition and post-annealing.* Applied Surface Science, 2012. 258(24): p. 10191-10194.

140. Sutter, P., et al., *Scalable Synthesis of Uniform Few-Layer Hexagonal Boron Nitride Dielectric Films.* Nano Letters, 2012. 13(1): p. 276-281.

141. Wu, J., et al., *Layer Thinning and Etching of Mechanically Exfoliated MoS2 Nanosheets by Thermal Annealing in Air.* Small, 2013. 9(19): p. 3314-3319.

142. Muratore, C., et al., *In situ Raman spectroscopy for examination of high temperature tribological processes.* Wear, 2011. 270(3–4): p. 140-145.

143. Donarelli, M., et al., *Tunable sulfur desorption in exfoliated MoS2 by means of thermal annealing in ultra-high vacuum.* Chemical Physics Letters, 2013. 588(0): p. 198-202.

144. Ghosh, S., et al., *Simple formation of nanostructured molybdenum disulfide thin films by electrodeposition.* International Journal of Electrochemistry, 2013: p. 1-7.

145. Simões, S., et al., *In situ TEM study of grain growth in nanocrystalline copper thin films.* Nanotechnology, 2010. 21(14): p. 145701.

146. Muratore, C. and A.A. Voevodin, *Control of molybdenum disulfide basal plane orientation during coating growth in pulsed magnetron sputtering discharges.* Thin Solid Films, 2009. 517(19): p. 5605-5610.

147. Muratore, C., et al., *Continuous ultra-thin MoS2 films grown by low-temperature physical vapor deposition.* Applied Physics Letters, 2014. 104(26): p. 261604(1-6).

148. Glavin, N.R., et al., *Synthesis of few-layer, large area hexagonal-boron nitride by pulsed laser deposition.* Thin Solid Films, (0).

149. Alam, T., et al., *Domain engineering of physical vapor deposited two-dimensional materials.* Applied Physics Letters, 2014. 105(21): p. 213110.

150. Lin, Y.-C., et al., *Graphene Annealing: How Clean Can It Be?* Nano Letters, 2011. 12(1): p. 414-419.

151. Lentz, C.M., et al., *Synthesis and Characterization of Glassy Carbon Nanowires.* Journal of Nanomaterials, 2011. 2011(2011): p. 129298(1-8).

152. Loh, G.C. and D. Baillargeat, *Graphitization of amorphous carbon and its transformation pathways.* Journal of Applied Physics, 2013. 114(3).

153. Antczak, G. and G. Ehrlich, *Surface Diffusion: Metals, Metal Atoms, and Clusters*. 2010, Cambridge, UK: Cambridge University Press.

154. Greer, J.R. and J.T.M. De Hosson, *Plasticity in small-sized metallic systems: Intrinsic versus extrinsic size effect.* Progress in Materials Science, 2011. 56(6): p. 654-724.

155. Zhu, T. and J. Li, *Ultra-strength materials.* Progress in Materials Science, 2010. 55(7): p. 710-757.

156. Lian, J., et al., *Emergence of film-thickness- and grain-size-dependent elastic properties in nanocrystalline thin films.* Scripta Materialia, 2013. 68(5): p. 261-264.

157. Shan, Z.W., et al., *Grain boundary-mediated plasticity in nanocrystalline nickel.* Science, 2004. 305(5684): p. 654-657.

158. Wu, D., et al., *Grain-boundary strengthening in nanocrystalline chromium and the Hall–Petch coefficient of body-centered cubic metals.* Scripta Materialia, 2013. 68(2): p. 118-121.

159. Hanlon, T., Y.N. Kwon, and S. Suresh, *Grain size effects on the fatigue response of nanocrystalline metals.* Scripta Materialia, 2003. 49(7): p. 675-680.

160. Jang, D. and J.R. Greer, *Size-induced weakening and grain boundary-assisted deformation in 60 nm grained Ni nanopillars.* Scripta Materialia, 2011. 64(1): p. 77-80.

161. Zhu, L.L. and X.J. Zheng, *Grain-Size Dependent Thermal, Electrical and Mechanical Properties of Bulk Nanocrystalline Materials*. Bulk Materials: Research, Technology and Applications, ed. T. Frias and V. Maestas. 2010. 267-305.

162. Henriquez, R., et al., *Electron scattering at surfaces and grain boundaries in thin Au films.* Applied Surface Science, 2013. 273: p. 315-323.

163. Park, J.S., et al., *Dependence of the transport, the magnetic and the optical properties of La0.7Ca0.3MnO3-delta on grain size.* Journal of the Korean Physical Society, 2007. 51(4): p. 1564-1567.

164. Seshan, K., *Handbook of Thin Film Deposition*. 2012: Elsevier Science.

165. Thompson, C.V., *Grain-growth in Thin Films.* Annual Review of Materials Science, 1990. 20: p. 245-268.

166. Dannenberg, R., et al., *In-situ TEM observations of abnormal grain growth, coarsening, and substrate de-wetting in nanocrystalline Ag thin films.* Thin Solid Films, 2000. 370(1-2): p. 54-62.

167. Kuru, Y., et al., *Large excess volume in grain boundaries of stressed, nanocrystalline metallic thin films: Its effect on grain-growth kinetics.* Applied Physics Letters, 2009. 95(16).

168. Estrin, Y., G. Gottstein, and L.S. Shvindlerman, *Diffusion controlled creep in nanocrystalline materials under grain growth.* Scripta Materialia, 2004. 50(7): p. 993-997.

169. Barmak, K., et al., *Grain growth and the puzzle of its stagnation in thin films: The curious tale of a tail and an ear.* Progress in Materials Science, 2013. 58(7): p. 987-1055.

170. Zhang, Y., et al., *Stress-driven grain growth in ultrafine grained Mg thin film.* Scripta Materialia, 2013. 68(6): p. 424-427.

171. Prasad, M. and A.H. Chokshi, *Deformation-induced thermally activated grain growth in nanocrystalline nickel.* Scripta Materialia, 2012. 67(2): p. 133-136.

172. De Hosson, J.T., et al., *In situ TEM nanoindentation and dislocation-grain boundary interactions: a tribute to David Brandon.* Journal of materials science, 2006. 41(23): p. 7704-7719.

173. Soer, W.A., et al., *Effects of solute Mg on grain boundary and dislocation dynamics during nanoindentation of Al–Mg thin films.* Acta Materialia, 2004. 52(20): p. 5783-5790.

174. Gianola, D.S., et al., *Stress-driven surface topography evolution in nanocrystalline Al thin films.* Advanced Materials, 2008. 20(2): p. 303-+.

175. Gollapudi, S., et al., *Creep in nanocrystalline materials: Role of stress assisted grain growth.* Materials Science and Engineering a-Structural Materials Properties Microstructure and Processing, 2010. 527(21-22): p. 5773-5781.

176. Gianola, D.S., et al., *Stress-assisted discontinuous grain growth and its effect on the deformation behavior of nanocrystalline aluminum thin films.* Acta Materialia, 2006. 54(8): p. 2253-2263.

177. Xu, W.C., P.Q. Dai, and X.L. Wu, *Effect of stress-induced grain growth during room temperature tensile deformation on ductility in nanocrystalline metals.* Bulletin of Materials Science, 2010. 33(5): p. 561-568.

178. Sharon, J.A., et al., *Stress-driven grain growth in nanocrystalline Pt thin films.* Scripta Materialia, 2011. 64(1): p. 25-28.

179. Cahn, J.W., Y. Mishin, and A. Suzuki, *Coupling grain boundary motion to shear deformation.* Acta Materialia, 2006. 54(19): p. 4953-4975.

180. Li, J. and A.K. Soh, *On shear-coupled migration of grain boundaries in nanocrystalline materials.* Applied Physics Letters, 2012. 101(24): p. 241915-4.

181. Sharma, G., et al., *High temperature mechanical behavior of nanocrystalline Ni.* Materials Science and Engineering a-Structural Materials Properties Microstructure and Processing, 2013. 576: p. 69-73.

182. Wang, B., M.T. Alam, and M.A. Haque, *Grain growth in nanocrystalline nickel films at low temperature and stress.* Scripta Materialia, 2014. 71: p. 1-4.

183. Rinaldi, A., et al., *Sample-size effects in the yield behavior of nanocrystalline nickel.* Acta Materialia, 2008. 56(3): p. 511-517.

184. Thompson, C.V. and R. Carel, *Stress and grain growth in thin films.* Journal of the Mechanics and Physics of Solids, 1996. 44(5): p. 657-673.

185. Kumar, S., et al., *Electromigration stress induced deformation mechanisms in free-standing platinum thin films.* Scripta Materialia, 2011. 65(4): p. 277-280.

186. Chan, T., et al., *In Situ Heat Generation and Strain Localization of Polycrystalline and Nanocrystalline Nickel*, in *Thermomechanics and Infra-Red Imaging, Volume 7*. 2011, Springer New York. p. 17-23.

187. Fang, T.H., et al., *Revealing Extraordinary Intrinsic Tensile Plasticity in Gradient Nano-Grained Copper.* Science, 2011. 331(6024): p. 1587-1590.

188. Molodov, D.A. and Y. Mishin, *Plastic Deformation by Grain Boundary Motion: Experiments and Simulations*, in *Microstructural Design of Advanced Engineering Materials*. 2013, Wiley-VCH Verlag GmbH & Co. KGaA. p. 201-233.

189. Wu, Z.X., et al., *Anatomy of nanomaterial deformation: Grain boundary sliding, plasticity and cavitation in nanocrystalline Ni.* Acta Materialia, 2013. 61(15): p. 5807-5820.

190. Trogadas, P., T.F. Fuller, and P. Strasser, *Carbon as catalyst and support for electrochemical energy conversion.* Carbon, 2014. 75: p. 5-42.

191. Mao, X., T.A. Hatton, and G.C. Rutledge, *A Review of electrospun carbon fibers as electrode materials for energy storage.* Current Organic Chemistry, 2013. 17(13): p. 1390-1401.

192. Fei, L., et al., *Graphene Folding in Si Rich Carbon Nanofibers for Highly Stable, High Capacity Li-Ion Battery Anodes.* ACS Applied Materials & Interfaces, 2016. 8(8): p. 5243-5250.

193. Liu, X.-M., et al., *Carbon nanotube (CNT)-based composites as electrode material for rechargeable Li-ion batteries: A review.* Composites Science and Technology, 2012. 72(2): p. 121-144.

194. Shilpa, et al., *Enhanced electrical conductivity of suspended carbon nanofibers: Effect of hollow structure and improved graphitization.* Carbon, 2016. 108: p. 135-145.

195. Hu, L., et al., *Thin, Flexible Secondary Li-Ion Paper Batteries.* ACS Nano, 2010. 4(10): p. 5843-5848.

196. Arshad, S.N., M. Naraghi, and I. Chasiotis, *Strong carbon nanofibers from electrospun polyacrylonitrile.* Carbon, 2011. 49(5): p. 1710-1719.

197. Beese, A.M., et al., *In situ transmission electron microscope tensile testing reveals structure–property relationships in carbon nanofibers.* Carbon, 2013. 60: p. 246-253.

198. Poveda, R.L. and N. Gupta, *Carbon Nanofibers: Structure and Fabrication*, in *Carbon Nanofiber Reinforced Polymer Composites*, L.R. Poveda and N. Gupta, Editors. 2016, Springer International Publishing: Cham. p. 11-26.

199. Lee, S., et al., *Surface and structure modification of carbon nanofibers.* Synthetic Metals, 2007. 157(16–17): p. 644-650.

200. Zhang, B., et al., *Recent advances in electrospun carbon nanofibers and their application in electrochemical energy storage.* Progress in Materials Science, 2016. 76: p. 319-380.

201. Tibbetts, G.G., et al., *A review of the fabrication and properties of vapor-grown carbon nanofiber/polymer composites.* Composites Science and Technology, 2007. 67(7–8): p. 1709-1718.

202. Lee, B.O., W.J. Woo, and M.S. Kim, *EMI shielding effectiveness of carbon nanofiber filled poly (vinyl alcohol) coating materials.* Macromolecular Materials and Engineering, 2001. 286(2): p. 114-118.

203. Endo, M., et al., *Microstructural changes induced in "stacked cup" carbon nanofibers by heat treatment.* Carbon, 2003. 41(10): p. 1941-1947.

204. Burket, C.L., R. Rajagopalan, and H.C. Foley, *Overcoming the barrier to graphitization in a polymer-derived nanoporous carbon.* Carbon, 2008. 46(3): p. 501-510.

205. Fujita, J., et al., *Graphitic tube transformation of FIB-CVD pillar by Joule heating with flash discharge.* Microelectronic Engineering, 2007. 84(5-8): p. 1507-1510.

206. Huang, J.Y., et al., *Real-time observation of tubule formation from amorphous carbon nanowires under high-bias Joule heating.* Nano Letters, 2006. 6(8): p. 1699-1705.

207. Zwanger, M.S., F. Banhart, and A. Seeger, *Formation and decay of spherical concentric-shell carbon clusters.* Journal of Crystal Growth, 1996. 163(4): p. 445-454.

208. Lin, M. and C. Basaran, *Electromigration induced stress analysis using fully coupled mechanical–diffusion equations with nonlinear material properties.* Computational Materials Science, 2005. 34(1): p. 82-98.

209. De Orio, R., H. Ceric, and S. Selberherr, *Physically based models of electromigration: From Black's equation to modern TCAD models.* Microelectronics Reliability, 2010. 50(6): p. 775-789.

210. Tan, C., et al., *Development of Physics-Based Modeling for ULSI Interconnections Failure Mechanisms: Electromigration and Stress-Induced Voiding*, in *Applications of Finite Element Methods for Reliability Studies on ULSI Interconnections*. 2011, Springer London. p. 5-38.

211. Hoffman, R. and D. Turnbull, *Lattice and Grain Boundary Self-Diffusion in Silver.* Journal of Applied Physics, 1951. 22(5): p. 634-639.

212. Zhang, J. and J. Zhang, *Thermal-Mechanical Stress Enhanced Atomic Migration at the Solder/Under Bump Metallization Interface with Current Loading.* Advanced Science Letters, 2012. 5(2): p. 667-671.

213. Kirchheim, R., *Stress and electromigration in Al-lines of integrated circuits.* Acta Metallurgica et Materialia, 1992. 40(2): p. 309-323.

214. Asoka-Kumar, P., et al., *Detection of current-induced vacancies in thin aluminum–copper lines using positrons.* Applied Physics Letters, 1996. 68(3): p. 406-408.

215. Hayashi, T., et al., *Smallest Freestanding Single-Walled Carbon Nanotube.* Nano Letters, 2003. 3(7): p. 887-889.

216. Liu, W., et al., *Lignin-assisted direct exfoliation of graphite to graphene in aqueous media and its application in polymer composites.* Carbon, 2015. 83: p. 188-197.

217. Carrasco, P.M., et al., *High-concentration aqueous dispersions of graphene produced by exfoliation of graphite using cellulose nanocrystals.* Carbon, 2014. 70: p. 157-163.

218. Li, K., et al., *Extraction of contact resistance in carbon nanofiber via interconnects with varying lengths.* Applied Physics Letters, 2010. 97(25): p. 253109.

219. Saito, T., et al., *Improved contact for thermal and electrical transport in carbon nanofiber interconnects.* Applied Physics Letters, 2008. 93(10): p. 102108.

220. Zhang, B., et al., *Exceptional rate performance of functionalized carbon nanofiber anodes containing nanopores created by (Fe) sacrificial catalyst.* Nano Energy, 2014. 4: p. 88-96.

221. Xu, Z.-L., et al., *Carbon nanofibers containing Si nanoparticles and graphene-covered Ni for high performance anodes in Li ion batteries.* RSC Advances, 2014. 4(43): p. 22359-22366.

222. *Honeycomb GaN micro-light-emitting diodes.* Journal of Vacuum Science & Technology B: Microelectronics and Nanometer Structures Processing, Measurement, and Phenomena, 2006. 24(2): p. 800-802.

223. *AlGaN/GaN quantum well ultraviolet light emitting diodes.* Applied Physics Letters, 1998. 73(12): p. 1688-1690.

224. *GaN/AlGaN ultraviolet/infrared dual*-*band detector.* Applied Physics Letters, 2006. 89(9): p. 091113.

225. Okumura, H., *A roadmap for future wide bandgap semiconductor power electronics.* MRS Bulletin, 2015. 40(05): p. 439-444.

226. Tetsu, K., *Recent progress of GaN power devices for automotive applications.* Japanese Journal of Applied Physics, 2014. 53(10): p. 100210.

227. Iacopi, F., et al., *Power electronics with wide bandgap materials: Toward greener, more efficient technologies.* MRS Bulletin, 2015. 40(05): p. 390-395.

228. Zanoni, E., et al. *Reliability and failure physics of GaN HEMT, MIS-HEMT and p-gate HEMTs for power switching applications: Parasitic effects and degradation due to deep level effects and time-dependent breakdown phenomena*. in *2015 IEEE 3rd Workshop on Wide Bandgap Power Devices and Applications (WiPDA)*. 2015.

229. del Alamo, J.A. and J. Joh, *GaN HEMT reliability*. Microelectronics Reliability, 2009. 49(9–11): p. 1200-1206.

230. Park, S.Y., et al., *Physical degradation of GaN HEMT devices under high drain bias reliability testing.* Microelectronics Reliability, 2009. 49(5): p. 478-483.

231. Dun, S.B., et al., *Micro-Raman spectroscopy observation of field-induced strain relaxation in AlGaN/GaN heterojunction field-effect transistors.* Physica Status Solidi a-Applications and Materials Science, 2012. 209(6): p. 1174-1178.

232. Hilton, A.M., E.R. Heller, and D.L. Dorsey, *Electroluminescence Microscopy of Cross-Sectioned AlGaN/GaN High-Electron Mobility Transistors.* IEEE Transactions on Electron Devices, 2016. 63(4): p. 1459-1463.

233. Hilton, A., et al., *Characterization of cross-sectioned gallium nitride high-electron-mobility transistors with in situ biasing.* Journal of Electronic Materials, 2015. 44(10): p. 3259.

234. Zhou, L., Z. San, and J.F. Mao. *Electro-thermal-stress analysis of AlGaN/GaN HEMTs breakdown under intentional EMI*. in *2016 IEEE International Symposium on Radio-Frequency Integration Technology (RFIT)*. 2016.

235. Choi, S., et al., *The impact of mechanical stress on the degradation of AlGaN/GaN high electron mobility transistors.* Journal of Applied Physics, 2013. 114(16): p. 164501.

236. Lin, C.H., et al., *Strain and Temperature Dependence of Defect Formation at AlGaN/GaN High-Electron-Mobility Transistors on a Nanometer Scale.* IEEE Transactions on Electron Devices, 2012. 59(10): p. 2667-2674.

237. Chaplya, P.M. and G.P. Carman, *Dielectric and piezoelectric response of lead zirconate–lead titanate at high electric and mechanical loads in terms of non-180° domain wall motion.* Journal of Applied Physics, 2001. 90(10): p. 5278-5286.

238. Fang, D. and C. Li, *Nonlinear electric-mechanical behavior of a soft PZT-51 ferroelectric ceramic.* Journal of Materials Science, 1999. 34(16): p. 4001-4010.

239. Fett, T., D. Munz, and G. Thun, *Stress-Strain Behaviour of a Soft PZT Ceramic Under Tensile and Compression Loading and a Transverse Electric Field.* Ferroelectrics, 2003. 297(1): p. 83-90.

240. Hwang, S.C., C.S. Lynch, and R.M. McMeeking, *Ferroelectric/ferroelastic interactions and a polarization switching model.* Acta Metallurgica et Materialia, 1995. 43(5): p. 2073-2084.

241. Yongzhong, H. and J. Qing, *Modeling of domain switching in polycrystalline ferroelectric ceramics.* Smart Materials and Structures, 1997. 6(4): p. 441.

242. Chen, X., D.N. Fang, and K.C. Hwang, *Micromechanics simulation of ferroelectric polarization switching.* Acta Materialia, 1997. 45(8): p. 3181-3189.

243. Wang, J., et al., *Phase-field simulations of ferroelectric/ferroelastic polarization switching.* Acta Materialia, 2004. 52(3): p. 749-764.

244. Fotinich, Y. and G.P. Carman, *Stresses in piezoceramics undergoing polarization switchings.* Journal of Applied Physics, 2000. 88(11): p. 6715-6725.

245. Sun, C.-T. and A. Achuthan, *Domain-Switching Criteria for Ferroelectric Materials Subjected to Electrical and Mechanical Loads.* Journal of the American Ceramic Society, 2004. 87(3): p. 395-400.

246. Paduano, Q., et al., *Growth and characteristics of AlGaN/GaN heterostructures on sp 2-bonded BN by metal–organic chemical vapor deposition.* Journal of Materials Research, 2016. 31(15): p. 2204-2213.

247. Hellman, E.S., *The Polarity of GaN: a Critical Review.* MRS Internet Journal of Nitride Semiconductor Research, 1998. 3.

248. Sumiya, M. and S. Fuke, *Review of polarity determination and control of GaN.* MRS Internet Journal of Nitride Semiconductor Research, 2004. 9.

249. Hushur, A., M.H. Manghnani, and J. Narayan, *Raman studies of GaN/sapphire thin film heterostructures.* Journal of Applied Physics, 2009. 106(5): p. 054317.

250. Gruverman, A., et al., *Direct studies of domain switching dynamics in thin film ferroelectric capacitors.* Applied Physics Letters, 2005. 87(8): p. 082902.

251. Shen, K.-C., et al., *Pulsed laser deposition of hexagonal GaN-on-Si(100) template for MOCVD applications.* Optics Express, 2013. 21(22): p. 26468-26474.

252. Makaram, P., et al., *Evolution of structural defects associated with electrical degradation in AlGaN/GaN high electron mobility transistors.* Applied Physics Letters, 2010. 96(23): p. 233509.

253. Chowdhury, U., et al., *TEM observation of crack- and pit-shaped defects in electrically degraded GaNHEMTs.* IEEE Electron Device Letters, 2008. 29(10): p. 1098-1100.

254. Wenjun, Z., et al., *An analysis of the effect of domain switching on fracture behavior of piezoelectric solids.* Smart Materials and Structures, 2003. 12(1): p. 88.

255. Minary-Jolandan, M., et al., *Individual GaN Nanowires Exhibit Strong Piezoelectricity in 3D.* Nano Letters, 2012. 12(2): p. 970-976.

256. Vurgaftman, I. and J.R. Meyer, *Electron Bandstructure Parameters*, in *Nitride Semiconductor Devices: Principles and Simulation*. 2007, Wiley-VCH Verlag GmbH & Co. KGaA. p. 13-48.

257. Huang, J.Y., et al., *In Situ Nanomechanics of GaN Nanowires.* Nano Letters, 2011. 11(4): p. 1618-1622.

258. Lee, C., et al., *Measurement of the Elastic Properties and Intrinsic Strength of Monolayer Graphene.* Science, 2008. 321(5887): p. 385-388.

259. Mayorov, A.S., et al., *Micrometer-Scale Ballistic Transport in Encapsulated Graphene at Room Temperature.* Nano Letters, 2011. 11(6): p. 2396-2399.

260. Balandin, A.A., *Thermal properties of graphene and nanostructured carbon materials.* Nat Mater, 2011. 10(8): p. 569-581.

261. Ferrari, A.C., et al., *Science and technology roadmap for graphene, related two-dimensional crystals, and hybrid systems.* Nanoscale, 2015. 7(11): p. 4598-4810.

262. Novoselov, K.S., et al., *A roadmap for graphene.* Nature, 2012. 490(7419): p. 192-200.

263. Lee, S.-M., J.-H. Kim, and J.-H. Ahn, *Graphene as a flexible electronic material: mechanical limitations by defect formation and efforts to overcome.* Materials Today, 2015. 18(6): p. 336-344.

264. Algara-Siller, G., et al., *Dry-cleaning of graphene.* Applied Physics Letters, 2014. 104(15): p. 153115.

265. Lee, J., et al., *Clean transfer of graphene and its effect on contact resistance.* Applied Physics Letters, 2013. 103(10): p. 103104.

266. Yu Wang, Y. and P.J. Burke, *A large-area and contamination-free graphene transistor for liquid-gated sensing applications.* Applied Physics Letters, 2013. 103(5): p. 052103.

267. Moser, J., A. Barreiro, and A. Bachtold, *Current-induced cleaning of graphene.* Applied Physics Letters, 2007. 91(16): p. 163513.

268. Hertel, S., et al., *Current annealing and electrical breakdown of epitaxial graphene.* Applied Physics Letters, 2011. 98(21): p. 212109.

269. Shanmugam, M., et al., *2D layered insulator hexagonal boron nitride enabled surface passivation in dye sensitized solar cells.* Nanoscale, 2013. 5(22): p. 11275-11282.

270. Wang, B., M.T. Alam, and M.A. Haque, *Grain growth in nanocrystalline nickel films at low temperature and stress.* Scripta Materialia, 2014. 71(0): p. 1-4.

271. Graf, D., et al., *Spatially resolved Raman spectroscopy of single-and few-layer graphene.* Nano letters, 2007. 7(2): p. 238-242.

272. Murali, R., et al., *Breakdown current density of graphene nanoribbons.* Applied Physics Letters, 2009. 94(24): p. 243114.

273. Shao, Q., et al., *High-temperature quenching of electrical resistance in graphene interconnects.* Applied Physics Letters, 2008. 92(20): p. 202108.

274. Barreiro, A., et al., *Structured Graphene Devices for Mass Transport.* Small, 2011. 7(6): p. 775-780.

275. Lloyd, J.R., *Electromigration in thin film conductors.* Semiconductor Science and Technology, 1997. 12(10): p. 1177.

276. Chan, K.T., J.B. Neaton, and M.L. Cohen, *First-principles study of metal adatom adsorption on graphene.* Physical Review B, 2008. 77(23): p. 235430.

277. Ribeiro, F.J., et al., *Mechanism for bias-assisted indium mass transport on carbon nanotube surfaces.* Physical Review B, 2005. 72(7): p. 075302.

278. Lupina, G., et al., *Residual Metallic Contamination of Transferred Chemical Vapor Deposited Graphene.* ACS Nano, 2015. 9(5): p. 4776-4785.

279. Velizhanin, K.A., N. Dandu, and D. Solenov, *Electromigration of bivalent functional groups on graphene.* Physical Review B, 2014. 89(15): p. 155414.

280. Susi, T., et al., *Silicon\char21{}Carbon Bond Inversions Driven by 60-keV Electrons in Graphene.* Physical Review Letters, 2014. 113(11): p. 115501.

281. Chung, C.-K. and B. Wu, *Effect of substrate temperature on the in-situ formation of crystalline SiC nanostructured film using ultra-high-vacuum ion beam sputtering.* Journal of nanoscience and nanotechnology, 2010. 10(7): p. 4679-4683.

282. Butler, S.Z., et al., *Progress, Challenges, and Opportunities in Two-Dimensional Materials Beyond Graphene.* ACS Nano, 2013. 7(4): p. 2898-2926.

283. Shi, Y., H. Li, and L.-J. Li, *Recent advances in controlled synthesis of two-dimensional transition metal dichalcogenides via vapour deposition techniques.* Chemical Society Reviews, 2015. 44(9): p. 2744-2756.

284. Wang, H., et al., *Two-dimensional heterostructures: fabrication, characterization, and application.* Nanoscale, 2014. 6(21): p. 12250-12272.

285. Mak, K.F., et al., *The valley Hall effect in MoS2 transistors.* Science, 2014. 344(6191): p. 1489-1492.

286. Das, S., et al., *All Two-Dimensional, Flexible, Transparent, and Thinnest Thin Film Transistor.* Nano Letters, 2014. 14(5): p. 2861-2866.

287. Huang, J., et al., *Large-area synthesis of monolayer WSe2 on a SiO2/Si substrate and its device applications.* Nanoscale, 2015. 7(9): p. 4193-4198.

288. Das, S. and J. Appenzeller, *WSe2 field effect transistors with enhanced ambipolar characteristics.* Applied Physics Letters, 2013. 103(10): p. 103501.

289. Huang, J.-K., et al., *Large-Area Synthesis of Highly Crystalline WSe2 Monolayers and Device Applications.* ACS Nano, 2014. 8(1): p. 923-930.

290. Pradhan, N.R., et al., *Hall and field-effect mobilities in few layered p-WSe2 field-effect transistors.* Sci. Rep., 2015. 5.

291. Fang, H., et al., *High-Performance Single Layered WSe2 p-FETs with Chemically Doped Contacts.* Nano Letters, 2012. 12(7): p. 3788-3792.

292. Jia, K., et al., *Effects of defects and thermal treatment on the properties of graphene.* Vacuum, 2015. 116(0): p. 90-95.

293. Nan, H.Y., et al., *The thermal stability of graphene in air investigated by Raman spectroscopy.* Journal of Raman Spectroscopy, 2013. 44(7): p. 1018-1021.

294. Lu, X., et al., *Layer-by-layer thinning of MoS2 by thermal annealing.* Nanoscale, 2013. 5(19): p. 8904-8908.

295. Singh Raman, R.K., et al., *Protecting copper from electrochemical degradation by graphene coating.* Carbon, 2012. 50(11): p. 4040-4045.

296. Wood, J.D., et al., *Effective Passivation of Exfoliated Black Phosphorus Transistors against Ambient Degradation.* Nano Letters, 2014. 14(12): p. 6964-6970.

297. Eichfeld, S.M., et al., *Highly Scalable, Atomically Thin WSe2 Grown via Metal–Organic Chemical Vapor Deposition.* ACS Nano, 2015. 9(2): p. 2080-2087.

298. Azizi, A., et al., *Freestanding van der Waals Heterostructures of Graphene and Transition Metal Dichalcogenides.* ACS Nano, 2015.

299. Allain, A. and A. Kis, *Electron and Hole Mobilities in Single-Layer WSe2.* ACS Nano, 2014. 8(7): p. 7180-7185.

300. Wang, J.I.J., et al., *Electronic Transport of Encapsulated Graphene and WSe2 Devices Fabricated by Pick-up of Prepatterned hBN.* Nano Letters, 2015. 15(3): p. 1898-1903.

301. Clark, G., et al., *Vapor-transport growth of high optical quality WSe2 monolayers a.* APL Materials, 2014. 2(10): p. 101101.

302. Paul, B., et al., *Large-area synthesis of WSe 2 from WO 3 by selenium–oxygen ion exchange.* 2D Materials, 2015. 2(1): p. 014003.

303. Li, X., et al., *Large-Area Synthesis of High-Quality and Uniform Graphene Films on Copper Foils.* Science, 2009. 324(5932): p. 1312-1314.

304. Tao, C., W.G. Cullen, and E.D. Williams, *Visualizing the Electron Scattering Force in Nanostructures.* Science, 2010. 328(5979): p. 736.

305. Solenov, D. and K.A. Velizhanin, *Adsorbate Transport on Graphene by Electromigration.* Physical Review Letters, 2012. 109(9): p. 095504.

306. Parker, J.H., D.W. Feldman, and M. Ashkin, *Raman Scattering by Silicon and Germanium.* Physical Review, 1967. 155(3): p. 712-714.

307. Huran, J., et al., *The effect of neutron irradiation on the properties of SiC and SiC(N) layer prepared by plasma enhanced chemical vapor deposition.* Applied Surface Science, 2013. 269(0): p. 88-91.

308. Lin, Y.-C., et al., *Atomically Thin Heterostructures Based on Single-Layer Tungsten Diselenide and Graphene.* Nano Letters, 2014. 14(12): p. 6936-6941.

309. Buscema, M., et al., *Large and Tunable Photothermoelectric Effect in Single-Layer MoS2.* Nano letters, 2013. 13(2): p. 358-363.

310. Das, S. and J. Appenzeller, *Screening and interlayer coupling in multilayer MoS2.* physica status solidi (RRL) – Rapid Research Letters, 2013. 7(4): p. 268-273.

311. Splendiani, A., et al., *Emerging Photoluminescence in Monolayer MoS2.* Nano Letters, 2010. 10(4): p. 1271-1275.

312. Bernardi, M., M. Palummo, and J.C. Grossman, *Extraordinary Sunlight Absorption and One Nanometer Thick Photovoltaics Using Two-Dimensional Monolayer Materials.* Nano Letters, 2013. 13(8): p. 3664-3670.

313. Fontana, M., et al., *Electron-hole transport and photovoltaic effect in gated MoS2 Schottky junctions.* Scientific Reports, 2013. 3.

314. Lopez-Sanchez, O., et al., *Ultrasensitive photodetectors based on monolayer MoS2.* Nature Nanotechnology, 2013. 8(7): p. 497-501.

315. Plechinger, G., et al., *Low-temperature photoluminescence of oxide-covered single-layer MoS2.* physica status solidi (RRL) – Rapid Research Letters, 2012. 6(3): p. 126-128.

316. Muratore, C., et al., *Thermal anisotropy in nano-crystalline* MoS_2 *thin films.* Physical Chemistry Chemical Physics, 2013.

317. Muratore, C. and A.A. Voevodin, *Control of molybdenum disulfide basal plane orientation during coating growth in pulsed magnetron sputtering discharges.* Thin Solid Films, 2009. 517: p. 5605-5610.

318. Lince, J.R., D.J. Carre, and P.D. Fleischauer, *Effects of argon-ion bombardment on the basal plane surface of molybdenum disulfide.* Langmuir, 1986. 2(6): p. 805-808.

319. Bierwagen, O., et al., *Mobility and carrier density in materials with anisotropic conductivity revealed by van der Pauw measurements.* Physical Review B, 2004. 70(16): p. 165307.

320. Fontana, M., et al., *Photovoltaic effect in gated MoS2 Schottky junctions.* 2012.

321. Shanmugam, M., et al., *Schottky-barrier solar cell based on layered semiconductor tungsten disulfide nanofilm.* Applied Physics Letters, 2012. 101(26).

322. Yin, Z., et al., *Single-layer MoS2 phototransistors.* ACS nano, 2011. 6(1): p. 74-80.

323. Popov, I., G. Seifert, and D. Tománek, *Designing Electrical Contacts to MoS_ {2} Monolayers: A Computational Study*. Physical Review Letters, 2012. 108(15): p. 156802.

324. Grodnenskii, I., K. Starostin, and D. Galchenkov, *Negative photoconductivity of 2 D electrons in semiconductor heterostructures.* JETP Letters, 1986. 43: p. 70-73.

325. Nakanishi, H., et al., *Photoconductance and inverse photoconductance in films of functionalized metal nanoparticles.* Nature, 2009. 460(7253): p. 371-375.

326. Serpi, A., *Negative Photoconductivity in MoS2.* physica status solidi (a), 1992. 133(2): p. K73-K77.

327. Wei, P.-C., et al., *Room-temperature negative photoconductivity in degenerate InN thin films with a supergap excitation.* Physical Review B, 2010. 81(4): p. 045306.

328. Jing-Gao, Z., S. Jia-Lin, and X. Ping, *Negative Photoconductivity Induced by Surface Plasmon Polaritons in the Kretschmann Configuration.* Chinese Physics Letters, 2011. 28(12): p. 127302.

329. Pankove, J., *The anomalous photovoltaic effect.* physica status solidi (a), 1980. 61(1): p. 127-132.

330. Das, S., et al., *High Performance Multilayer MoS2 Transistors with Scandium Contacts.* Nano Letters, 2012. 13(1): p. 100-105.

331. Giovannetti, G., et al., *Doping Graphene with Metal Contacts.* Physical Review Letters, 2008. 101(2): p. 026803.

332. Jiang, J.-W., X. Zhuang, and T. Rabczuk, *Orientation Dependent Thermal Conductance in Single-Layer MoS2.* Sci. Rep., 2013. 3.

333. Zinkle, S.J. and G.S. Was, *Materials challenges in nuclear energy.* Acta Materialia, 2013. 61(3): p. 735-758.

334. Yan, C., et al., *Effects of ion irradiation on microstructure and properties of zirconium alloys—A review.* Nuclear Engineering and Technology, 2015. 47(3): p. 323-331.

335. Was, G.S., *Fundamentals of Radiation Materials Science: Metals and Alloys*. 2007: Springer Berlin Heidelberg.

336. Dayal, P., et al., *Effect of double ion implantation and irradiation by Ar and He ions on nano-indentation hardness of metallic alloys.* Journal of Nuclear Materials, 2013. 438(1–3): p. 108-115.

337. Sarkar, A., et al., *Investigation of microstructure and mechanical properties of proton irradiated Zircaloy 2.* Journal of Nuclear Materials, 2016. 479: p. 524-532.

338. Liu, W., et al., *Irradiation Induced Microstructure Evolution in Nanostructured Materials: A Review.* Materials, 2016. 9(2): p. 105.

339. Beyerlein, I.J., et al., *Radiation damage tolerant nanomaterials.* Materials Today, 2013. 16(11): p. 443-449.

340. Cheng, G.M., et al., *Grain size effect on radiation tolerance of nanocrystalline Mo.* Scripta Materialia, 2016. 123: p. 90-94.

341. Argon, A.S. and S. Yip, *The strongest size.* Philosophical Magazine Letters, 2006. 86(11): p. 713-720.

342. Idrees, Y., et al., *In situ study of defect accumulation in zirconium under heavy ion irradiation.* Journal of Nuclear Materials, 2013. 433(1–3): p. 95-107.

343. Hengstler-Eger, R.M., et al., *Heavy ion irradiation induced dislocation loops in AREVA's M5® alloy.* Journal of Nuclear Materials, 2012. 423(1–3): p. 170-182.

344. Yamada, S. and T. Kameyama, *Observation of c-component dislocation structures formed in pure Zr and Zr-base alloy by self-ion accelerator irradiation.* Journal of Nuclear Materials, 2012. 422(1–3): p. 167-172.

345. Ziegler, J.F., M.D. Ziegler, and J.P. Biersack, *SRIM – The stopping and range of ions in matter (2010).* Nuclear Instruments and Methods in Physics Research Section B: Beam Interactions with Materials and Atoms, 2010. 268(11–12): p. 1818-1823.

346. Bufford, D.C., et al., *Unraveling irradiation induced grain growth with in situ transmission electron microscopy and coordinated modeling.* Applied Physics Letters, 2015. 107(19): p. 191901.

347. Motta, A., D. Kaoumi, and R. Birtcher, *Grain Growth in Nanocrystalline Metal Thin Films under In Situ Ion-Beam Irradiation.* Journal of ASTM International, 2007. 4(8): p. 1-13.

348. Zhang, Y., et al., *Structural modification of nanocrystalline ceria by ion beams.* Physical Chemistry Chemical Physics, 2011. 13(25): p. 11946-11950.

349. Muntifering, B., et al., *Electron Beam Effects during In-Situ Annealing of Self-Ion Irradiated Nanocrystalline Nickel.* MRS Proceedings, 2015. 1809: p. 13-18.

350. Hahn, E.N. and M.A. Meyers, *Grain-size dependent mechanical behavior of nanocrystalline metals.* Materials Science and Engineering: A, 2015. 646: p. 101-134.

Baoming Wang

317 Leonhard Building, Pennsylvania State University, University Park, PA 16802

E-mail: bzw127@psu.edu, wbmllmy@gmail.com

Education

2012 - Present	**Doctor of Philosophy** (June, 2017), CGPA: 3.89 / 4.00, Mechanical Engineering (ME), Pennsylvania State University, University Park, PA.
2006 - 2010	**Bachelor of Science in Mechanical Engineering,** CGPA: 90/100, Mechanical Engineering (ME), Xiamen University, Xiamen, China.

Key Publications

---

1. **Baoming Wang**, D.E. Wolfe, M. Terrones, M.A. Haque, S. Ganguly, A.K. Roy, "Electro-graphitization and exfoliation of graphene on carbon nanofibers", Carbon, Volume 117, June 2017, Pages 201-207
2. **Baoming Wang**, SM Eichfield, Dixiong Wang, JA Robinson, MA Haque, "In situ degradation studies of two-dimensional WSe_2–graphene heterostructures", Nanoscale, 2015,7, 14489-14495
3. **Baoming Wang**, Aman Haque, Alexander E. Mag-isa, Hak-Joo Lee "High temperature and current density induced degradation of multi-layer graphene", Applied Physics Letters 107, 163103 (2015)
4. **Baoming Wang**, Tarek Alam and Aman Haque., "Grain Growth in Nano-crystalline Nickel Films at Low Temperature and Stress", Scripta Materialia, Volume 71, pp. 1-4, 2014.
5. **Baoming Wang**, Aman Haque, "In Situ Microstructural Control and Mechanical Testing Inside the Transmission Electron Microscope at Elevated Temperatures", JOM, Volume 67, Issue 8 , pp 1713-1720 (2015)
6. **Baoming Wang**, Vikas Tomar, Aman Haque, "In-situ TEM mechanical testing of nanocrystalline zirconium thin films", Materials Letters, Volume 152, 1 August 2015, Pages 105-108
7. **Baoming Wang** and Aman Haque, "Low Temperature Viscoelasticity in Nanocrystalline Nickel Films", Materials Letters, Vol. 188, pp. 59-61, 2014
8. **Baoming Wang**, Raghu Pulavarthy, Aman Haque, "Grain size induced thermo-mechanical coupling in Zirconium thin films", Journal of Thermal Analysis and Calorimetry, Volume 123, Issue 2, pp 1197–1204, 2016
9. **Baoming Wang**, Christopher Muratore, Andrey A Voevodin, Md Amanul Haque, "Photo-sensitivity of large area physical vapor deposited mono and bilayer MoS_2", Nano Convergence, 2014. 1(1): p. 1-5
10. **Baoming Wang**, M. Zahabul Islam, Kehao Zhang, Ke Wang, Joshua Robinson, Aman Haque, "Fracture mechanism of monolayer MoS_2" Nanotechnology (Accepted)
11. **Baoming Wang**, Vikas Tomar, Aman Haque, "Self-ion irradiation effects on mechanical properties of nanocrystalline zirconium films" MRS Communications (Accepted)
12. **Baoming Wang**, Tun Wang, Aman Haque, Michael Snure, Eric Heller, and Nicholas Glavin, "In-situ TEM Study of Domain Switching in GaN Thin Films", Applied Physics Letters (Submitted)